



JPTM

Journal of Pathology
and Translational Medicine

March 2021
Vol. 55 / No.2
jpatholm.org
pISSN: 2383-7837
eISSN: 2383-7845



*Dysplastic Subtypes
in Inflammatory
Bowel Disease*

Aims & Scope

The *Journal of Pathology and Translational Medicine* is an open venue for the rapid publication of major achievements in various fields of pathology, cytopathology, and biomedical and translational research. The Journal aims to share new insights into the molecular and cellular mechanisms of human diseases and to report major advances in both experimental and clinical medicine, with a particular emphasis on translational research. The investigations of human cells and tissues using high-dimensional biology techniques such as genomics and proteomics will be given a high priority. Articles on stem cell biology are also welcome. The categories of manuscript include original articles, review and perspective articles, case studies, brief case reports, and letters to the editor.

Subscription Information

To subscribe to this journal, please contact the Korean Society of Pathologists/the Korean Society for Cytopathology. Full text PDF files are also available at the official website (<https://jpatholm.org>). *Journal of Pathology and Translational Medicine* is indexed by Emerging Sources Citation Index (ESCI), PubMed, PubMed Central, Scopus, KoreaMed, KoMCI, WPRIM, Directory of Open Access Journals (DOAJ), and CrossRef. Circulation number per issue is 50.

Editors-in-Chief

Jung, Chan Kwon, MD (*The Catholic University of Korea, Korea*) <https://orcid.org/0000-0001-6843-3708>

Park, So Yeon, MD (*Seoul National University, Korea*) <https://orcid.org/0000-0002-0299-7268>

Associate Editors

Shin, Eunah, MD (*Yongin Severance Hospital, Yonsei University, Korea*) <https://orcid.org/0000-0001-5961-3563>

Kim, Haeryoung, MD (*Seoul National University, Korea*) <https://orcid.org/0000-0002-4205-9081>

Bychkov, Andrey, MD (*Kameda Medical Center, Japan; Nagasaki University Hospital, Japan*) <https://orcid.org/0000-0002-4203-5696>

Editorial Board

Avila-Casado, Maria del Carmen, MD (*University of Toronto, Toronto General Hospital UHN, Canada*)

Bae, Young Kyung, MD (*Yeungnam University, Korea*)

Bongiovanni, Massimo, MD (*Lausanne University Hospital, Switzerland*)

Bova, G. Steven, MD (*University of Tampere, Finland*)

Choi, Joon Hyuk, MD (*Yeungnam University, Korea*)

Chong, Yo Sep, MD (*The Catholic University of Korea, Korea*)

Chung, Jin-Haeng, MD (*Seoul National University, Korea*)

Fadda, Guido, MD (*Catholic University of Rome-Foundation Agostino Gemelli University Hospital, Italy*)

Fukushima, Noriyoshi, MD (*Jichi Medical University, Japan*)

Go, Heunjeong, MD (*University of Ulsan, Korea*)

Hong, Soon Won, MD (*Yonsei University, Korea*)

Jain, Deepali, MD (*All India Institute of Medical Sciences, India*)

Kakudo, Kennichi, MD (*Izumi City General Hospital, Japan*)

Kim, Jang-Hee, MD (*Ajou University, Korea*)

Kim, Jung Ho, MD (*Seoul National University, Korea*)

Kim, Se Hoon, MD (*Yonsei University, Korea*)

Komuta, Miina, MD (*Keio University, Tokyo, Japan*)

Kwon, Ji Eun, MD (*Ajou University, Korea*)

Lai, Chiung-Ru, MD (*Taipei Veterans General Hospital, Taiwan*)

Lee, C. Soon, MD (*University of Western Sydney, Australia*)

Lee, Hye Seung, MD (*Seoul National University, Korea*)

Lee, Sung Hak, MD (*The Catholic University, Korea*)

Liu, Zhiyan, MD (*Shanghai Jiao Tong University, China*)

Lkhagvadorj, Sayamaa, MD (*Mongolian National University of Medical Sciences, Mongolia*)

Moran, Cesar, MD (*MD Anderson Cancer Center, U.S.A.*)

Paik, Jin Ho, MD (*Seoul National University, Korea*)

Park, Jeong Hwan, MD (*Seoul National University, Korea*)

Ro, Jae Y., MD (*Cornell University, The Methodist Hospital, U.S.A.*)

Sakhujia, Puja, MD (*Govind Ballabh Pant Hospital, India*)

Shahid, Pervez, MD (*Aga Khan University, Pakistan*)

Song, Joon Seon, MD (*University of Ulsan, Korea*)

Tan, Puay Hoon, MD (*National University of Singapore, Singapore*)

Than, Nandor Gabor, MD (*Semmelweis University, Hungary*)

Tse, Gary M., MD (*The Chinese University of Hong Kong, Hong Kong*)

Yatabe, Yasushi, MD (*Aichi Cancer Center, Japan*)

Zhu, Yun, MD (*Jiangsu Institution of Nuclear Medicine, China*)

Ethic Editor

Choi, In-Hong, MD (*Yonsei University, Korea*)

Huh, Sun, MD (*Hallym University, Korea*)

Statistics Editors

Kim, Dong Wook (*National Health Insurance Service Ilsan Hospital, Korea*)

Lee, Hye Sun (*Yonsei University, Korea*)

Manuscript Editor

Chang, Soo-Hee (*InfoLumi Co., Korea*)

Layout Editor

Kim, Haeja (*iMiS Company Co., Ltd., Korea*)

Website and JATS XML File Producers

Cho, Yoonsang (*M2Community Co., Korea*)

Im, Jeonghee (*M2Community Co., Korea*)

Administrative Assistants

Jung, Ji Young (*The Korean Society of Pathologists*)

Jeon, Anmi (*The Korean Society for Cytopathology*)

Contact the Korean Society of Pathologists/the Korean Society for Cytopathology

Publishers: Cho, Nam Hoon, MD, Gong, Gyungyub, MD

Editors-in-Chief: Jung, Chan Kwon, MD, Park, So Yeon, MD

Published by the Korean Society of Pathologists/the Korean Society for Cytopathology

Editorial Office

Room 1209 Gwanghwamun Officia, 92 Saemunan-ro, Jongno-gu, Seoul 03186, Korea

Tel: +82-2-795-3094 Fax: +82-2-790-6635 E-mail: office@jpatholm.org

#1508 Renaissancetower, 14 Mallijae-ro, Mapo-gu, Seoul 04195, Korea

Tel: +82-2-593-6943 Fax: +82-2-593-6944 E-mail: office@jpatholm.org

Printed by iMiS Company Co., Ltd. (JMC)

Jungang Bldg. 18-8 Wonhyo-ro 89-gil, Yongsan-gu, Seoul 04314, Korea

Tel: +82-2-717-5511 Fax: +82-2-717-5515 E-mail: ml@smileml.com

Manuscript Editing by InfoLumi Co.

210-202, 421 Pangyo-ro, Bundang-gu, Seongnam 13522, Korea

Tel: +82-70-8839-8800 E-mail: infolumi.chang@gmail.com

Front cover image: Conventional dysplasia, hypermucinous dysplasia, and crypt cell dysplasia (p85, p88).

© Copyright 2021 by the Korean Society of Pathologists/the Korean Society for Cytopathology

© Journal of Pathology and Translational Medicine is an Open Access journal under the terms of the Creative Commons Attribution Non-Commercial License (<https://creativecommons.org/licenses/by-nc/4.0>).

© This paper meets the requirements of KS X ISO 9706, ISO 9706-1994 and ANSI/NISO Z.39.48-1992 (Permanence of Paper).

CONTENTS

REVIEW

- 83 Non-conventional dysplastic subtypes in inflammatory bowel disease: a review of their diagnostic characteristics and potential clinical implications
Won-Tak Choi

ORIGINAL ARTICLES

- 94 Histologically confirmed distant metastatic urothelial carcinoma from the urinary bladder: a retrospective review of one institution's 20-year experience
Youngeun Yoo, Junghye Lee, Heae Surng Park, Min-Sun Cho, Sun Hee Sung, Sanghui Park, Euno Choi
- 102 The prognostic significance of p16 expression pattern in diffuse gliomas
Jin Woo Park, Jeongwan Kang, Ka Young Lim, Hyunhee Kim, Seong-Ik Kim, Jae Kyung Won, Chul-Kee Park, Sung-Hye Park
- 112 A study of pathological characteristics and *BRAF* V600E status in Langerhans cell histiocytosis of Vietnamese children
Thu Dang Anh Phan, Bao Gia Phung, Tu Thanh Duong, Vu Anh Hoang, Dat Quoc Ngo, Nguyen Dinh The Trinh, Tung Thanh Tran
- 118 Deep learning for computer-assisted diagnosis of hereditary diffuse gastric cancer
Sean A. Rasmussen, Thomas Arnason, Weei-Yuarn Huang
- 125 MicroRNA-552 expression in colorectal cancer and its clinicopathological significance
Joon Im, Soo Kyung Nam, Hye Seung Lee

CASE REPORTS

- 132 Adenocarcinoma of the minor salivary gland with concurrent *MAML2* and *EWSR1* alterations
Sangjoon Choi, Junhun Cho, Seung Eun Lee, Chung-Hwan Baek, Yi-Kyung Kim, Hyung-Jin Kim, Young Hye Ko
- 139 A case of concomitant *EGFR/ALK* alteration against a mutated *EGFR* background in early-stage lung adenocarcinoma
Ki-Chang Lee, Jiwon Koh, Doo Hyun Chung, Yoon Kyung Jeon

145 Malignant rhabdoid tumor of the kidney in an adult with loss of INI1 expression and mutation in the *SMARCB1* gene
Eunkyung Han, Jiyeon Kim, Min Jung Jung, Susie Chin, Sang Wook Lee, Ahrim Moon

154 Multiple hepatocyte nuclear factor 1A (HNF1A)-inactivated hepatocellular adenomas arising in a background of congenital hepatic fibrosis
Yangkyu Lee, Hyunjin Park, Kyoungbun Lee, Youngeun Lee, Kiryang Lee, Haeryoung Kim

NEWSLETTER

159 What's New in Pathology Newsletter by PathologyOutlines.com
Nat Pernick

161 What's new in gynecologic pathology 2021: vulva, cervix, and uterus
Carlos Parra-Herran, Jennifer A. Bennett

Instructions for Authors for *Journal of Pathology and Translational Medicine* are available at <http://jpatholm.org/authors/authors.php>

Non-conventional dysplastic subtypes in inflammatory bowel disease: a review of their diagnostic characteristics and potential clinical implications

Won-Tak Choi

Department of Pathology, University of California at San Francisco, San Francisco, CA, USA

The early detection and grading of dysplasia is the current standard of care to minimize mortality from colorectal cancer (CRC) in patients with inflammatory bowel disease. With the development of advanced endoscopic resection techniques, colectomy is now reserved for patients with invisible/flat dysplasia (either high-grade [HGD] or multifocal low-grade dysplasia) or endoscopically unresectable lesions. Although most pathologists are familiar with the morphologic criteria of conventional (intestinal type) dysplasia, the most well-recognized form of dysplasia, an increasing number of diagnostic material has led to the recognition of several different morphologic patterns of epithelial dysplasia. The term “non-conventional” dysplasia has been coined to describe these changes, but to date, the recognition and full appreciation of these novel forms of dysplasia by practicing pathologists is uneven. The recognition of these non-conventional subtypes is becoming increasingly important, as some of them appear to have a higher risk of developing HGD or CRC than conventional dysplasia or sporadic adenomas. This review describes the morphologic characteristics of all seven non-conventional subtypes that have been reported to date as well as our current understanding of their clinicopathologic and molecular features that distinguish them from conventional dysplasia or sporadic adenomas.

Key Words: Colorectal neoplasm; Dysplasia; Inflammatory bowel disease; Non-conventional

Received: January 15, 2021 **Accepted:** February 17, 2021

Corresponding Author: Won-Tak Choi, MD, PhD, Department of Pathology, University of California at San Francisco, 505 Parnassus Avenue, M552, Box 0102, San Francisco, CA 94143, USA

Tel: +1-415-353-9533, Fax: +1-415-353-1200, E-mail: Won-Tak.Choi@ucsf.edu

Although pathologists have a good grasp of the morphologic criteria of conventional (intestinal type) dysplasia, several unfamiliar morphologic patterns of epithelial dysplasia have been recently described in inflammatory bowel disease (IBD). They are collectively referred to as “non-conventional” dysplasia, and there are at least seven subtypes that have been reported to date. This review summarizes their morphologic criteria as well as clinicopathologic and molecular features that distinguish them from conventional dysplasia or sporadic adenomas. The review is divided into three major parts: (1) clinical importance and management of invisible/flat dysplasia, (2) potential significance of non-conventional dysplasia, and (3) subtypes of non-conventional dysplasia—(a) hypermucinous dysplasia, (b) crypt cell dysplasia, (c) dysplasia with increased Paneth cell differentiation, (d) goblet cell deficient dysplasia, and (e) serrated dysplasia, including sessile serrated lesion (SSL)–like dysplasia, traditional

serrated adenoma (TSA)–like dysplasia, and serrated dysplasia, not otherwise specified (NOS).

CLINICAL IMPORTANCE AND MANAGEMENT OF INVISIBLE/FLAT DYSPLASIA

IBD is a well-established risk factor for the development of dysplasia and/or colorectal cancer (CRC) [1-5]. The risk of CRC is similar in both ulcerative colitis (UC) and Crohn’s disease [3], but younger age, male gender, longer disease duration, and primary sclerosing cholangitis (PSC) are often associated with a higher risk of developing dysplasia and/or CRC [4,6-8]. Surveillance colonoscopy is typically initiated at eight years after IBD diagnosis to detect pre-invasive, dysplastic lesions to reduce mortality from CRC [9-13].

Traditionally, the detection of IBD-related dysplasia has re-

lied on targeted sampling of endoscopically visible lesions as well as extensive random biopsies [14,15]. Also, it was thought to be important to distinguish IBD-related polypoid dysplasia (dysplasia-associated lesion or mass) from a sporadic adenoma, because the former was an indication for colectomy due to the high perceived probability of associated CRC, while the latter was usually treated by simple polypectomy [16]. However, along with advances in both endoscopic visualization and resection capability, it has become clear that the vast majority of IBD-related dysplastic lesions are endoscopically visible [17,18] and can be safely managed with endoscopic resection [19-22]. In fact, a systemic review of 10 studies reported 0.5% annual incidence of CRC in IBD patients with endoscopically resectable visible/polypoid dysplasia [19]. In light of these findings, the recent SCENIC (Surveillance for Colorectal Endoscopic Neoplasia Detection and Management in Inflammatory Bowel Disease Patients: International Consensus Recommendations) guidelines recommend that all visible/polypoid dysplastic lesions in IBD patients be managed with endoscopic resection (Fig. 1A), while invisible/flat dysplasia, particularly high-grade dysplasia (HGD), often necessitates colectomy (Fig. 1B) [13]. Indeed, sev-

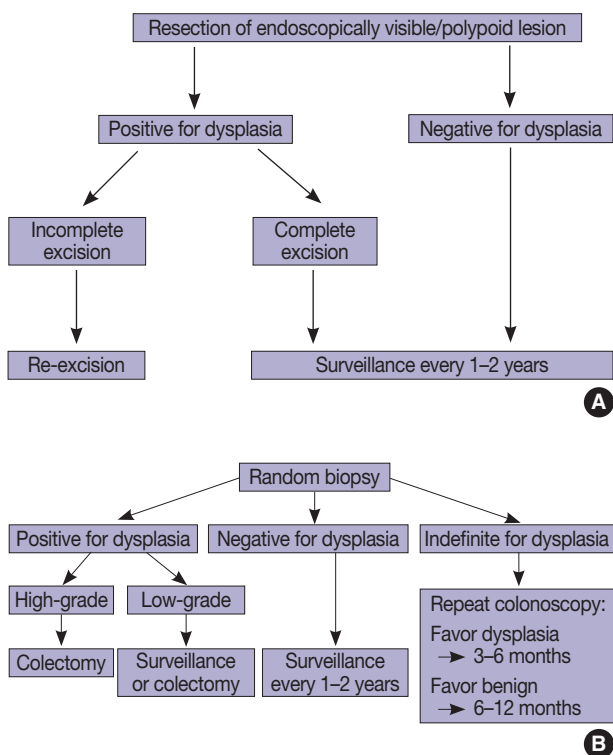


Fig. 1. Algorithms for management of endoscopically visible/polypoid dysplasia (A) versus invisible/flat dysplasia (B) in inflammatory bowel disease patients undergoing surveillance colonoscopies.

eral studies reported high rates of synchronous CRC (50%–67%) in colectomy specimens following a diagnosis of invisible/flat HGD [12,23-25]. Although the management of invisible/flat low-grade dysplasia (LGD) remains controversial due to its highly variable progression rates to advanced neoplasia (HGD or CRC) ranging from 0% to > 50% [23,26-37], colectomy is usually recommended for multifocal invisible/flat LGD [13].

There is evidence that IBD-related invisible/flat dysplasia may have different molecular features compared with visible/polypoid dysplasia. For instance, the frequency of large-scale chromosomal alterations resulting in aneuploidy as detected by DNA flow cytometry is significantly higher in invisible/flat dysplasia (41% for invisible/flat LGD and 93% for invisible/flat HGD) [37] than in low-grade conventional dysplasia (8%) or sporadic adenomas (9%) [38]. Likewise, using next-generation sequencing, Wanders et al. [39] reported that IBD-related dysplastic lesions that are often invisible or flat have more DNA copy number alterations (average number of gains and losses of 4.3 and 3.2, respectively) than sporadic adenomas (1.5 and 0.5, respectively). Overall, these findings indicate that invisible/flat dysplasia has more chromosomal instability than conventional dysplasia or sporadic adenomas, which may explain its frequent association with advanced neoplasia. In support of this, we also demonstrated that the presence of aneuploidy in the setting of invisible/flat LGD is a significant risk factor for subsequent detection of advanced neoplasia with the univariate and multivariate hazard ratios of 5.3 ($p = .006$) and 4.5 ($p = .040$), respectively [37].

POTENTIAL SIGNIFICANCE OF NON-CONVENTIONAL DYSPLASIA

Most of the literature on IBD-related dysplasia refers to conventional (or intestinal type) dysplasia, the most common form of dysplasia. Conventional dysplasia is defined by histologic features fundamentally identical to those of sporadic adenomas (Fig. 2A). In fact, the Riddell grading system proposed in 1983 for assessment of epithelial dysplasia in IBD mostly pertains to conventional dysplasia and categorizes IBD-related dysplasia into either LGD or HGD based on the degree of cytologic and/or architectural atypia [40]. LGD is characterized by crowded, elongated, hyperchromatic nuclei that are confined to the basal half of the cytoplasm, involving both crypts and surface epithelial cells (Fig. 2A), whereas HGD shows more severe cytologic (i.e., enlarged, rounder nuclei, pleomorphism, and loss of nuclear polarity) and/or architectural atypia (such as back-to-back glands

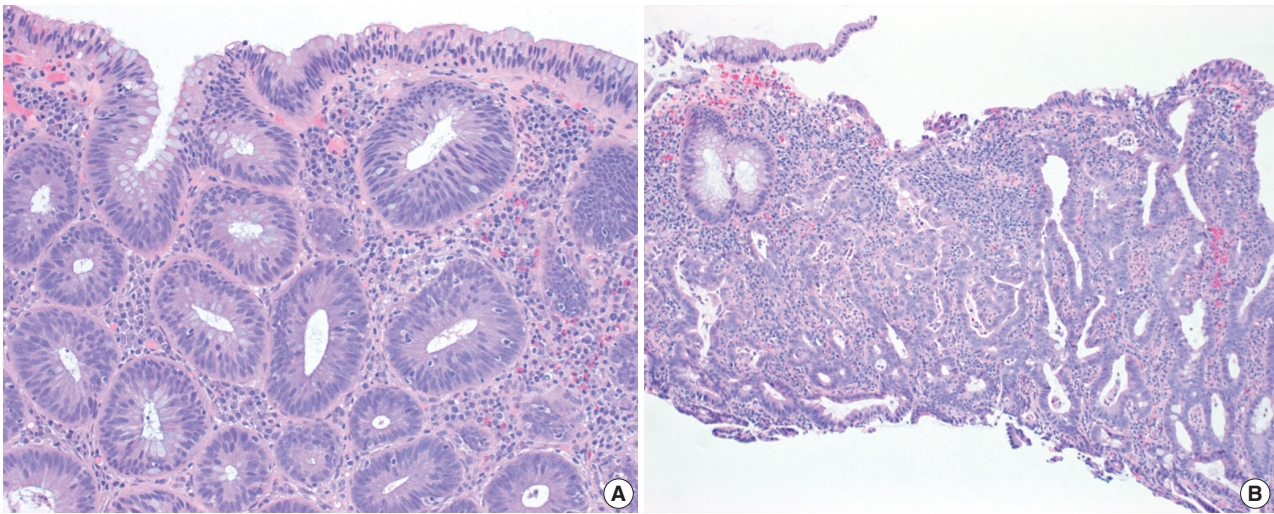


Fig. 2. Conventional dysplasia. (A) Invisible/flat low-grade dysplasia shows a tubular architecture lined by crowded, pencillate, hyperchromatic nuclei involving both crypts and surface epithelial cells. While goblet cells are reduced, they are easily identified. (B) Invisible/flat high-grade dysplasia shows severe cytologic and architectural atypia.

and cribriform formation) (Fig. 2B) [40]. Goblet cells may be reduced, but they are easily identified. Although a diagnosis of HGD does not require surface involvement, pathologists are accustomed to diagnosing dysplasia—including HGD—when dysplastic cells involve the surface epithelium. If nuclear atypia is limited to the crypt base without surface involvement, a diagnosis of “indefinite for dysplasia (IND)” or “reactive atypia” is often rendered, largely based on the assumption that true dysplasia does not maintain the capacity for maturation, as dysplastic cells migrate toward the surface epithelium.

Although pathologists have a good grasp of the morphologic criteria of conventional dysplasia, several unfamiliar morphologic patterns of dysplasia (collectively known as “non-conventional” dysplasia) have been recently described in IBD. There are at least seven subtypes, including (1) hypermucinous dysplasia; (2) crypt cell dysplasia; (3) dysplasia with increased Paneth cell differentiation; (4) goblet cell deficient dysplasia; (5) SSL-like dysplasia; (6) TSA-like dysplasia; and (7) serrated dysplasia NOS [38,41–43]. Although their clinicopathologic and molecular features are not fully characterized, in part due to the rarity of these subtypes and the likelihood that they are under-recognized, the recognition of these non-conventional subtypes is becoming increasingly important, as they often present as invisible/flat lesions, and at least some of them appear to have a higher malignant potential than conventional dysplasia or sporadic adenomas.

In this regard, we previously reported that non-conventional dysplasia, as a group, is common in a cohort of 58 IBD patients with CRC, detected in 45% [41]. Although it was often associ-

ated with conventional dysplasia, more commonly in the same colonic segment, up to 21% of the patients had non-conventional dysplasia only. Interestingly, despite its low-grade morphology (81% vs. 37% for conventional dysplasia; $p = .003$), non-conventional dysplasia was found in the same colonic segment as CRC or immediately adjacent to the CRC at a rate (85%) similar to conventional dysplasia (96%). Furthermore, CRC occurring in patients with non-conventional dysplasia only was more likely to be high-grade (poorly differentiated; 36%) than CRC that occurred in association with conventional dysplasia (10%) ($p = .026$). Taken together, these findings, for the first time, raised the possibility that non-conventional dysplasia may be associated with an increased risk for advanced neoplasia compared with conventional dysplasia.

In support of this argument, we recently reported that non-conventional dysplasia (38%) is more frequently associated with advanced neoplasia than conventional dysplasia (19%) ($p < .001$) [38]. Notably, non-conventional dysplasia with low-grade morphology had a significantly higher rate of aneuploidy (46%) than low-grade conventional dysplasia (8%, $p = .002$) or sporadic adenomas (9%, $p = .037$). Also, non-conventional dysplasia (41%) was more likely to present as invisible/flat dysplasia than conventional dysplasia (18%) ($p < .001$), suggesting that a current move towards performing only targeted biopsies in IBD patients [44] may miss some of these high-risk, non-conventional dysplastic lesions, and that IBD patients may potentially benefit from random biopsies in addition to targeted sampling of visible lesions.

In another larger multicenter study of 126 additional cases of

non-conventional dysplasia (including 55 hypermucinous, 45 crypt cell, and 26 goblet cell deficient dysplastic lesions), we demonstrated that 66% of the non-conventional dysplastic lesions presented as invisible/flat lesions (vs. 18% for conventional dysplasia; $p < .001$), and that 60% of the lesions were associated with subsequent detection of advanced neoplasia at the site of previous biopsy or in the same colonic segment within a mean follow-up time of 12 months (vs. 10% for conventional dysplasia; $p < .001$) (unpublished results). Overall, these findings support that non-conventional dysplasia has distinct clinicopathologic, molecular, and risk profiles compared with conventional dysplasia, underscoring the importance of recognizing non-conventional dysplasia and recommending its complete removal and/or careful follow-up.

SUBTYPES OF NON-CONVENTIONAL DYSPLASIA

Hypermucinous dysplasia

Hypermucinous dysplasia represents approximately 2% of all dysplastic lesions in IBD patients (Table 1) [38]. Most patients have a long history of IBD with a mean duration of 23 years. It is predominantly found in UC patients (86%) who often have a concurrent history of PSC (29%). Although the majority of hypermucinous dysplastic lesions have a polypoid endoscopic appearance with a mean size of 2.1 cm [38], up to 42% are endoscopically invisible or flat (unpublished results). Hypermucinous dysplasia shows a predilection for the left colon (57%).

Morphologically, hypermucinous dysplasia most often demonstrates a tubulovillous/villous architecture lined by tall, prominent mucinous cells representing > 50% of the lesion (Fig. 3A, B) [38,41,43]. Although low-grade dysplastic features are usually present in crypts, the degree of atypia tends to decrease towards the surface epithelium due to prominent mucinous differentiation, so one must be careful not to miss hypermucinous dysplasia when evaluating superficial fragments with hypermucinous features but without significant nuclear atypia (Fig. 3B). The presence of high-grade nuclear features is relatively uncommon (29%). Hypermucinous dysplasia can present either as a 'pure type' or a 'mixed type' with either conventional or another non-conventional subtype (most often with a serrated subtype) [41]. However, to be categorized as the mixed type, the hypermucinous component should represent > 50% of the lesion.

There is increasing evidence that hypermucinous dysplasia may be a marker of increased risk for advanced neoplasia. First, hypermucinous dysplasia was the most common non-con-

ventional subtype (42%) found in a cohort of 58 IBD patients with CRC [41]. Second, a significant proportion of hypermucinous dysplastic lesions (57%) were associated with advanced neoplasia [38]. In another study, we demonstrated that 19 (49%) of 39 low-grade hypermucinous dysplastic lesions were correlated with subsequent detection of HGD ($n = 9$, 23%) or adenocarcinoma ($n = 10$, 26%) at the site of previous biopsy or in the same colonic segment within a mean follow-up time of 11 months (unpublished results). Third, hypermucinous dysplasia, even without cytologic atypia, has been shown to have a higher rate of *KRAS* mutations (61%) than conventional LGD (4%, $p < .001$) or HGD (29%, $p > .05$) [45]. Similarly, we reported that the frequency of aneuploidy in low-grade hypermucinous dysplasia (80%) is significantly higher than that of low-grade conventional dysplasia (8%) or sporadic adenomas (9%) ($p < .001$) [38]. In fact, its rate of aneuploidy (80%) is similar to that of invisible/flat HGD (93%) [37]. Overall, these results indicate that despite its low-grade morphology, hypermucinous dysplasia shares similar molecular features with conventional HGD, suggesting that it may represent at least a high-risk low-grade lesion, if not already HGD. These findings also suggest that *KRAS* mutations and/or aneuploidy may contribute to the development of tubulovillous/villous growth, larger size, and/or higher biologic grade in hypermucinous dysplasia [46]. Similar to conventional dysplasia, hypermucinous dysplasia most likely develops via the chromosomal instability pathway involving multiple genetic mutations (including *KRAS*, *TP53*, and *APC* genes) and altered regulation of Wnt/ β -catenin pathway, as well as aneuploidy [47-50].

Crypt cell dysplasia

Crypt cell dysplasia accounts for approximately 4% of all dysplastic lesions in IBD patients (Table 1) [38], but it is likely an under-diagnosed entity. Most patients have a long history of IBD (mean duration: 15 years) and often have a concurrent history of PSC (43%) [38,42]. It is predominantly found in UC patients and shows a propensity for the left colon (79%). It exclusively presents as an invisible/flat lesion. When endoscopically visible, it has been described as "mild inflammation," "edema," "erythema," "friable," or "scarring" [42].

Histologically, crypt cell dysplasia is characterized by mildly enlarged, round-to-oval or slightly irregular, crowded, hyperchromatic nuclei limited to the crypt base without surface involvement or significant architectural atypia (Fig. 3C, D) [38,42,43]. Increased mitoses at the base of crypts are common (Fig. 3D). Although a few scattered cells may show more than mild nuclear enlargement and/or focal loss of nuclear polarity, there is no

Table 1. Morphologic, clinicopathologic, and molecular characteristics of non-conventional dysplastic subtypes

	Hypermucinous dysplasia	Crypt cell dysplasia	Dysplasia with increased Paneth cell differentiation	Goblet cell deficient dysplasia	Sessile serrated lesion-like dysplasia	Traditional serrated adenoma-like dysplasia	Serrated dysplasia, not otherwise specified
Defining morphologic features	Tall, prominent mucinous cells with typically mildly elongated, hyperchromatic nuclei	Mostly round-to-oval or slightly elongated, non-stratified nuclei with mild nuclear enlargement and crowding limited to the crypt base without surface involvement	Increased Paneth cell differentiation involving at least two contiguous dysplastic crypts in two different foci (beyond what is present in background mucosa)	Complete or near-complete absence of goblet cells	Dilatation at the crypt base, including dilated L- or inverted T-shaped crypts, at the interface with muscularis mucosa	Intensely eosinophilic cytoplasm and ectopic crypts	Serrated profile without definite features of sessile serrated lesion-like dysplasia or traditional serrated adenoma-like dysplasia
Endoscopic appearance	Often visible/polypoid	Usually invisible/flat	Usually visible/polypoid	Often invisible/flat	Usually visible/polypoid	Usually visible/polypoid	Usually visible/polypoid
Mean size (cm)	2.1	Not applicable	1.0	1.9 (when visible)	1.2	1.2	Unknown
Most common location	Left colon	Left colon	Right colon	Both right and left	Right colon	Left colon	Unknown
Most common histologic architecture	Tubulovillous/villous	Flat	Tubular	Tubular	Tubular	Tubulovillous/villous	Unknown
Association with PSC	Common	Common	Rare	Not uncommon	Rare	Rare	Unknown
Risk for HGD or CRC compared with conventional dysplasia	Higher	Higher	Similar	Higher	Similar	Similar	Unknown
Reported molecular alterations	Aneuploidy, <i>KRAS</i> , <i>TP53</i>	Aneuploidy, <i>TP53</i> , <i>KRAS</i>	Aneuploidy	Aneuploidy, <i>PIK3CA</i> , <i>TP53</i> , <i>KRAS</i>	<i>TP53</i> , <i>BRAF</i>	Aneuploidy, <i>KRAS</i> , <i>BRAF</i>	Unknown
Incidence (% of all dysplastic lesions)	Rare (2%)	Rare (4%)	Common (13%)	Rare (3%)	Rare (1%)	Rare (1%)	Rare (<1%)

PSC, primary sclerosing cholangitis; HGD, high-grade dysplasia; CRC, colorectal cancer.

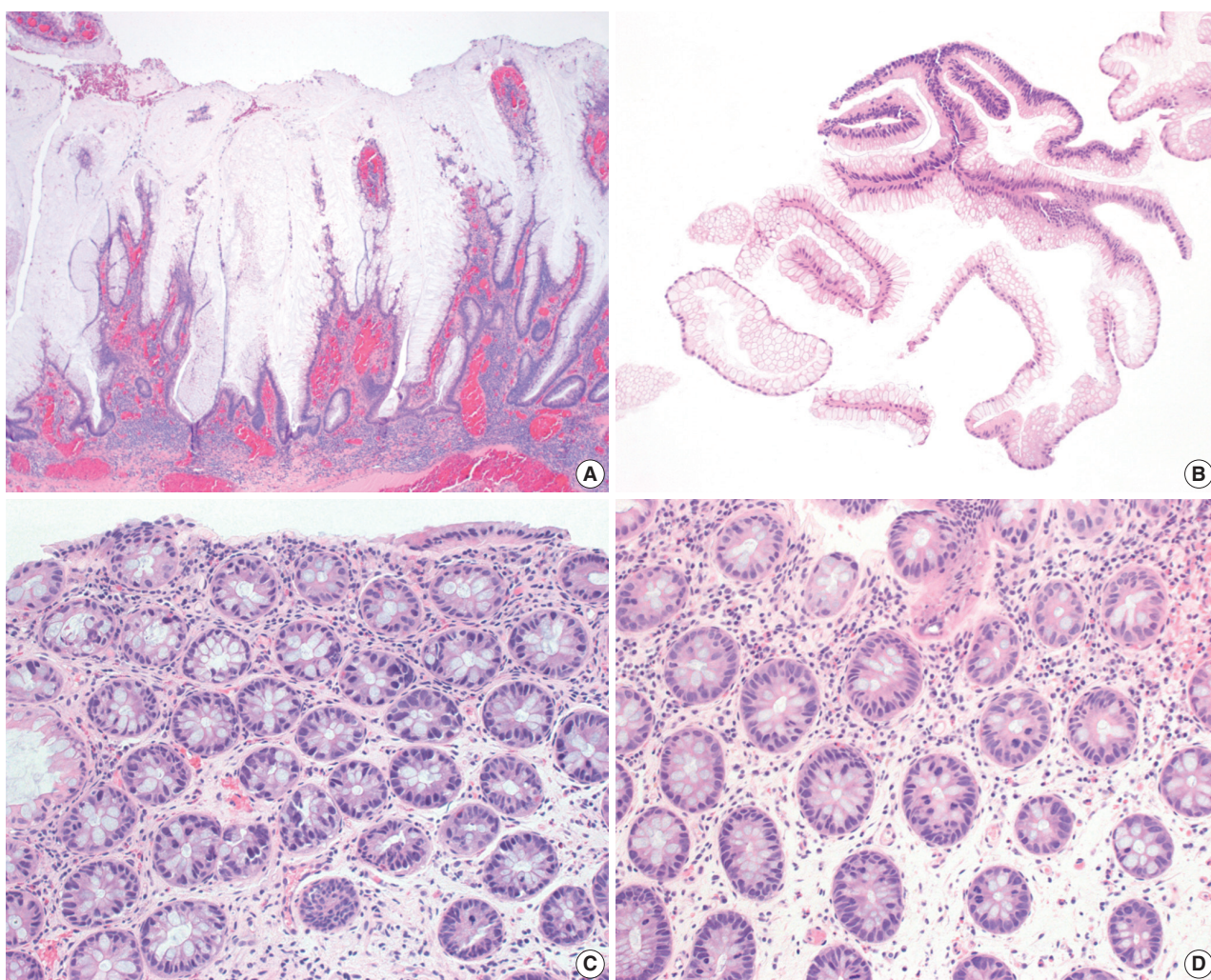


Fig. 3. Hypermucinous and crypt cell dysplasias. (A) Hypermucinous dysplasia demonstrates a tubulovillous lesion with mild nuclear atypia and prominent mucinous differentiation. (B) Superficial fragments of hypermucinous dysplasia show prominent mucinous cells with minimal to no nuclear atypia. (C, D) Crypt cell dysplasia is characterized by mostly round-to-oval or slightly elongated, hyperchromatic nuclei with mild nuclear enlargement and crowding limited to the crypt base without surface involvement. Increased mitoses are present (D).

unequivocal evidence of HGD. To avoid confusion with reactive changes, significant neutrophilic inflammation and/or ulceration should be absent. Immunohistochemical staining for p53 could be potentially useful to distinguish crypt cell dysplasia from reactive changes, as strong and diffuse p53 nuclear staining has been reported in up to 63% of crypt cell dysplastic lesions [42].

Similar to hypermucinous dysplasia, crypt cell dysplasia is considered a high-risk marker for advanced neoplasia. In support of this, we reported that six of seven patients (86%) with crypt cell dysplasia developed HGD ($n = 4$, 57%) or CRC ($n = 2$, 29%) in the same colonic segment within a mean follow-up time of 27 months [38,42]. Notably, all 14 biopsies with crypt cell dysplasia from the seven patients demonstrated aneuploidy [42]. This is consistent with our previous finding that invisible/

flat dysplasia in IBD patients is characterized by the high rate of aneuploidy (41% for invisible/flat LGD and 93% for invisible/flat HGD) [37]. Taken together, these findings indicate that crypt cell dysplasia likely represents at least high-risk LGD, if not already HGD. Other investigators also reported that *TP53* (43%) and *KRAS* (14%) mutations are common in crypt cell dysplasia, further confirming its dysplastic nature [47]. Of note, these results are very similar to what has been described in Barrett's esophagus-related "crypt dysplasia," which showed similar molecular alterations (i.e., aneuploidy and *TP53* mutations) that are normally found in traditional dysplasia with surface involvement [51].

In practice, it may be difficult to diagnose and/or grade crypt cell dysplasia in a consistent manner on histologic grounds alone.

In fact, we previously reported a poor interobserver agreement in the diagnosis and/or grading of crypt cell dysplasia [42]. Even though the majority of pathologists recognized its atypical morphology and diagnosed as IND, LGD, or HGD in 83% of their readings, a diagnosis of IND was made in 50% rather than either LGD (13%) or HGD (19%). As such, in challenging situations, we recommend that pathologists use the diagnostic term “crypt cell atypia” to describe similar changes and recommend a repeat colonoscopy within 3–6 months. If there is significant neutrophilic inflammation and/or ulceration in the areas of cytologic atypia, it may be more appropriate to make a diagnosis of IND and suggest a repeat colonoscopy within 3–6 months (Fig. 1B).

Dysplasia with increased Paneth cell differentiation

Dysplasia with increased Paneth cell differentiation is a common non-conventional subtype accounting for 51% of non-conventional dysplastic lesions and 13% of all dysplastic lesions in IBD patients (Table 1) [38]. The majority of affected patients have a long history of IBD (mean duration: 17 years), but a concurrent history of PSC is rare (9%). Dysplasia with increased Paneth cell differentiation most often presents as a polypoid lesion (70%) with a mean size of 1 cm. The right colon is most frequently involved (45%), and there appears to be a strong association with male sex (82%).

The defining histologic feature of dysplasia with increased Paneth cell differentiation is increased Paneth cell differentiation involving at least two contiguous dysplastic crypts in two different foci (beyond what is present in background mucosa) (Fig. 4A, B) [38,41,43]. It usually demonstrates a tubular architecture mostly lined by elongated, hyperchromatic nuclei involving both crypts and surface epithelial cells. Goblet cells may be reduced, but they are not absent or nearly-absent. Although scattered Paneth cells may be present in other dysplastic subtypes, they are not present in multiple crypts and in multiple foci as in dysplasia with increased Paneth cell differentiation, and the same degree of Paneth cell differentiation is always present in adjacent, non-dysplastic mucosa.

Unlike hypermucinous and crypt cell dysplasias, increased Paneth cell differentiation may be a marker of lower-risk lesions. In favor of this, we previously demonstrated that the risk of harboring advanced neoplasia in dysplasia with increased Paneth cell differentiation (15%) is compatible to that of conventional dysplasia (19%) ($p = .523$). Also, the rate of aneuploidy in low-grade lesions (12%) is similar to that of low-grade conventional dysplasia (8%, $p = 0.715$) or sporadic adenomas (9%, $p = .823$) [38]. These results are in agreement with our previous finding

that dysplasia with increased Paneth cell differentiation was a rare non-conventional subtype (11%) found in a cohort of 58 IBD patients with CRC [41].

Interestingly, sporadic Paneth cell-containing adenomas have been described in the literature with the reported frequency of 0.2% to 39% [52–55]. Even though these earlier studies defined the presence of even one Paneth cell as histologic evidence of increased Paneth cell differentiation, sporadic Paneth cell-containing adenomas appear to share similar clinicopathologic features with their IBD-related counterpart. For instance, Pai et al. [55] reported that sporadic Paneth cell-containing adenomas are more likely to occur in the right colon (85% vs. 56% for non-Paneth cell-containing adenomas; $p = .006$) and in male individuals (89% vs. 56% for non-Paneth cell-containing adenomas; $p = .002$). Also, Mahon et al. [53] demonstrated that sporadic Paneth cell-containing adenomas in the proximal ($p = .157$) and distal colon ($p = .797$) are not significantly associated with subsequent detection of CRC, compared with non-Paneth cell-containing adenomas.

Goblet cell deficient dysplasia

Goblet cell deficient dysplasia represents approximately 3% of all dysplastic lesions in IBD patients (Table 1) [38]. Most patients have a long history of IBD (mean duration: 17 years). Although a concurrent history of PSC is not uncommon (14%), it appears to be not as frequent as in patients with crypt cell dysplasia (43%) or hypermucinous dysplasia (29%). Goblet cell deficient dysplasia is often endoscopically invisible or flat (40%), but when endoscopically visible, it usually presents as a large polypoid lesion with a mean size of 1.9 cm. It is equally common in both right and left colon (40% each).

Morphologically, goblet cell deficient dysplasia is defined by a complete or near-complete absence of goblet cells, often leading to intensely eosinophilic cytoplasm (Fig. 4C, D) [38,41,43]. It predominantly shows a tubular architecture with low-grade dysplastic features involving both crypts and surface epithelial cells. However, up to 40% of goblet cell deficient dysplastic lesions may demonstrate HGD at diagnosis. Eosinophilic luminal secretion is another common histologic feature of goblet cell deficient dysplasia (Fig. 4C).

Similar to hypermucinous and crypt cell dysplasias, goblet cell deficient dysplasia may be another high-risk marker for advanced neoplasia. In support of this, as noted above, 40% of goblet cell deficient dysplastic lesions were associated with advanced neoplasia [38]. In another study, we demonstrated that 10 (59%) of 17 low-grade goblet cell deficient dysplastic lesions were corre-

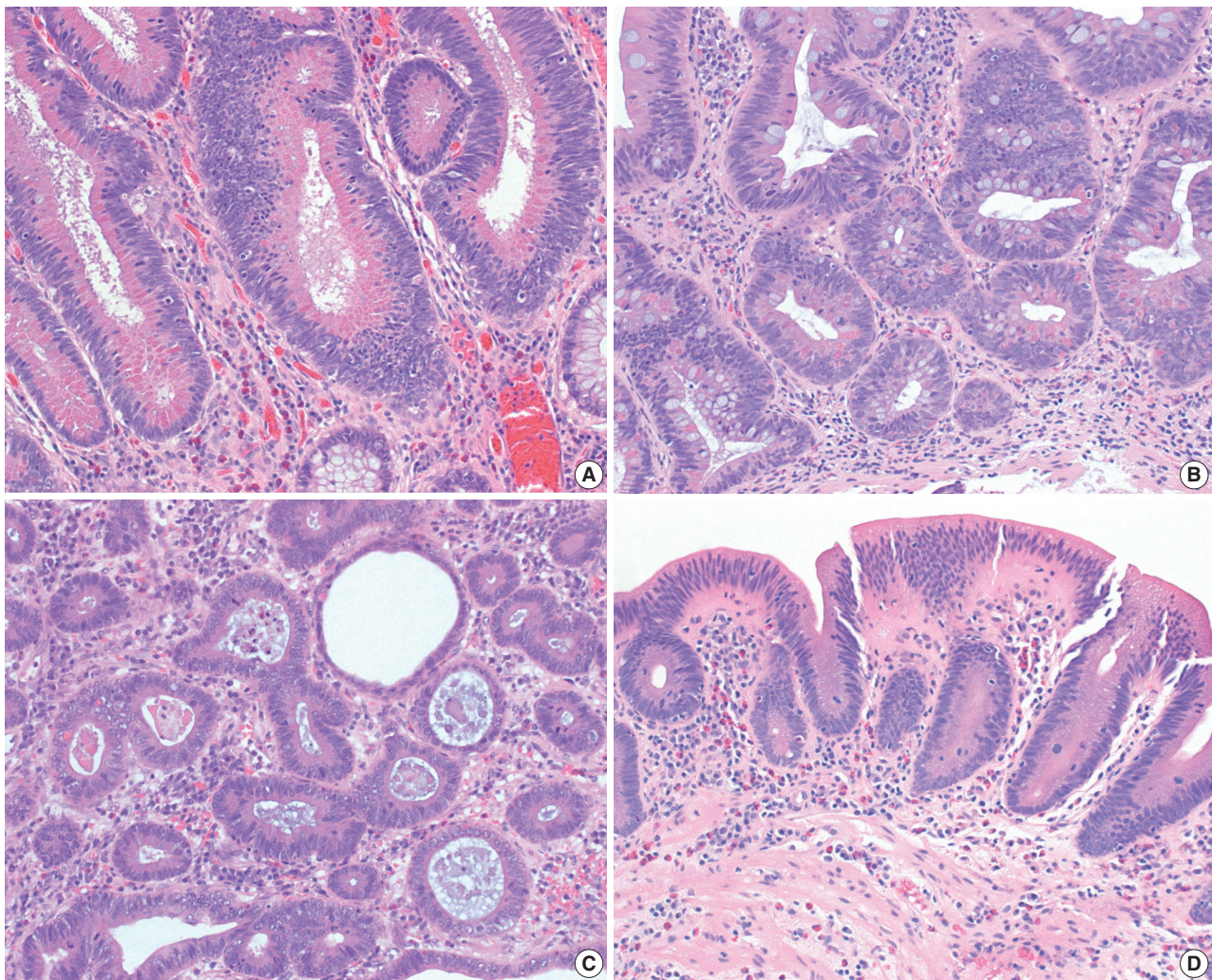


Fig. 4. Dysplasia with increased Paneth cell differentiation and goblet cell deficient dysplasia. (A, B) Dysplasia with increased Paneth cell differentiation shows increased Paneth cell differentiation involving multiple dysplastic crypts. (C, D) Goblet cell deficient dysplasia is defined by a complete or near-complete absence of goblet cells, leading to intensely bright eosinophilic cytoplasm. Eosinophilic luminal secretion is often seen in goblet cell deficient dysplasia (C).

lated with subsequent detection of HGD ($n = 4$, 24%) or adenocarcinoma ($n = 6$, 35%) at the site of previous biopsy or in the same colonic segment within a mean follow-up time of 13 months (unpublished results). Also, low-grade goblet cell deficient dysplasia appears to have a higher rate of aneuploidy (25%) than low-grade conventional dysplasia (8%) or sporadic adenomas (9%) [38]. Furthermore, other investigators reported the high rates of *TP53* (44%), *KRAS* (22%), and *PIK3CA* (56%) mutations in goblet cell deficient dysplasia [47].

Serrated dysplasia

This category includes three distinct subtypes, including SSL-like dysplasia, TSA-like dysplasia, and serrated dysplasia NOS [38,41,43]. Serrated dysplastic lesions usually present as polyp-

oid lesions with a mean size of 1.2 cm (Table 1) [38,56], and they are known to share similar clinicopathologic and molecular features with their sporadic counterparts [38,56-58]. For instance, while TSA-like dysplasia shows a propensity for the left colon, SSL-like dysplasia is more common in the right colon [38,56,57]. Ko et al. [56] also reported that low-grade serrated dysplasia in IBD patients often resembles sporadic TSA, occurs mainly in the left colon, and contains *KRAS* mutations (45%). In addition, serrated dysplasia, in particular SSL-like dysplasia, usually lacks aneuploidy, suggesting that an alternative serrated pathway (without resulting in aneuploidy) may be responsible for the development of at least a subset of SSL-like and TSA-like dysplastic lesions [38,58].

Histologically, SSL-like dysplasia is characterized by distorted

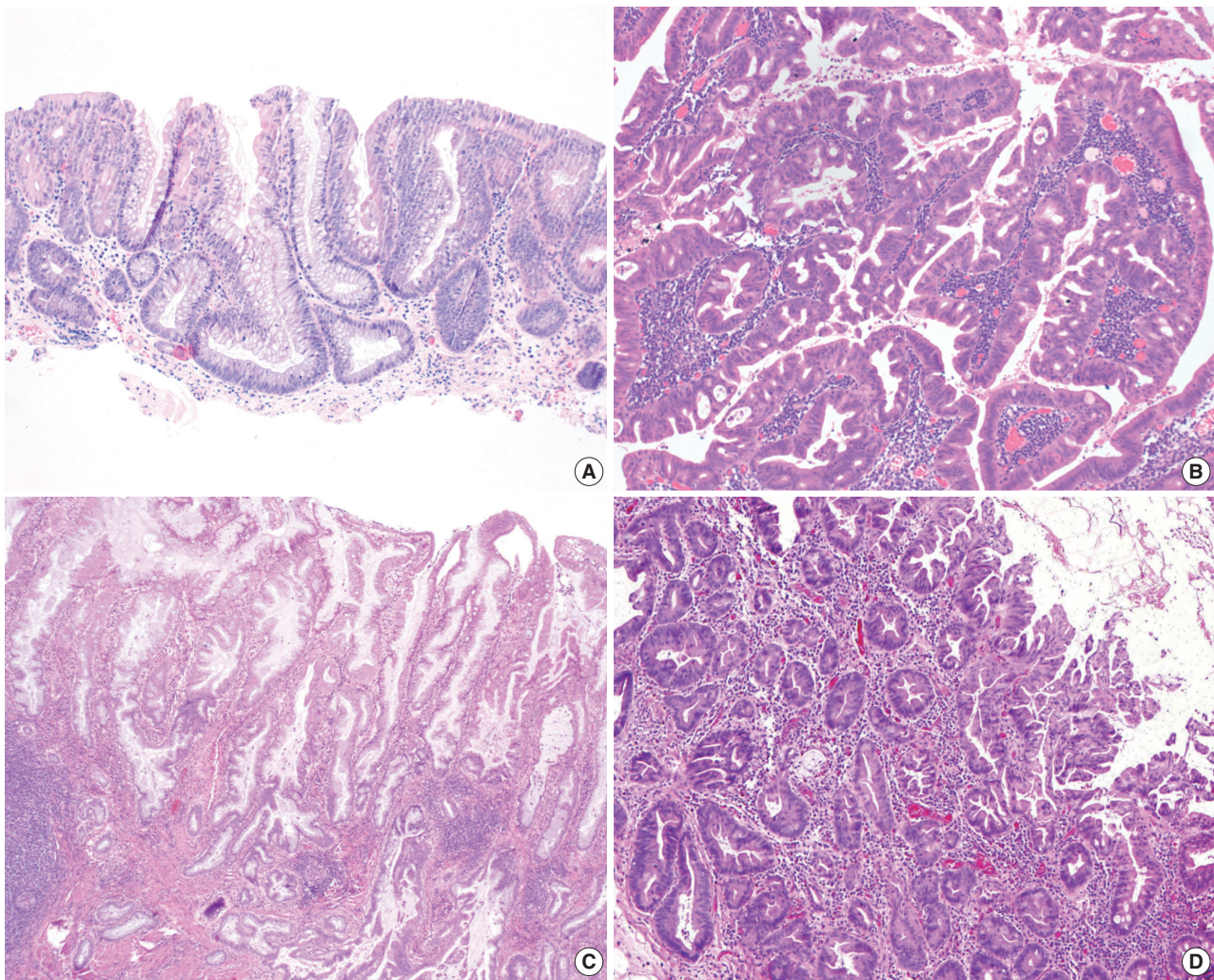


Fig. 5. Three subtypes of serrated dysplasia. (A) Sessile serrated lesion (SSL)-like dysplasia demonstrates a dilated L-shaped crypt at the interface with muscularis mucosa. (B) Traditional serrated adenoma (TSA)-like dysplasia shows villiform projections lined by elongated nuclei with intensely eosinophilic cytoplasm and ectopic crypts. (C) Serrated dysplasia not otherwise specified (NOS) shows a complex serrated architecture without definite features of SSL-like dysplasia or TSA-like dysplasia. (D) Another case of serrated dysplasia NOS mimics a hyperplastic polyp, but it shows full-thickness dysplasia with papillary or pseudopapillary changes on the surface epithelium.

serrated crypts with prominent basal crypt dilatation (i.e., dilated L- or inverted T-shaped crypts) at the interface with muscularis mucosa (Fig. 5A) [38,41,43]. TSA-like dysplasia most often demonstrates a tubulovillous/villous architecture lined by tall columnar cells with intensely eosinophilic cytoplasm and ectopic crypts (Fig. 5B) [38,41,43]. Serrated dysplasia NOS shows no definite features of SSL-like dysplasia or TSA-like dysplasia (Fig. 5C, D) [38,41,43]. Serrated dysplasia can co-exist with conventional dysplasia or another non-conventional subtype as a minor component, but to be classified as a specific serrated subtype, a serrated architecture should form the predominant feature representing > 50% of the lesion [38,41].

Although the natural history of serrated dysplasia is not well

defined in IBD patients, low-grade serrated dysplasia (which often resembles sporadic TSA) has been reported to have higher rates of advanced neoplasia (17% within 10 years, $p = .020$) and prevalent neoplasia (76%, $p < .001$) than serrated lesions without dysplasia (0% and 11%, respectively) [56]. Its 10-year rate of advanced neoplasia (17%) was similar to that of low-grade, non-serrated, conventional dysplasia (23%) [56]. Overall, these findings suggest that although serrated lesions that lack dysplasia seem to pose little risk for advanced neoplasia, those with LGD are associated with increased rates of synchronous and metachronous neoplasia. However, their risk of developing advanced neoplasia is probably compatible to that of conventional dysplasia (Table 1).

CONCLUSION

Non-conventional dysplasia in IBD has distinct clinicopathologic, molecular, and risk profiles compared with conventional dysplasia. Despite its low-grade morphology, non-conventional dysplasia, in particular hypermucinous, crypt cell, and goblet cell deficient dysplasias, has molecular alterations characteristic of conventional HGD (i.e., higher rates of aneuploidy and/or *KRAS* mutations) and appears to have a higher malignant potential than conventional dysplasia or sporadic adenomas. Therefore, it is important to recognize different non-conventional subtypes and recommend complete removal and/or careful follow-up. Also, a significant proportion of non-conventional dysplastic lesions present as invisible/flat lesions, suggesting that IBD patients may benefit from increased endoscopic surveillance with random biopsy sampling in addition to targeted biopsies.

Ethics Statement

Not applicable.

ORCID

Won-Tak Choi <https://orcid.org/0000-0002-6892-5881>

Conflicts of Interest

The author declares that he has no potential conflicts of interest.

Funding Statement

No funding to declare.

References

1. Ekbom A, Helmick C, Zack M, Adami HO. Ulcerative colitis and colorectal cancer: a population-based study. *N Engl J Med* 1990; 323: 1228-33.
2. Soderlund S, Brandt L, Lapidus A, et al. Decreasing time-trends of colorectal cancer in a large cohort of patients with inflammatory bowel disease. *Gastroenterology* 2009; 136: 1561-7.
3. Bernstein CN, Blanchard JF, Kliever E, Wajda A. Cancer risk in patients with inflammatory bowel disease: a population-based study. *Cancer* 2001; 91: 854-62.
4. Jess T, Rungoe C, Peyrin-Biroulet L. Risk of colorectal cancer in patients with ulcerative colitis: a meta-analysis of population-based cohort studies. *Clin Gastroenterol Hepatol* 2012; 10: 639-45.
5. Ekbom A, Helmick C, Zack M, Adami HO. Increased risk of large-bowel cancer in Crohn's disease with colonic involvement. *Lancet* 1990; 336: 357-9.
6. Eaden JA, Abrams KR, Mayberry JF. The risk of colorectal cancer in ulcerative colitis: a meta-analysis. *Gut* 2001; 48: 526-35.
7. Soetikno RM, Lin OS, Heidenreich PA, Young HS, Blackstone MO. Increased risk of colorectal neoplasia in patients with primary sclerosing cholangitis and ulcerative colitis: a meta-analysis. *Gastrointest Endosc* 2002; 56: 48-54.
8. Beaugerie L, Svrcek M, Seksik P, et al. Risk of colorectal high-grade dysplasia and cancer in a prospective observational cohort of patients with inflammatory bowel disease. *Gastroenterology* 2013; 145: 166-75.
9. Lutgens MW, Oldenburg B, Siersema PD, et al. Colonoscopic surveillance improves survival after colorectal cancer diagnosis in inflammatory bowel disease. *Br J Cancer* 2009; 101: 1671-5.
10. Karlen P, Kornfeld D, Brostrom O, Lofberg R, Persson PG, Ekbom A. Is colonoscopic surveillance reducing colorectal cancer mortality in ulcerative colitis? A population based case control study. *Gut* 1998; 42: 711-4.
11. Eaden J, Abrams K, Ekbom A, Jackson E, Mayberry J. Colorectal cancer prevention in ulcerative colitis: a case-control study. *Aliment Pharmacol Ther* 2000; 14: 145-53.
12. Choi CH, Rutter MD, Askari A, et al. Forty-year analysis of colonoscopic surveillance program for neoplasia in ulcerative colitis: an updated overview. *Am J Gastroenterol* 2015; 110: 1022-34.
13. Laine L, Kaltenbach T, Barkun A, et al. SCENIC international consensus statement on surveillance and management of dysplasia in inflammatory bowel disease. *Gastrointest Endosc* 2015; 81: 489-501.
14. Farraye FA, Odze RD, Eaden J, et al. AGA medical position statement on the diagnosis and management of colorectal neoplasia in inflammatory bowel disease. *Gastroenterology* 2010; 138: 738-45.
15. Leighton JA, Shen B, Baron TH, et al. ASGE guideline: endoscopy in the diagnosis and treatment of inflammatory bowel disease. *Gastrointest Endosc* 2006; 63: 558-65.
16. Odze RD. Adenomas and adenoma-like DALMs in chronic ulcerative colitis: a clinical, pathological, and molecular review. *Am J Gastroenterol* 1999; 94: 1746-50.
17. Rutter MD, Saunders BP, Wilkinson KH, Kamm MA, Williams CB, Forbes A. Most dysplasia in ulcerative colitis is visible at colonoscopy. *Gastrointest Endosc* 2004; 60: 334-9.
18. Rubin DT, Rothe JA, Hetzel JT, Cohen RD, Hanauer SB. Are dysplasia and colorectal cancer endoscopically visible in patients with ulcerative colitis? *Gastrointest Endosc* 2007; 65: 998-1004.
19. Wanders LK, Dekker E, Pullens B, Bassett P, Travis SP, East JE. Cancer risk after resection of polypoid dysplasia in patients with longstanding ulcerative colitis: a meta-analysis. *Clin Gastroenterol Hepatol* 2014; 12: 756-64.
20. Blonski W, Kundu R, Furth EF, Lewis J, Aberra F, Lichtenstein GR. High-grade dysplastic adenoma-like mass lesions are not an indication for colectomy in patients with ulcerative colitis. *Scand J Gastroenterol* 2008; 43: 817-20.
21. Odze RD, Farraye FA, Hecht JL, Hornick JL. Long-term follow-up after polypectomy treatment for adenoma-like dysplastic lesions in ulcerative colitis. *Clin Gastroenterol Hepatol* 2004; 2: 534-41.
22. Kisiel JB, Loftus EV Jr, Harmsen WS, Zinsmeister AR, Sandborn WJ. Outcome of sporadic adenomas and adenoma-like dysplasia in patients with ulcerative colitis undergoing polypectomy. *Inflamm Bowel Dis* 2012; 18: 226-35.
23. Connell WR, Lennard-Jones JE, Williams CB, Talbot IC, Price AB, Wilkinson KH. Factors affecting the outcome of endoscopic surveillance for cancer in ulcerative colitis. *Gastroenterology* 1994; 107: 934-44.
24. Friedman S, Rubin PH, Bodian C, Goldstein E, Harpaz N, Present DH. Screening and surveillance colonoscopy in chronic Crohn's colitis. *Gastroenterology* 2001; 120: 820-6.
25. Hata K, Watanabe T, Kazama S, et al. Earlier surveillance colonoscopy programme improves survival in patients with ulcerative colitis.

- tis associated colorectal cancer: results of a 23-year surveillance programme in the Japanese population. *Br J Cancer* 2003; 89: 1232-6.
26. Bernstein CN, Shanahan F, Weinstein WM. Are we telling patients the truth about surveillance colonoscopy in ulcerative colitis? *Lancet* 1994; 343: 71-4.
 27. Thomas T, Abrams KA, Robinson RJ, Mayberry JF. Meta-analysis: cancer risk of low-grade dysplasia in chronic ulcerative colitis. *Aliment Pharmacol Ther* 2007; 25: 657-68.
 28. Jess T, Loftus EV Jr, Velayos FS, et al. Incidence and prognosis of colorectal dysplasia in inflammatory bowel disease: a population-based study from Olmsted County, Minnesota. *Inflamm Bowel Dis* 2006; 12: 669-76.
 29. Ullman T, Croog V, Harpaz N, Sachar D, Itzkowitz S. Progression of flat low-grade dysplasia to advanced neoplasia in patients with ulcerative colitis. *Gastroenterology* 2003; 125: 1311-9.
 30. Ullman TA, Loftus EV Jr, Kakar S, Burgart LJ, Sandborn WJ, Tremaine WJ. The fate of low grade dysplasia in ulcerative colitis. *Am J Gastroenterol* 2002; 97: 922-7.
 31. van Schaik FD, ten Kate FJ, Offerhaus GJ, et al. Misclassification of dysplasia in patients with inflammatory bowel disease: consequences for progression rates to advanced neoplasia. *Inflamm Bowel Dis* 2011; 17: 1108-16.
 32. Befrits R, Ljung T, Jaramillo E, Rubio C. Low-grade dysplasia in extensive, long-standing inflammatory bowel disease: a follow-up study. *Dis Colon Rectum* 2002; 45: 615-20.
 33. Venkatesh PG, Jegadeesan R, Gutierrez NG, Sanaka MR, Navaneethan U. Natural history of low grade dysplasia in patients with primary sclerosing cholangitis and ulcerative colitis. *J Crohns Colitis* 2013; 7: 968-73.
 34. Pekow JR, Hetzel JT, Rothe JA, et al. Outcome after surveillance of low-grade and indefinite dysplasia in patients with ulcerative colitis. *Inflamm Bowel Dis* 2010; 16: 1352-6.
 35. Zisman TL, Bronner MP, Rulyak S, et al. Prospective study of the progression of low-grade dysplasia in ulcerative colitis using current cancer surveillance guidelines. *Inflamm Bowel Dis* 2012; 18: 2240-6.
 36. Navaneethan U, Jegadeesan R, Gutierrez NG, et al. Progression of low-grade dysplasia to advanced neoplasia based on the location and morphology of dysplasia in ulcerative colitis patients with extensive colitis under colonoscopic surveillance. *J Crohns Colitis* 2013; 7: e684-91.
 37. Tsai JH, Rabinovitch PS, Huang D, et al. Association of aneuploidy and flat dysplasia with development of high-grade dysplasia or colorectal cancer in patients with inflammatory bowel disease. *Gastroenterology* 2017; 153: 1492-5.
 38. Lee H, Rabinovitch PS, Mattis AN, Lauwers GY, Choi WT. Non-conventional dysplasia in inflammatory bowel disease is more frequently associated with advanced neoplasia and aneuploidy than conventional dysplasia. *Histopathology* 2020 Nov 5 [Epub]. <https://doi.org/10.1111/his.14298>.
 39. Wanders LK, Cordes M, Voorham Q, et al. IBD-associated dysplastic lesions show more chromosomal instability than sporadic adenomas. *Inflamm Bowel Dis* 2020; 26: 167-80.
 40. Riddell RH, Goldman H, Ransohoff DF, et al. Dysplasia in inflammatory bowel disease: standardized classification with provisional clinical applications. *Hum Pathol* 1983; 14: 931-68.
 41. Choi WT, Yozu M, Miller GC, et al. Nonconventional dysplasia in patients with inflammatory bowel disease and colorectal carcinoma: a multicenter clinicopathologic study. *Mod Pathol* 2020; 33: 933-43.
 42. Wen KW, Umetsu SE, Goldblum JR, et al. DNA flow cytometric and interobserver study of crypt cell atypia in inflammatory bowel disease. *Histopathology* 2019; 75: 578-88.
 43. Pereira D, Kovari B, Brown I, et al. Non-conventional dysplasias of the tubular gut: a review and illustration of their histomorphological spectrum. *Histopathology* 2020 Oct 30 [Epub]. <https://doi.org/10.1111/his.14294>.
 44. Watanabe T, Ajioka Y, Mitsuyama K, et al. Comparison of targeted vs random biopsies for surveillance of ulcerative colitis-associated colorectal cancer. *Gastroenterology* 2016; 151: 1122-30.
 45. Andersen SN, Lovig T, Clausen OP, Bakka A, Fausa O, Rognum TO. Villous, hypermucinous mucosa in long standing ulcerative colitis shows high frequency of K-ras mutations. *Gut* 1999; 45: 686-92.
 46. Maltzman T, Knoll K, Martinez ME, et al. Ki-ras proto-oncogene mutations in sporadic colorectal adenomas: relationship to histologic and clinical characteristics. *Gastroenterology* 2001; 121: 302-9.
 47. Gui X, Kobel M, Ferraz JG, et al. Histological and molecular diversity and heterogeneity of precancerous lesions associated with inflammatory bowel diseases. *J Clin Pathol* 2020; 73: 391-402.
 48. Vogelstein B, Fearon ER, Hamilton SR, et al. Genetic alterations during colorectal-tumor development. *N Engl J Med* 1988; 319: 525-32.
 49. Ried T, Knutzen R, Steinbeck R, et al. Comparative genomic hybridization reveals a specific pattern of chromosomal gains and losses during the genesis of colorectal tumors. *Genes Chromosomes Cancer* 1996; 15: 234-45.
 50. Meijer GA, Hermsen MA, Baak JP, et al. Progression from colorectal adenoma to carcinoma is associated with non-random chromosomal gains as detected by comparative genomic hybridisation. *J Clin Pathol* 1998; 51: 901-9.
 51. Lomo LC, Blount PL, Sanchez CA, et al. Crypt dysplasia with surface maturation: a clinical, pathologic, and molecular study of a Barrett's esophagus cohort. *Am J Surg Pathol* 2006; 30: 423-35.
 52. Joo M, Shahsafaei A, Odze RD. Paneth cell differentiation in colonic epithelial neoplasms: evidence for the role of the Apc/beta-catenin/Tcf pathway. *Hum Pathol* 2009; 40: 872-80.
 53. Mahon M, Xu J, Yi X, Liu X, Gao N, Zhang L. Paneth cell in adenomas of the distal colorectum is inversely associated with synchronous advanced adenoma and carcinoma. *Sci Rep* 2016; 6: 26129.
 54. Bansal M, Fenoglio CM, Robboy SJ, King DW. Are metaplasias in colorectal adenomas truly metaplasias? *Am J Pathol* 1984; 115: 253-65.
 55. Pai RK, Rybicki LA, Goldblum JR, Shen B, Xiao SY, Liu X. Paneth cells in colonic adenomas: association with male sex and adenoma burden. *Am J Surg Pathol* 2013; 37: 98-103.
 56. Ko HM, Harpaz N, McBride RB, et al. Serrated colorectal polyps in inflammatory bowel disease. *Mod Pathol* 2015; 28: 1584-93.
 57. Yang C, Tarabishy Y, Dassopoulos T, Nalbantoglu I. Clinical, histologic, and immunophenotypic features of serrated polyps in patients with inflammatory bowel disease. *Gastroenterology Res* 2018; 11: 355-60.
 58. Choi WT, Wen KW, Rabinovitch PS, Huang D, Mattis AN, Gill RM. DNA content analysis of colorectal serrated lesions detects an aneuploid subset of inflammatory bowel disease-associated serrated epithelial change and traditional serrated adenomas. *Histopathology* 2018; 73: 464-72.

Histologically confirmed distant metastatic urothelial carcinoma from the urinary bladder: a retrospective review of one institution's 20-year experience

Youngeun Yoo, Junghye Lee, Heae Surng Park, Min-Sun Cho, Sun Hee Sung, Sanghui Park, Eunoo Choi

Department of Pathology, Ewha Womans University College of Medicine, Seoul, Korea

Background: Urothelial carcinoma (UC) accounts for roughly 90% of bladder cancer, and has a high propensity for diverse differentiation. Recently, certain histologic variants of UC have been recognized to be associated with unfavorable clinical outcomes. Several UC studies have also suggested that tumor budding is a poor prognostic marker. Distant metastasis of UC after radical cystectomy is not uncommon. However, these metastatic lesions are not routinely confirmed with histology. **Methods:** We investigated the histopathologic features of 13 cases of UC with biopsy-proven distant metastases, with a special emphasis on histologic variants and tumor budding. **Results:** Lymph nodes (6/13, 46%) were the most common metastatic sites, followed by the lung (4/13, 31%), liver (4/13, 31%), and the adrenal gland (2/13, 15%). The histologic variants including squamous (n=1), micropapillary (n=4), and plasmacytoid (n=1) variants in five cases of UC. Most histologic variants (4/5, 80%) of primary UCs appeared in the metastatic lesions. In contrast, high-grade tumor budding was detected in six cases (46%), including one case of non-muscle invasive UC. Our study demonstrates that histologic variants are not uncommonly detected in distant metastatic UCs. Most histologic variants seen in primary UCs persist in the distant metastatic lesions. In addition, high-grade tumor budding, which occurs frequently in primary tumors, may contribute to the development of distant metastasis. **Conclusions:** Therefore, assessing the presence or absence of histologic variants and tumor budding in UCs of the urinary bladder, even in non-muscle invasive UCs, may be useful to predict distant metastasis.

Key Words: Bladder neoplasms; Distant metastasis; Urothelial carcinoma; Histologic variant; Tumor budding

Received: September 25, 2020 **Revised:** October 9, 2020 **Accepted:** October 19, 2020

Corresponding Author: Eunoo Choi, MD, Department of Pathology, Ewha Womans University College of Medicine, 260 Gonghang-daero, Gangseo-gu, Seoul 07804, Korea
Tel: +82-2-2650-5194, Fax: +82-2-2650-2879, E-mail: euno1103@hanmail.net

Bladder cancer is the sixth most prevalent cancer and ninth leading cause of cancer death in men worldwide [1]. Urothelial carcinoma comprises approximately 90% of bladder cancers, and exhibits a great propensity for divergent differentiation [2]. Reflecting this morphologic diversity, histologic variants have been proposed to define urothelial carcinoma with distinctive histomorphology that differs from that of conventional urothelial carcinoma [2,3]. The World Health Organization (WHO) recently classified urothelial cancers into 13 histologic variants [4]. There is also accumulating evidence regarding the clinical relevance of histologic variants with regard to prognosis and response to treatment. Therefore, it is becoming increasingly important to recognize the histologic variant [3,5]. Several histologic variants, including squamous differentiation, micropapillary carcinoma, plasmacytoid, sarcomatoid, and nested variants, are as-

sociated with unfavorable clinical outcomes [6-11]. These histological variants frequently persist, even in metastatic tumors [6].

In addition to histologic variants, tumor budding has also been proposed as a poor prognostic indicator [12,13]. Tumor budding is defined by the presence of single tumor cells or clusters of fewer than five cancer cells at the invasive front. It has been recognized as an adverse prognostic factor in several types of cancer, especially in colorectal cancer [14-17]. Tumor budding is considered to represent the epithelial to mesenchymal transition by which tumor cells achieve migratory and invasive properties for metastasis [18].

Radical cystectomy is the gold standard treatment for patients with muscle-invasive bladder cancer. Based on recent data, patients with non-muscle invasive bladder cancer harboring micropapillary carcinoma or plasmacytoid variants are also considered

candidates for early radical cystectomy due to the aggressive clinical course [2,6,9].

Distant metastasis occurs in 10%–29% of patients with bladder cancer during their disease course [19]. Once distant metastasis develops, the long-term prognosis is generally poor [20]. Certain histologic variants in bladder cancer, including micropapillary carcinoma, the plasmacytoid variant, and the sarcomatoid variant, are associated with a high tendency to develop distant metastasis [8,10,21,22]. However, few studies have evaluated the histopathologic parameters and prevalence of histologic variants in metastatic urothelial carcinoma of distant metastatic sites, because histologic confirmation is rarely performed in this setting.

In this study, we analyzed the histopathologic findings of 13 cases of urothelial carcinomas of the urinary bladder with histologically confirmed distant metastases. We studied the correlation between the histomorphology of the primary tumors and that of subsequent distant metastases with an emphasis on the histologic variants. We also assessed various histopathologic parameters, including tumor budding.

MATERIALS AND METHODS

Case selection

A retrospective chart review was conducted of 477 patients with urothelial carcinoma of the urinary bladder who were treated by radical cystectomy at Ewha Womans University Mokdong Hospital between 1997 and 2017. Twelve of the 477 patients with histologically confirmed distant metastasis were selected for inclusion in this study. Additionally, one patient who was diagnosed with urothelial carcinoma by transurethral resection of the bladder and needle biopsy of the liver was included. The following clinical data were obtained from the medical records: sex, age, procedure, primary tumor size, metastatic site, biopsy site, tumor stage, and follow-up data.

Histologic evaluation

All hematoxylin and eosin stained slides from the 13 patients were reviewed by two uropathologists (SP and EC). The stage, grade, and histologic variants were reclassified according to the Cancer Staging Manual of the American Joint Committee on Cancer, 8th edition and the 2016 WHO/International Society of Urologic Pathology grading system [4,23]. Histologic variants were compared between the matched primary and metastatic tumors. Data concerning lymphovascular invasion, perineural invasion, accompanying urothelial carcinoma in situ, and tumor budding were recorded. Tumor budding was assessed with hema-

toxylin and eosin staining. Tumor budding was defined by the presence of isolated tumor cells or small groups of fewer than five cancer cells at the invasion front [14]. Tumor budding foci were counted in hot spots under $\times 200$ magnification. Tumor budding was regarded as high-grade when 10 or more budding foci were identified [24].

IHC staining

Immunohistochemical (IHC) staining for α -fetoprotein (AFP; 1:1,000, clone C3, mouse monoclonal, Novocastra, Newcastle upon Tyne, UK) was performed on 4- μ m thick slides using an automated immunostainer (BOND MAX, Leica Biosystem, Newcastle upon Tyne, UK) following the manufacturer's protocol. We performed immunostaining for AFP in one case with hepatic feature. In this case, most tumor cells demonstrated cytoplasmic expression for AFP.

RESULTS

Baseline features

The clinical features of the 13 patients are summarized in Table 1. All 13 cases arose primarily from the urinary bladder. Ten patients (77%) were men, and the median age was 59 years (range, 38 to 76 years). Twelve patients were treated with radical cystectomy for urothelial carcinoma of the urinary bladder, and one patient underwent a transurethral resection of bladder tumor with concurrent liver metastasis. The primary tumor size (maximum tumor diameter by pathological report) ranged from 0.5 to 8.5 cm (median, 3.5 cm). Clinically, eight (62%) distant metastatic lesions presented as solitary masses, while multiple metastatic lesions were detected in five cases (38%). Lymph nodes were the most frequent distant metastatic site (46%), followed by the lung (38%), liver (31%), and adrenal gland (15%). The biopsy sites of distant metastatic tumors are presented in Table 1. Regarding pathologic tumor stage (pT), 10 cases (77%) were classified as muscle-invasive urothelial carcinoma (pT2–T3), and three (23%) were classified as non-muscle-invasive urothelial carcinoma (pT1). The median follow-up duration was 47 months (range, 8 to 151 months). The median interval from the initial diagnosis of the primary lesion to that of distant metastasis was 25 months (range, 0 to 123 months).

Histopathologic features

The overall histopathologic findings are summarized in Table 2. Eight cases (62%) presented with conventional high-grade urothelial carcinoma. Histologic variants were present in the pure

Table 1. Baseline patient characteristics

Case	Sex	Age (yr)	Operation	Primary tumor size (cm)	Clinical distant metastatic sites	Bx site of distant metastatic lesion	pTNM	F/U (mo)	Interval (mo)
1	M	59	RC	8.5, multiple	Lung	Lung	pT2N0M1b	47	19
2	M	38	RC	0.5 (x2)	Liver, neck LN	Neck LN	pT2N0M1b	46	25
3	M	76	TURBT	NA	Liver	Liver	NA	22	0
4	M	55	RC	3.5, multiple	Colon, peritoneal seeding	Colon	pT3N2M1b	8	8
5	M	58	RC	2.3, multiple	Liver, adrenal gland, inguinal, retrocaval, aortocaval LNs	Inguinal LN	pT3N2M1b	30	13
6	M	74	RC	1.5	Axillary LN	Axillary LN	pT2N0M1a	151	123
7	F	59	RC	3.5	Liver	Liver	pT2N1M1b	43	28
8	M	64	RC	4.5	Adrenal gland	Adrenal gland	pT3N0M1b	68	6
9	F	64	RC	6, multiple	Lung, vagina, right rectus muscle, mediastinal LN	Lung	pT1N0M1b	76	60
10	M	62	RC	2.5	Neck LN	Neck LN	pT1NXM1a	64	31
11	F	69	RC	2.5	Lung	Lung	pT3N0M1b	90	61
12	M	55	RC	3.8	Lung (both)	Lung	pT3N1M1b	16	16
13	M	59	RC	4	Inguinal LN	Inguinal LN	pT1N0M1a	61	58

Bx, biopsy; F/U, follow-up; RC, radical cystectomy; LN, lymph node; TURBT, transurethral resection of bladder tumor; NA, non-applicable.

Table 2. Comparison of histologic components between primary and distant metastatic tumors

Case No.	Stage	Primary tumor histology	LVI	NI	CIS	TB	Distant metastatic tumor histology
1	pT2N0M1b	Conventional UC with MPC (3%)	+	-	-	+	MPC (100%)
2	pT2N0M1b	Conventional UC	-	+	+	-	Conventional UC
3	NA	AFP-producing type UC	+	NA	-	NA	AFP-producing type UC
4	pT3N2M1b	Conventional UC with MPC (10%) and squamous differentiation (70%)	+	+	+	+	Squamous differentiation (100%)
5	pT3N2M1b	Conventional UC	+	+	+	-	Conventional UC
6	pT2N0M1a	Plasmacytoid variant (100%)	-	-	+	-	Plasmacytoid variant (100%)
7	pT2N1M1b	Conventional UC with MPC (20%)	+	-	+	+	Conventional UC
8	pT3N0M1b	Conventional UC	+	+	+	+	Conventional UC
9	pT1N0M1b	Conventional UC	-	-	+	+	Conventional UC
10	pT1NXM1a	Conventional UC	+	-	+	-	Conventional UC with squamous (1%)
11	pT3N0M1b	Conventional UC with MPC (3%)	+	+	+	+	Conventional UC with mpc (1%)
12	pT3N1M1b	Conventional UC	+	+	+	-	Conventional UC
13	pT1N0M1a	Conventional UC	-	-	-	-	Conventional UC

LVI, lymphovascular invasion; NI, neural invasion; CIS, carcinoma in situ; TB, tumor budding; UC, urothelial carcinoma; MPC, micropapillary carcinoma component; NA, non-applicable; AFP, α -fetoprotein.

form in one case (1/13, 8%) and mixed with conventional high-grade urothelial carcinoma in four cases (4/13, 31%). Four of these mixed cases (cases 1, 4, 7, and 11) had a micropapillary carcinoma component (3%–20%) and 1 (case 4) had concurrent squamous differentiation (70%). One case was diagnosed as an AFP-producing urothelial carcinoma. Lymphovascular and perineural invasion were identified in nine cases (69%) and six cases (46%), respectively. Most cases (77%) had concomitant urothelial carcinoma in situ. High-grade tumor budding was identified in six cases (46%) (cases 1, 4, 7, 8, 9, and 11) (Fig. 1).

Histologic evaluation of the metastatic carcinomas was available in all 13 cases. Histologic variants were noted in the metastatic sites in five of 13 cases (38%). Most of these histologic vari-

ants (80%, 4/5) were also identified in the primary tumors. In case 1, the metastatic tumor was entirely composed of micropapillary carcinoma, which was focally present (3%) in the corresponding primary tumor (Fig. 2A, B). Although the primary tumor of case 4 had components of micropapillary carcinoma (10%) and squamous differentiation (70%), the corresponding metastatic tumor only demonstrated carcinoma cells with squamous differentiation (Fig. 2C, D). The primary tumor in case 6 was considered a plasmacytoid variant, which was maintained at the metastatic site (Fig. 2E, F). In case 10, the primary tumor was a conventional high-grade urothelial carcinoma, which persisted in the corresponding metastatic tumor along with focal squamous differentiation (1%). Squamous differentiation was

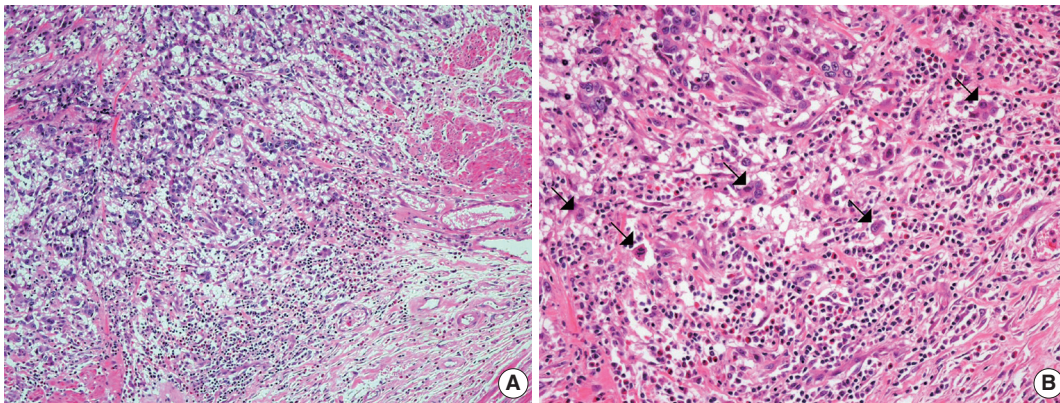


Fig. 1. Representative morphology of tumor budding at the invasive front. (A, B) Hematoxylin and eosin staining shows single or small clusters of tumor cells with up to 5 cells per cluster (arrows) detached from the main tumor mass.

not identified in the corresponding primary tumor. In case 11, the primary tumor showed predominant conventional high-grade urothelial carcinoma with a small micropapillary carcinoma component (3%). The corresponding metastatic tumor also revealed small amounts of micropapillary carcinoma component (1%). In case 3, both primary and metastatic tumors were AFP-producing urothelial carcinomas (Fig. 3). There were no remarkable differences in the histomorphologic findings between primary and corresponding metastatic tumors in seven cases (cases 2, 5, 7, 8, 9, 12, and 13) that were primarily diagnosed as conventional high-grade urothelial carcinomas.

DISCUSSION

Regional lymph node metastasis occurs in approximately 30% of bladder cancers with muscle invasion (pT2) and 60% of bladder cancers with extravesical fat extension (pT3–pT4) [25]. The survival outcome of muscle-invasive bladder cancer (pT2–pT4) with regional lymph node metastasis is poor with an 11% 5-year survival rate [26]. Distant metastasis of bladder cancer develops in 10%–29% of patients [19]. Once distant metastasis occurs, survival outcome is very poor with a median survival time of 8.5 months [27].

A previous autopsy study of 367 patients with muscle-invasive bladder cancer demonstrated that the frequency of metastases was strongly associated with local tumor extension and regional lymph node metastases. There was no difference in the frequency of metastases between 308 transitional cell carcinomas and 38 squamous cell carcinomas [28].

In addition, a recent study on the metastatic patterns of bladder cancer showed that advanced T category or atypical histologic features were linked to an early occurrence of distant metastasis

[29]. In this study, we confirmed that histologic variants were not uncommonly detected in urothelial carcinomas with distant metastasis. In addition, these histologic variants were usually present in both primary and accompanying metastatic tumors. Five of the 13 cases included histologic variants, one in pure form and four in mixed forms. The histologic variants of primary tumors were preserved in four corresponding metastatic tumors (4/5, 80%). The following histologic variants of the primary tumors were maintained in the metastatic tumors: micropapillary carcinoma variant (2/4, 50%), squamous differentiation (1/1, 100%), and plasmacytoid variant (1/1, 100%).

Additionally, we present a case of AFP-producing urothelial carcinoma, which has only been described before in several case reports [30,31]. In the previously reported cases, most patients had an increased level of serum AFP, which is closely correlated with tumor burden and may serve as a tumor marker. All tumors also showed aberrant AFP expression by IHC [30,31]. El-Bahrawy et al. [31] emphasized that although AFP-producing urothelial tumors are extremely rare, it is important to be aware of this tumor type because it requires a different chemotherapeutic regimen and has a different prognosis than do AFP-producing germ cell tumors.

Previous studies reported that histologic variants are associated with an advanced disease stage [32]. Recognition of histologic variants is important because they commonly persist in metastatic tumors and represent the association between primary and corresponding metastatic tumors [6,33]. However, to the best of our knowledge, no prior studies have evaluated the frequency of histologic variants in metastatic urothelial carcinomas compared to that of primary urothelial carcinomas of the urinary bladder. In this study, we confirmed that the histologic variants of urothelial carcinoma, even if focally present, frequently metas-

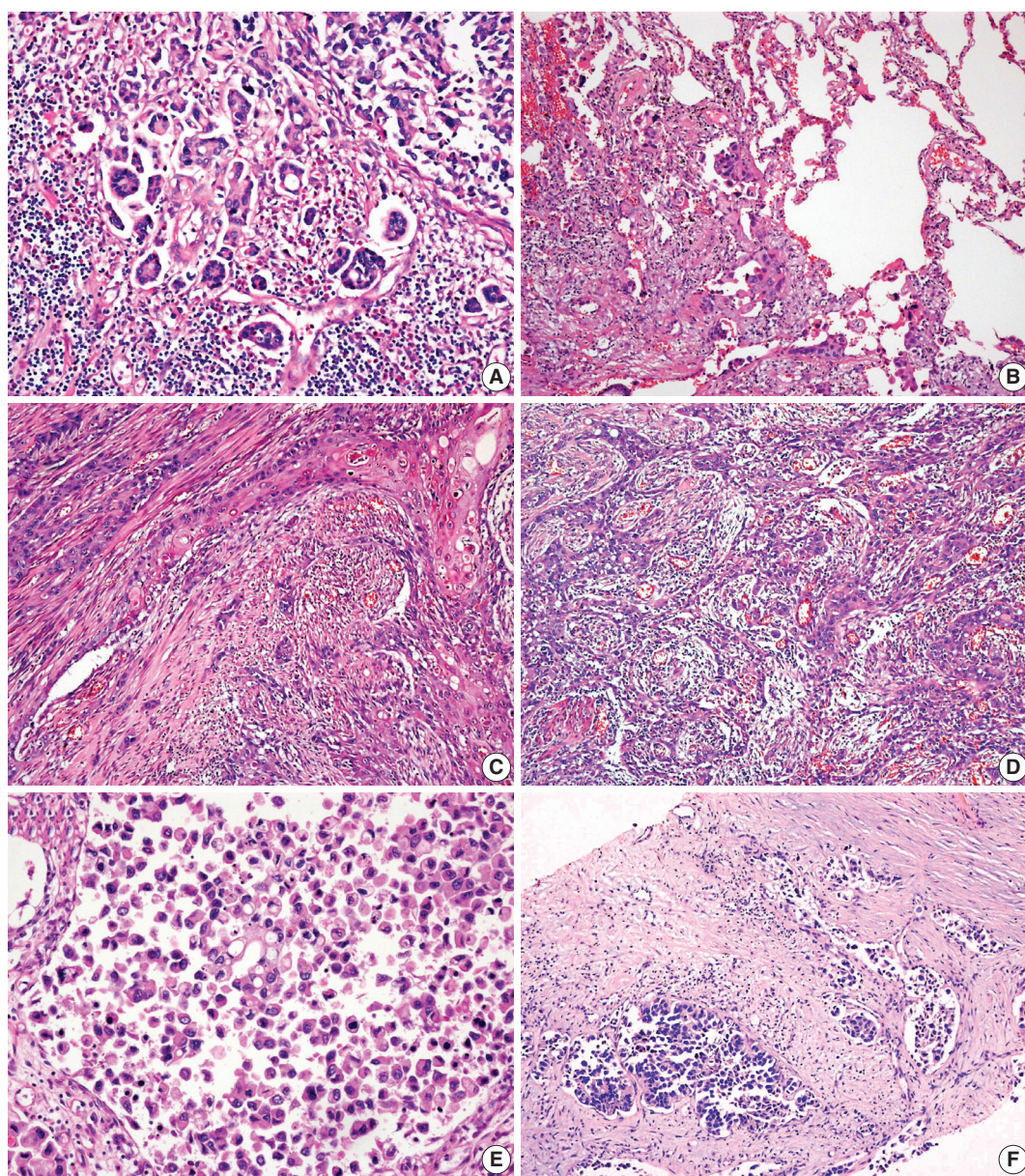


Fig. 2. Histologic features of three histologic variants that are concurrently displayed in both primary and metastatic lesions. (A) In case 1, the primary bladder tumor focally shows a micropapillary carcinoma component characterized by small tight nests or balls with reverse polarity within lacunae. (B) A subsequent pulmonary metastatic lesion is entirely comprised of a micropapillary carcinoma component. (C) The primary bladder tumor in case 4 shows marked squamous differentiation. (D) Squamous differentiation seen in the primary tumor of case 4 is preserved in the subsequent colonic metastatic lesion. (E) In the primary bladder tumor of case 6, the tumor cells are entirely composed of highly atypical discohesive plasmacytoid cells arranged in a solid sheet-like architecture. These histologic findings are compatible with plasmacytoid urothelial carcinoma. (F) Plasmacytoid morphology was maintained in the metastatic tumor cells in the axillary lymph node.

tasize to distant organs. Therefore, histologic examination of urothelial carcinomas in the urinary bladder should be performed with an emphasis on the presence or absence of histologic variants.

In this study, high-grade tumor budding was detected in almost half of all cases, including five muscle-invasive and one non-muscle-invasive urothelial carcinomas. Lymphovascular invasion was

present in all five muscle-invasive urothelial carcinoma cases with high-grade tumor budding. Tumor budding is a histologic phenomenon encountered at the invasive edge of various carcinomas. It represents the epithelial-mesenchymal transition by which tumor cells obtain the ability to disseminate and metastasize [15,18]. Tumor budding is associated with aggressive bi-

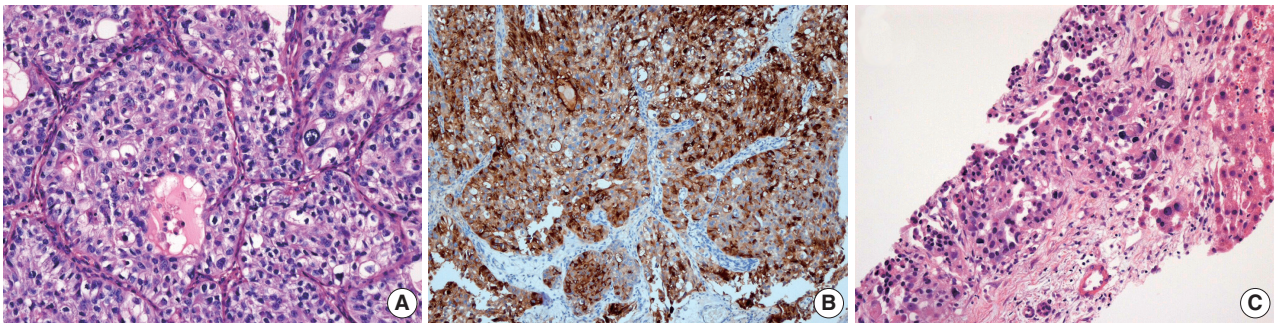


Fig. 3. Histologic and immunohistochemical findings of case 3. (A) In the primary tumor, polygonal tumor cells are arranged in large nests and have highly pleomorphic nuclei and abundant clear to eosinophilic cytoplasm. (B) On immunohistochemistry, most tumor cells show strong positivity for α -fetoprotein (AFP), implicating tumor-derived AFP production. (C) Representative histologic features of hepatic metastatic lesion.

ologic characteristics in various types of carcinomas, including frequent lymphovascular invasion, advanced stage, and distant metastasis [15,18]. In colorectal cancer, high tumor budding has been identified as a predictive biomarker for distant metastasis at the locally advanced stage [18,34]. In this study, six cases (5 which were muscle-invasive bladder cancer) showed lymphovascular invasion that was associated with high-grade tumor budding. A few studies have investigated the clinicopathologic significance of tumor budding in bladder cancer [12,13]. In two previous reports, high tumor budding was suggested to be an adverse pathologic indicator to predict stage progression in both non-muscle-invasive and muscle-invasive bladder cancers [12,13]. Further, larger studies are needed to clarify the association between tumor budding and distant metastasis of bladder cancer.

Distant metastasis of non-muscle-invasive urothelial carcinoma is extremely rare. In a review of over 1,000 patients with bladder cancer (irrespective of stage), Matthews et al. [35] described distant metastases in only nine superficial urothelial carcinomas, including three diagnosed as stage pT_a. In the current study, we describe distant metastasis in three cases of non-muscle-invasive urothelial carcinoma, which were of the pT₁ stage at the time of radical cystectomy. None of these cases showed lymph node metastasis or local recurrence during follow-up. All three of these cases were conventional urothelial carcinomas, and two cases exhibited concomitant carcinoma in situ. Two of the three cases presented with multifocal stromal invasion. Lymphovascular invasion was detected in one case, and high-grade tumor budding was identified in another case. These findings suggest that carcinoma in situ, multifocal stromal invasion, lymphovascular invasion, or high-grade tumor budding may be important histopathologic factors that affect distant metastasis, even in early stage bladder cancer.

There are several limitations in this study. First, the number

of cases was small. Only 13 cases of metastatic urothelial carcinoma were included. The small sample size made it difficult to conduct appropriate statistical tests, which allow for adequate statistical power. In addition, we could not assess the effect of the presence or absence of histologic variants and tumor budding on distant metastasis because the current study only included patients who developed distant metastasis. Second, our study yielded limited results on the impact of tumor budding on distant metastasis in urothelial carcinoma, because this study consisted of a small number of metastatic urothelial carcinoma cases and did not investigate tumor budding in patients without distant metastasis. In contrast, few studies have evaluated the prognostic value of tumor budding in urothelial carcinomas [12,13]. In addition, there are no well-defined criteria to evaluate tumor buddings in urothelial carcinomas. Therefore, we assessed tumor budding according to the International Tumor Budding Consensus Conference criteria [24], which is a standardized scoring system for tumor budding in colorectal cancers. To the best of our knowledge, this is the first study to investigate the presence of tumor budding in metastatic urothelial carcinomas. Further studies with larger sample sizes are warranted to identify the impact of tumor budding on the occurrence of distant metastasis.

In conclusion, histologic variants are not uncommonly detected in distant metastatic urothelial carcinomas. Despite its rarity, the histologic variants present in primary tumors are mostly maintained in metastatic tumors. High-grade tumor budding, which is frequently found in primary tumors, seems to play a significant role in the development of distant metastasis. Therefore, it may be useful to evaluate the presence of histologic variants and tumor budding in urothelial carcinomas of the urinary bladder to predict distant metastasis, even in non-muscle invasive urothelial carcinomas.

Ethics Statement

All procedures performed in this study were approved by the Institutional Review Board at Ewha Womans University Mokdong Hospital (IRB No. 2019-07-013) in accordance with the Helsinki Declaration as revised in 2013. Formal written informed consent was waived by the IRB.

ORCID

Youngeun Yoo <https://orcid.org/0000-0003-4855-3870>
 Junghye Lee <https://orcid.org/0000-0001-8454-4360>
 Heae Surng Park <https://orcid.org/0000-0003-1849-5120>
 Min-Sun Cho <https://orcid.org/0000-0001-8772-9686>
 Sun Hee Sung <https://orcid.org/0000-0001-9345-1131>
 Sanghui Park <https://orcid.org/0000-0003-3837-8677>
 Euno Choi <https://orcid.org/0000-0002-9284-9276>

Author Contributions

Conceptualization: YY, JL, HSP, MSC, SHS, SP, EC. Data Curation: YY, JL. Formal analysis: YY, JL, EC. Investigation: YY, EC. Methodology: SP, EC. Project administration: SP, EC. Resources: HSP, MSC, SHS. Supervision: SP, EC. Validation: EC. Visualization: YY, EC. Writing—original draft: EC. Writing—review & editing: YY, JL, HSP, MSC, SHS, SP, EC. Approval of final manuscript: all authors.

Conflicts of Interest

The authors declare that they have no potential conflicts of interest.

Funding Statement

No funding to declare

References

1. Bray F, Ferlay J, Soerjomataram I, Siegel RL, Torre LA, Jemal A. Global cancer statistics 2018: GLOBOCAN estimates of incidence and mortality worldwide for 36 cancers in 185 countries. *CA Cancer J Clin* 2018; 68: 394-424.
2. Lopez-Beltran A, Henriques V, Montironi R, Cimadamore A, Raspollini MR, Cheng L. Variants and new entities of bladder cancer. *Histopathology* 2019; 74: 77-96.
3. Warrick JL. Clinical significance of histologic variants of bladder cancer. *J Natl Compr Canc Netw* 2017; 15: 1268-74.
4. Moch H, Humphrey PA, Ulbright TM, Reuter VE. WHO classification of tumours of the urinary system and male genital organs. 4th ed. Lyon: International Agency for Research on Cancer, 2016; 77-98.
5. Moschini M, D'Andrea D, Korn S, et al. Characteristics and clinical significance of histological variants of bladder cancer. *Nat Rev Urol* 2017; 14: 651-68.
6. Amin MB. Histological variants of urothelial carcinoma: diagnostic, therapeutic and prognostic implications. *Mod Pathol* 2009; 22 Suppl 2: S96-118.
7. Liu Y, Bui MM, Xu B. Urothelial carcinoma with squamous differentiation is associated with high tumor stage and pelvic lymph-node metastasis. *Cancer Control* 2017; 24: 78-82.
8. Perepletchikov AM, Parwani AV. Micropapillary urothelial carcinoma: clinico-pathologic review. *Pathol Res Pract* 2009; 205: 807-10.
9. Keck B, Wach S, Stoehr R, et al. Plasmacytoid variant of bladder cancer defines patients with poor prognosis if treated with cystectomy and adjuvant cisplatin-based chemotherapy. *BMC Cancer* 2013; 13: 71.
10. Sanfrancesco J, McKenney JK, Leivo MZ, Gupta S, Elson P, Hansel DE. Sarcomatoid urothelial carcinoma of the bladder: analysis of 28 cases with emphasis on clinicopathologic features and markers of epithelial-to-mesenchymal transition. *Arch Pathol Lab Med* 2016; 140: 543-51.
11. Venyo AK. Nested variant of urothelial carcinoma. *Adv Urol* 2014; 2014: 192720.
12. Lorenzo Soriano L, Ordaz Jurado G, Pontones Moreno JL, et al. Tumor budding: prognostic value in muscle-invasive bladder cancer. *Urology* 2019; 130: 93-8.
13. Fukumoto K, Kikuchi E, Mikami S, et al. Tumor budding, a novel prognostic indicator for predicting stage progression in T1 bladder cancers. *Cancer Sci* 2016; 107: 1338-44.
14. Ueno H, Murphy J, Jass JR, Mochizuki H, Talbot IC. Tumour 'budding' as an index to estimate the potential of aggressiveness in rectal cancer. *Histopathology* 2002; 40: 127-32.
15. Lugli A, Karamitopoulou E, Zlobec I. Tumour budding: a promising parameter in colorectal cancer. *Br J Cancer* 2012; 106: 1713-7.
16. Salhia B, Trippel M, Pfaltz K, et al. High tumor budding stratifies breast cancer with metastatic properties. *Breast Cancer Res Treat* 2015; 150: 363-71.
17. Kemi N, Eskuri M, Ikalainen J, Karttunen TJ, Kauppila JH. Tumor budding and prognosis in gastric adenocarcinoma. *Am J Surg Pathol* 2019; 43: 229-34.
18. Grigore AD, Jolly MK, Jia D, Farach-Carson MC, Levine H. Tumor budding: the name is EMT. *Partial EMT. J Clin Med* 2016; 5: 51.
19. Manig L, Kasmann L, Janssen S, Rades D. Predicting survival after irradiation of metastases from transitional carcinoma of the bladder. *Anticancer Res* 2016; 36: 6663-5.
20. Shelley MD, Cleves A, Wilt TJ, Mason MD. Gemcitabine chemotherapy for the treatment of metastatic bladder carcinoma. *BJU Int* 2011; 108: 168-79.
21. Sood S, Paner GP. Plasmacytoid urothelial carcinoma: an unusual variant that warrants aggressive management and critical distinction on transurethral resections. *Arch Pathol Lab Med* 2019; 143: 1562-7.
22. Ricardo-Gonzalez RR, Nguyen M, Gokden N, Sangoi AR, Presti JC Jr, McKenney JK. Plasmacytoid carcinoma of the bladder: a urothelial carcinoma variant with a predilection for intraperitoneal spread. *J Urol* 2012; 187: 852-5.
23. Bochner BH, Hansel DE, Efstathiou JA, et al. Urinary bladder. In: Amin MB, ed. *AJCC cancer staging manual*. 8th ed. New York: Springer, 2017; 346-55.
24. Lugli A, Kirsch R, Ajioka Y, et al. Recommendations for reporting tumor budding in colorectal cancer based on the International Tumor Budding Consensus Conference (ITBCC) 2016. *Mod Pathol* 2017; 30: 1299-311.
25. Shankar PR, Barkmeier D, Hadjiiski L, Cohan RH. A pictorial review of bladder cancer nodal metastases. *Transl Androl Urol* 2018; 7: 804-13.
26. MacVicar AD. Bladder cancer staging. *BJU Int* 2000; 86 Suppl 1: 111-22.
27. Jessen C, Agerbaek M, Von Der Maase H. Predictive factors for response and prognostic factors for long-term survival in consecutive, single institution patients with locally advanced and/or metastatic transitional cell carcinoma following cisplatin-based chemotherapy. *Acta Oncol* 2009; 48: 411-7.
28. Wallmeroth A, Wagner U, Moch H, Gasser TC, Sauter G, Mihatsch

- MJ. Patterns of metastasis in muscle-invasive bladder cancer (pT2-4): an autopsy study on 367 patients. *Urol Int* 1999; 62: 69-75.
29. Shinagare AB, Ramaiya NH, Jagannathan JP, Fennessy FM, Taplin ME, Van den Abbeele AD. Metastatic pattern of bladder cancer: correlation with the characteristics of the primary tumor. *AJR Am J Roentgenol* 2011; 196: 117-22.
 30. Melms JC, Thummalapalli R, Shaw K, et al. Alpha-fetoprotein (AFP) as tumor marker in a patient with urothelial cancer with exceptional response to anti-PD-1 therapy and an escape lesion mimic. *J Immunother Cancer* 2018; 6: 89.
 31. El-Bahrawy M. Alpha-fetoprotein-producing non-germ cell tumors of the urological system. *Rev Urol* 2011; 13: 14-9.
 32. Klaile Y, Schlack K, Boegemann M, Steinestel J, Schrader AJ, Krabbe LM. Variant histology in bladder cancer: how it should change the management in non-muscle invasive and muscle invasive disease? *Transl Androl Urol* 2016; 5: 692-701.
 33. Nigwekar P, Amin MB. The many faces of urothelial carcinoma: an update with an emphasis on recently described variants. *Adv Anat Pathol* 2008; 15: 218-33.
 34. Jayasinghe C, Simiantonaki N, Kirkpatrick CJ. Histopathological features predict metastatic potential in locally advanced colon carcinomas. *BMC Cancer* 2015; 15: 14.
 35. Matthews PN, Madden M, Bidgood KA, Fisher C. The clinicopathological features of metastatic superficial papillary bladder cancer. *J Urol* 1984; 132: 904-6.

The prognostic significance of p16 expression pattern in diffuse gliomas

Jin Woo Park¹, Jeongwan Kang¹, Ka Young Lim¹, Hyunhee Kim¹, Seong-Ik Kim¹,
Jae Kyung Won¹, Chul-Kee Park², Sung-Hye Park^{1,3}

Departments of ¹Pathology and ²Neurosurgery, Seoul National University Hospital, Seoul;
³Neuroscience Research Institute, Seoul National University College of Medicine, Seoul, Korea

Background: *CDKN2A* is a tumor suppressor gene that encodes the cell cycle inhibitor protein p16. Homozygous deletion of the *CDKN2A* gene has been associated with shortened survival in isocitrate dehydrogenase (*IDH*)–mutant gliomas. This study aimed to analyze the prognostic value of p16 and to evaluate whether p16 immunohistochemical staining could be used as a prognostic marker to replace *CDKN2A* genotyping in diffuse gliomas. **Methods:** p16 immunohistochemistry was performed on tissue microarrays of 326 diffuse gliomas with diagnoses that reflected *IDH*-mutations and 1p/19q codeletion status. The results were divided into three groups (negative, focal expression, overexpression) according to the presence and degree of p16 expression. Survival analysis was performed to assess the prognostic value of p16 expression. **Results:** A loss of p16 expression predicted a significantly worse outcome in all glioma patients (n=326, p<.001), in the *IDH*-mutant glioma patients (n=103, p=.010), and in the *IDH*-mutant astrocytoma patients (n=73, p=.032). However, loss of p16 expression did not predict the outcome in the *IDH*-wildtype glioma patients (n=223, p=.121) or in the oligodendroglial tumor patients with the *IDH*-mutation and 1p/19q codeletion (n=30, p=.457). Multivariate analysis showed the association was still significant in the *IDH*-mutant glioma patients (p=.008; hazard ratio [HR], 2.637; 95% confidence interval [CI], 1.295 to 5.372) and in the *IDH*-mutant astrocytoma patients (p=.001; HR, 3.586; 95% CI, 1.649 to 7.801). Interestingly, patients who presented with tumors with p16 overexpression also had shorter survival times than did patients with tumors with p16 focal expression in the whole glioma (p<.001) and in *IDH*-mutant glioma groups. (p=.046). **Conclusions:** This study suggests that detection of p16 expression by immunohistochemistry can be used as a useful surrogate test to predict prognosis, especially in *IDH*-mutant astrocytoma patients.

Key Words: Glioma; p16; Immunohistochemistry; Prognosis; *CDKN2A*

Received: October 8, 2020 **Revised:** October 20, 2020 **Accepted:** October 22, 2020

Corresponding Author: Sung-Hye Park, MD, PhD, Department of Pathology, Seoul National University College of Medicine, 103 Daehak-ro, Jongno-gu, Seoul 03080, Korea
Tel: +82-2-740-3090, Fax: +82-2-743-5530, E-mail: shparknp@snu.ac.kr

CDKN2A is a tumor suppressor gene located on chromosome 9p21 that encodes the cell cycle inhibitor protein p16 [1]. Genetic alterations of this gene are frequently observed in various types of human cancers [1-3]. With regard to brain tumors and prognosis, homozygous deletion of the *CDKN2A* gene has been reported to be associated with shortened survival in isocitrate dehydrogenase (*IDH*)–mutant glioma patients [4-8]. In the recent expert meeting of cIMPACT-NOW (the Consortium to Inform Molecular and Practical Approaches to CNS Tumor Taxonomy-Not Official WHO), update 5, genetic testing for the detection of *CDKN2A* homozygous deletion has been recommended for grade *IDH*-mutant astrocytic tumors. Its importance is increasingly high in adult and pediatric glioma patients [4,6,9-11].

Molecular testing to identify the *CDKN2A* deletion requires advanced, high-cost equipment. However, the results of molecular testing are difficult to interpret. Therefore, it is challenging to use molecular testing in routine diagnostic practice. Since the *CDKN2A* gene product is the p16 protein, immunohistochemical detection of p16 protein expression can be used instead of molecular testing to identify the *CDKN2A* gene deletion. Before 2010, in the pre-*IDH*-era, a few studies investigated the predictive value of p16 immunoreactivity in glioma samples [12-17]. The studies mainly targeted heterogeneous groups of gliomas that did not reflect the current molecular genetics integrated classification. The sample size was small, and the results were not consistently conclusive. In addition, no large-scale comprehensive studies have been conducted on the prognostic significance of

p16 immunohistochemistry in gliomas, particularly in this *IDH*-era of brain tumor diagnoses.

Meanwhile, although p16 is a tumor suppressor, aberrant overexpression of p16 protein has been observed in several tumors, including uterine cervical cancer, breast cancer, colorectal adenocarcinoma, and malignant melanoma [18-20]. In these tumors, p16 overexpression occurs by various mechanisms and has diverse prognostic implications depending on the tumor type [21]. Therefore, in addition to examining the prognostic relevance of p16 protein loss, it is also worth evaluating the prognostic implications of p16 overexpression in glioma patients.

This study aimed to determine whether p16 immunohistochemical staining can be used as a prognostic marker to replace *CDKN2A* genotyping in molecularly characterized diffuse gliomas. We first examined the correlation and concordance between p16 immunohistochemistry and *CDKN2A* fluorescent in situ hybridization (FISH) results. In addition, considering that p16 is a negative regulator of cell proliferation, we evaluated whether the loss of p16 expression was related to an increase in the cell proliferation marker Ki-67 labeling index. Finally, the survival analyses were performed to evaluate the prognostic implications of p16 protein expression patterns in the whole sample, and in the subgroups according to *IDH*-mutation and 1p/19q codeletion status.

MATERIALS AND METHODS

Subjects and data acquisition

A total of 326 cases of diffuse glioma from Seoul National University Hospital (SNUH) between 2011 and 2015 with tissue microarray (TMA) blocks were included in this study. The clinical information and test results that were previously conducted to assist in diagnosis were obtained retrospectively from the electronic medical records of SNUH. The overall survival time was calculated from the date of surgery to the date of death. All diagnoses were reassessed to reflect genetic alterations, including *IDH*-mutation and 1p/19q codeletion status according to the cIMPACT-NOW update 5 and 6, and the 2016 World Health Organization (WHO) classification of central nervous system tumors.

Evaluation of p16 immunohistochemistry

The immunohistochemical staining for p16 was conducted on the TMA sections using an antibody against p16 (mouse monoclonal, clone E6H4, Ventana, Tucson, AZ, USA) and the Ventana BenchMark XT automated immunohistochemical staining sys-

tem following the manufacturer's protocol. The results of immunohistochemical staining were first scored as the percentage of positively stained cells. Tumor cells with only nuclear or concurrent nuclear and cytoplasmic immunoreactivity were considered positive. The scoring was performed blindly without any knowledge of the diagnostic or clinical information. If there were no positive cells, or if the percentage of positive cells was < 1%, then the tumor was classified as p16 negative (loss of expression). Conversely, tumors with more than 1% immunopositivity were considered to be p16 positive (retained expression). The p16 immunopositive cases were further divided into focal expression (if the positive cells were < 50%) or diffuse overexpression (if the positive cells were > 50%) according to the degree of p16 expression. Notably, in the group with p16 overexpression, most of the tumor cells showed simultaneous intense nuclear and cytoplasmic staining (Fig. 1).

Other immunohistochemical and molecular testing variables

The previously used antibodies included IDH1 (1:100, mouse monoclonal, clone H09, Dianova, Hamburg, Germany), p53 (1:1,000, mouse monoclonal, clone DO-7, DAKO, Glostrup, Denmark), PTEN (1:400, mouse monoclonal, clone 6H2.1, DAKO) and Ki-67 (1:100, mouse monoclonal, clone MIB-1, DAKO). Quantification of the Ki-67 labeling index was determined by the Nuclear v9 algorithm using the Aperio ImageScope software (Aperio Technologies, Vista, CA, USA). p53 was considered to be overexpressed if $\geq 30\%$ of the tumor nuclei showed robust immunopositivity [22]. For IDH1 and PTEN, the immunohistochemical results were evaluated as positive or negative. Positive IDH1 immunostaining indicated the presence of a mutation, while negative immunostaining of PTEN meant protein loss.

Molecular tests that were previously performed for diagnosis included 1p/19q FISH to detect chromosome 1p and 19q codeletion; *IDH1/IDH2* direct sequencing (performed only when the IDH1 immunohistochemistry result was negative); *CDKN2A* (9p21) FISH to catch gene deletion; epidermal growth factor receptor (*EGFR*) (7p12) FISH to detect gene amplification; *PTEN* (10q23) FISH to detect gene deletion; and *O*⁶-methylguanine-DNA methyltransferase (MGMT) methylation-specific polymerase chain reaction analysis. The probes used to perform FISH were as follows: Vysis LSI 1p36 SpectrumOrange/1q25 SpectrumGreen Probes and Vysis LSI 19q13 SpectrumOrange/19p13 SpectrumGreen Probes (Abbott Molecular, Vysis, Des Plaines, IL, USA); Vysis LSI *CDKN2A* SpectrumOrange/CEP

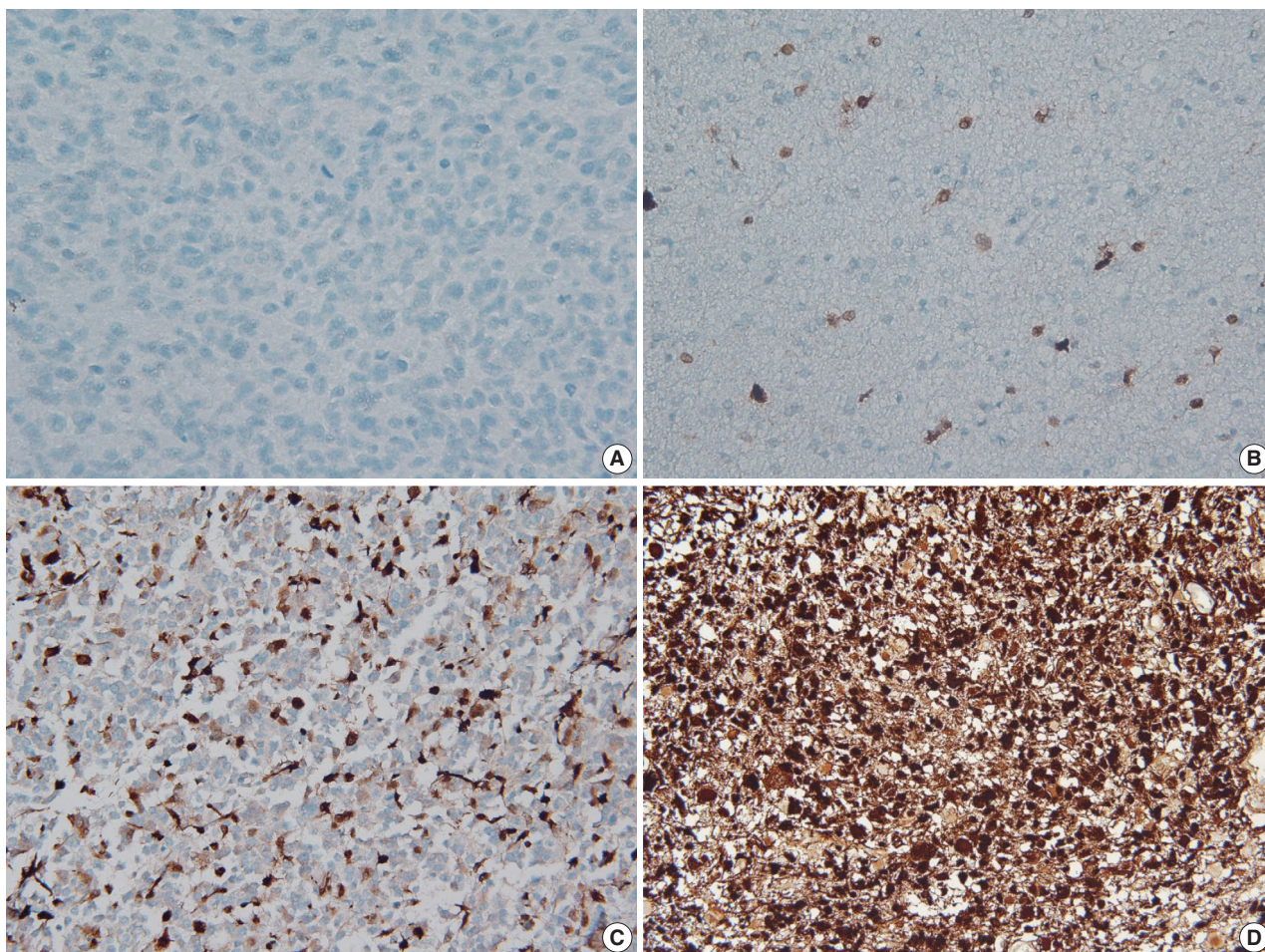


Fig. 1. Representative images of p16 immunohistochemical staining. If immunopositive cells were absent or made up < 1% of cells, the tumor was classified as having a loss of expression (A). Conversely, tumors with > 1% of immunopositivity were considered to have retained expression, which was further subdivided into focal expression (B, C) or overexpression (D) according to the degree of p16 expression on a 50% basis. B and C show the range of focal expression.

9 SpectrumGreen Probes (Abbott Molecular); Vysis LSI EGFR SpectrumOrange/CEP 7 SpectrumGreen Probes (Abbott Molecular); Vysis LSI PTEN/CEP 10 Dual Color Probe (Abbott Molecular). Each molecular test was performed and interpreted as previously described [23,24]. Homozygous deletion of the *CDKN2A* gene was determined when > 15% of tumor cells lost two test signals in the presence of at least one reference signal in 100 non-overlapping counted nuclei [25]. *PTEN* is a representative quasi-sufficient and obligate haploinsufficient tumor suppressor gene [26]. A *PTEN* hemizygous deletion was considered if > 50% of tumor cells showed more than one test signal loss or if > 10% of tumor cells showed two test signal losses in 100 non-overlapping nuclei with two reference signals [27]. A *PTEN* homozygous deletion was defined by the loss of both *PTEN* signals in more than 30% of tumor cells when counting more than 100 non-overlapping nuclei with at least one reference signal [27]. With regard

to the *PTEN* evaluation, most cases were evaluated by only one of the *PTEN* FISH or *PTEN* immunohistochemistry. The final results related to *PTEN* loss were used in combination with the two tests.

Statistical analyses

The chi-square test was used to examine the association between categorical variables. Cohen's kappa coefficient (κ) was calculated to determine whether there was a concordance between p16 immunohistochemistry and *CDKN2A* FISH. The Mann-Whitney U-test was used to test the relationship between p16 immunoreactivity and the Ki-67 labeling index. Kaplan-Meier survival curves were generated to estimate the overall survival distributions. The log-rank test was used for univariate survival comparisons. The Cox proportional hazards regression model was applied for the multivariate analyses using forward stepwise variable se-

lection. Variables with prognostic significance in univariate analyses were selected as independent variables in the multivariate analysis model. Statistical significance was defined as a p-value of $< .05$. All statistical analyses were performed using IBM SPSS Statistics software ver. 26.0 (IBM Corp., Armonk, NY, USA).

RESULTS

Characteristics of the study population

The median age of the study population was 54 years (range, 16 to 82 years), and 185 patients (56.7%) were men. Sixty-five cases (19.9%) were of recurrent tumors. Most patients were treated with surgery, followed by adjuvant radiotherapy and/or chemotherapy. Detailed clinical information is shown in Table 1. For the survival data, the median follow-up time was 23 months (range, 0 to 103 months). During this follow-up period, 220 patients (67.5%) died, while 106 patients (32.5%) were still alive at the last contact. The diagnoses according to cIMPACT-NOW update 5 and 6 and 2016 WHO classification were as follows: astrocytoma, *IDH*-mutant, WHO grade 2 (n = 8, 2.5%); anaplastic astrocytoma, *IDH*-mutant, WHO grade 3 (n = 27, 8.3%); astrocytoma, *IDH*-mutant, WHO grade 4 (n = 38, 11.7%); oligodendroglioma, *IDH*-mutant and 1p/19q-codeleted (ODG), WHO grade 2 (n = 12, 3.7%); ODG, WHO grade 3 (n = 18, 5.5%); diffuse astrocytoma, *IDH*-wildtype (n = 3, 0.9%); anaplastic astrocytoma, *IDH*-wildtype (n = 25, 7.7%); and glioblastoma, *IDH*-wildtype (n = 195, 59.8%). Overall, there were 103 *IDH*-mutant tumors and 223 *IDH*-wildtype tumors. p16 loss was more prevalent in the *IDH*-wildtype tumors than it was in the *IDH*-mutant tumors (*IDH*-wildtype, 120 out of 223 cases [53.8%] vs. *IDH*-mutant, 23 out of 103 cases [22.3%]; $p < .001$). Among the *IDH*-mutant tumors, the frequency of p16 loss was similar between the *IDH*-mutant astrocytomas (23.3%, 17 out of 73 cases) and ODG (20%, 6 out of 30 cases) ($p = .716$). The age of the patients was significantly higher in the p16 loss group than it was in the p16 expression group (p16 loss group, median 56 [range, 16 to 82] vs. p16 expression group, median 50 [range, 17 to 77]; $p < 0.001$). There was no significant association between p16 expression status and other clinical variables such as sex, the extent of surgery (biopsy or resection), recurrence, or adjuvant treatment. The immunohistochemical and FISH results of the study population are presented in Table 2.

Comparison of p16 immunohistochemistry and *CDKN2A* FISH results

The association between the *CDKN2A* homozygous deletion

Table 1. Clinicopathologic information

Characteristic	No. (%) (n=326)
Age (yr)	54 (16–82)
Sex	
Male	185 (56.7)
Female	141 (43.3)
IDH status	
<i>IDH</i> -mutant	103 (31.6)
<i>IDH</i> -wildtype	223 (68.4)
Astrocytoma, <i>IDH</i> -mutant ^a	73 (22.4)
Astrocytoma, <i>IDH</i> -mutant, WHO grade 2	8 (2.5)
Astrocytoma, <i>IDH</i> -mutant, WHO grade 3	27 (8.3)
Astrocytoma, <i>IDH</i> -mutant, WHO grade 4	38 (11.7)
ODG ^a	30 (9.2)
ODG, WHO grade 2	12 (3.7)
ODG, WHO grade 3	18 (5.5)
Glioma, <i>IDH</i> -wildtype ^a	223 (68.4)
Diffuse astrocytoma, <i>IDH</i> -wildtype	3 (0.9)
Anaplastic astrocytoma, <i>IDH</i> -wildtype	25 (7.7)
Glioblastoma, <i>IDH</i> -wildtype	195 (59.8)
Survival outcome	
Death	220 (67.5)
Censored	106 (32.5)
Survival time (mo), median (range)	23 (0–103)
Extent of surgery	
Biopsy	22 (6.7)
Resection	304 (93.3)
Tumor recurrence	
Primary tumor	261 (80.1)
Recurred tumor	65 (19.9)
Adjuvant treatment (n=323)	
Yes	300 (92.9)
No	23 (7.1)

IDG, isocitrate dehydrogenase; WHO, World Health Organization; ODG, oligodendroglioma, *IDH*-mutant and 1p/19q-codeleted.

^aDiagnoses were made by cIMPACT-Now update 5 and 6, and 2016 World Health Organization classification.

and the loss of p16 expression was significant ($p < .001$) (Table 3). Sixty-eight percent (88/129) of tumors with *CDKN2A* homozygous deletions by FISH demonstrated a loss of p16 expression by immunohistochemistry, while 72% (142/197) of tumors without the *CDKN2A* homozygous deletion showed p16 immunopositivity. Therefore, the diagnostic accuracy of p16 immunohistochemistry to detect a *CDKN2A* homozygous deletion confirmed by FISH was 70.6% (250/326). There was fair agreement between the *CDKN2A* FISH and p16 immunohistochemistry results (Cohen's kappa = 0.396, $p < .001$).

Correlation between p16 immunohistochemistry and Ki-67 labeling index

There was a significant inverse correlation between p16 expression and the Ki-67 labeling index ($p < .001$). That is, tumors with

p16 loss had a significantly higher Ki-67 labeling index (mean, 27.60%; median, 22.50%; range, 1.11 to 90.16) than did those with p16 expression (mean, 19.98%; median, 12.90%; range, 0.40 to 74.46). In addition, when the p16 retained expression (no loss) group was divided into two additional groups of overexpression and focal expression, the p16 overexpression group (mean, 27.73%; median, 24.70%; range, 2.34 to 72.70) showed a significantly higher Ki-67 labeling index than did the p16 focal expression group (mean, 16.30%, median, 8.55%; range,

0.40 to 74.46; $p < .001$). There was also a significant difference in the Ki-67 labeling index between the p16 focal expression group and the p16 loss of expression group (mean, 27.60%; median, 22.50%; range, 1.11 to 90.16; $p < .001$). However, there was no significant difference between p16 loss of expression and the p16 overexpression groups ($p = .940$) (Fig. 2).

Table 2. Immunohistochemical and FISH results of the included cases

Parameter	No. (%)
p16 IHC	
Loss	143 (43.9)
No loss (retained)	183 (56.1)
Focal expression	124 (38.0)
Overexpression	59 (18.1)
CDKN2A FISH	
Homozygous deletion	129 (39.6)
No deletion	197 (60.4)
EGFR amplification	
Positive	63 (19.3)
Negative	263 (80.7)
PTEN alteration (n=324)	
Loss	41 (12.6)
No loss	283 (86.8)
p53 overexpression	
Positive	143 (43.9)
Negative	183 (56.1)
MGMTp methylation (n=324)	
Positive	182 (55.8)
Negative	142 (43.6)
Ki-67 labeling index, median (range, %)	19.41 (0.4–90.16)

FISH, fluorescence in situ hybridization; IHC, immunohistochemistry; EGFR, epidermal growth factor receptor; MGMTp, O6-methylguanine-DNA methyltransferase promoter.

Survival analysis

In a total of 326 whole glioma samples, a loss of p16 expression was significantly associated with short overall survival in univariate analysis using Kaplan-Meier curves and the log-rank test ($p < .001$) (Fig. 3A). When stratified by *IDH* status, tumors with p16 loss demonstrated a significantly worse outcome in *IDH*-mutant glioma patients ($p = .010$) (Fig. 3B) than did those without p16 loss. However, no such association was found in the *IDH*-wildtype gliomas ($p = .121$) (Fig. 3C). Other parameters whose prognostic significance was confirmed by the log-rank test included recurrent tumors ($p < .001$), *EGFR* amplification ($p = .004$) and p53 overexpression ($p = .002$) in *IDH*-mutant glioma patients. In contrast, the extent of surgery ($p = .043$), adjuvant treatment ($p = .005$) and *MGMT* promoter methylation ($p = .024$) were included in the *IDH*-wildtype gliomas. Sex and *PTEN* loss had no significant prognostic association with either group.

Table 3. Comparison between CDKN2A FISH and p16 immunohistochemistry

p16 IHC	CDKN2A FISH		Total	p-value ^a
	Deletion	No deletion		
Loss	88 (68.2)	55 (27.9)	143	< .001
No loss	41 (31.8)	142 (72.1)	183	
Total	129 (100)	197 (100)	326	

Values are presented as number (%).

FISH, fluorescence in situ hybridization; IHC, immunohistochemistry.

^ap-value was determined using chi-square test.

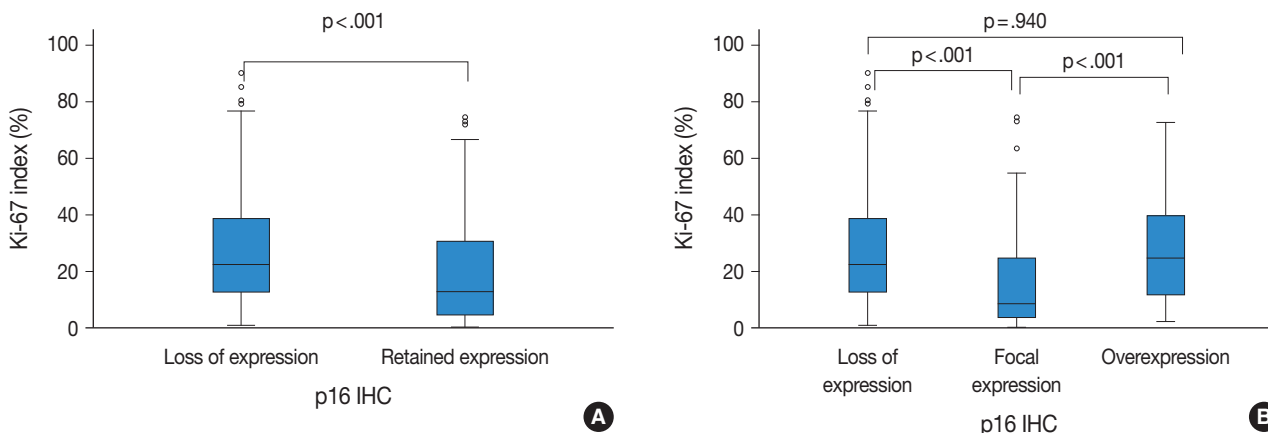


Fig. 2. Ki-67 labeling index according to p16 expression status (A) and the degree of p16 expression (B). IHC, immunohistochemistry.

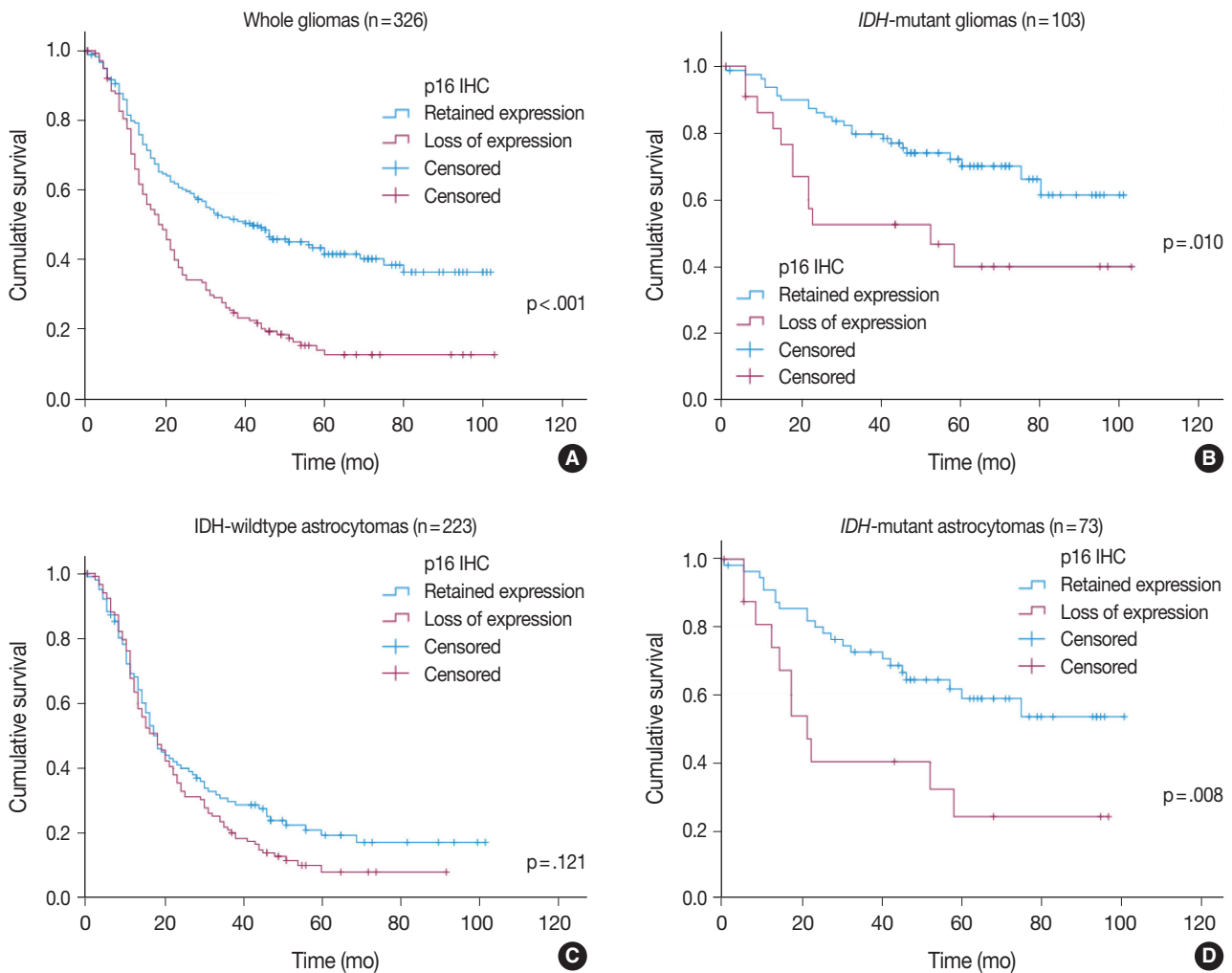


Fig. 3. Kaplan-Meier curves for overall survival according to p16 expression status: (A) whole gliomas, (B) *IDH*-mutant gliomas including oligodendrogliomas, (C) *IDH*-wildtype astrocytomas, and (D) *IDH*-mutant astrocytomas. *IDH*, isocitrate dehydrogenase; *IHC*, immunohistochemistry.

Table 4. Multivariate Cox regression analysis

Variable	<i>IDH</i> -mutant gliomas (n = 103)			<i>IDH</i> -mutant astrocytomas (n = 73)		
	HR	95% CI	p-value	HR	95% CI	p-value
p16 loss (<i>IHC</i>)	2.637	1.295–5.372	.008	3.586	1.649–7.801	.001
Recurred tumor	3.404	1.721–6.732	<.001	4.398	2.111–9.165	<.001
p53 overexpression	2.725	1.371–5.417	.004	NA	NA	.479

IDH, isocitrate dehydrogenase; *IHC*, immunohistochemistry; *HR*, hazards ratio; *CI*, confidence interval; *NA*, not applicable.

Multivariate Cox proportional hazards regression analysis was performed on the *IDH*-mutant gliomas using variables selected in univariate analyses as covariates. Although *CDKN2A* FISH and Ki-67 were significantly prognostic for *IDH*-mutant gliomas in univariate analysis ($p = .001$, the log-rank test for *CDKN2A* FISH; $p < .001$, and univariate Cox regression analysis for Ki-67), they were not included in the final multivariate model because they were collinear with p16 immunohistochemistry. After ad-

justing for recurrence, *EGFR* amplification and p53 overexpression, p16 loss was still a significant prognostic factor for worse outcome ($p = .008$; hazards ratio [*HR*], 2.637; 95% confidence interval [*CI*], 1.295 to 5.372) (Table 4). Next, when the *IDH*-mutant group was subdivided according to 1p/19q codeletion status, loss of p16 expression was associated with significantly shorter overall survival in astrocytoma, *IDH*-mutant patients by the log-rank test ($p = .008$) (Fig. 3D), but not in ODG patients

($p = .457$). This association with the *IDH*-mutant astrocytomas was also significant in a multivariate analysis adjusted for recurrence, *EGFR* amplification, and *p53* overexpression ($p = .001$; HR, 3.586; 95% CI, 1.649 to 7.801) (Table 4).

We also divided the p16 retained expression (no loss) tumors into two additional categories (focal expression vs. overexpression) according to the degree of p16 expression to check whether p16 overexpression has a prognostic meaning. Interestingly, among the 326 whole glioma cases, the p16 overexpression group showed a significantly worse overall survival curve than did the p16 focal expression group in Kaplan-Meier analysis ($p < .001$) (Fig. 4A). When limited to the *IDH*-mutant tumors (including astrocytomas and ODG), the p16 overexpression group had worse overall survival than did the p16 focal expression group ($p = .046$) (Fig. 4B). This association was not seen in the *IDH*-wildtype

glioma patients (Fig. 4C). In multivariate analysis (adjusted for recurrence, *p53* overexpression, and *EGFR* amplification), p16 overexpression was still associated with shorter overall survival than p16 focal expression, but this was not statistically significant ($p = .171$; HR, 2.048; 95% CI, 0.734 to 5.711). In the subgroup of *IDH*-mutant astrocytoma patients, p16 overexpression also appeared to be related to shorter overall survival compared to p16 focal expression; however, the difference did not reach statistical significance in Kaplan-Meier analysis ($p = .251$) (Fig. 4D). Meanwhile, in the ODG, the analysis was not possible because none of the 30 cases showed p16 overexpression.

DISCUSSION

This study demonstrates the prognostic value of p16 immu-

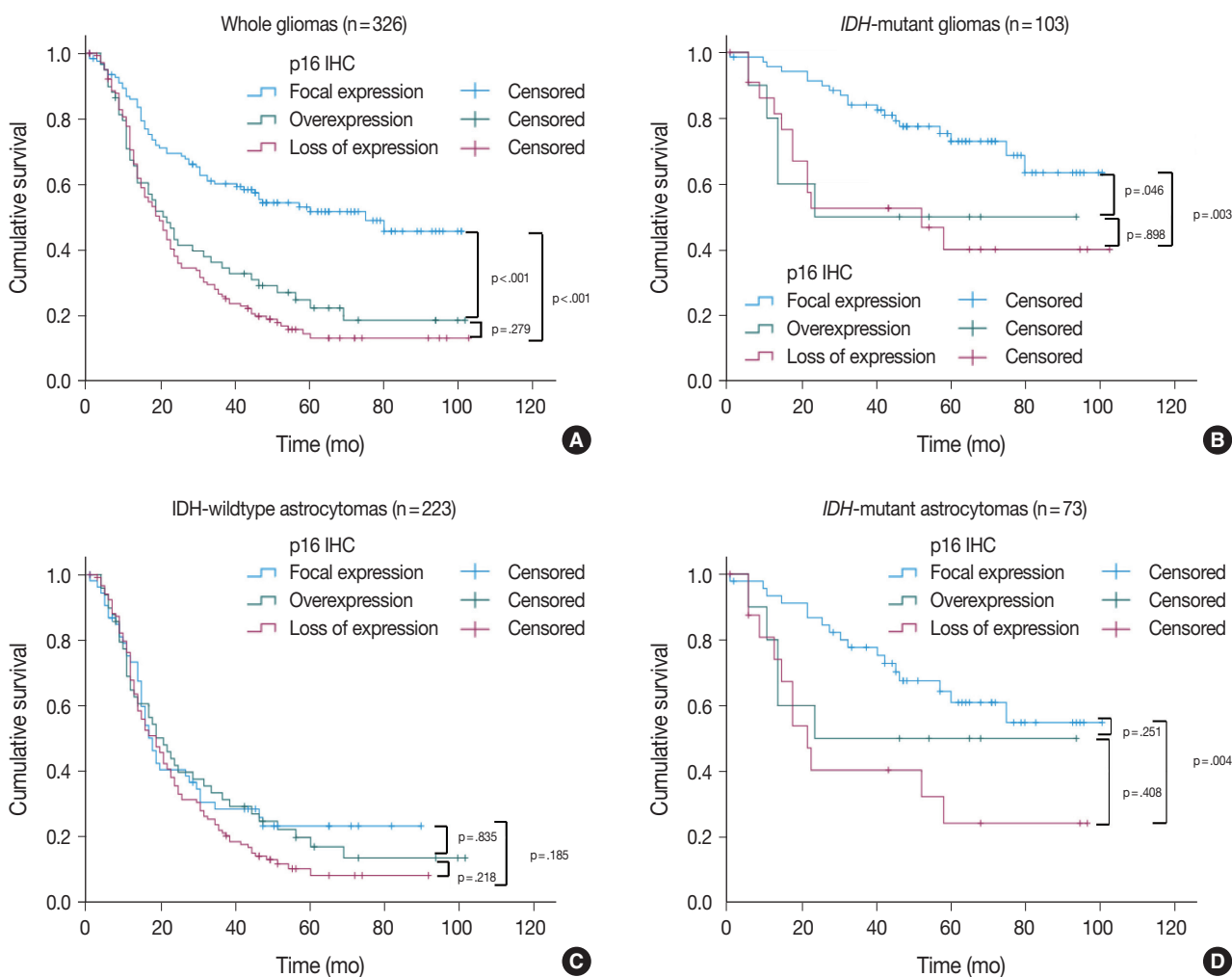


Fig. 4. Kaplan-Meier curves for overall survival according to the degree of p16 expression: (A) whole gliomas, (B) *IDH*-mutant gliomas including oligodendrogliomas, (C) *IDH*-wildtype astrocytomas, and (D) *IDH*-mutant astrocytomas. IHC, immunohistochemistry; *IDH*, isocitrate dehydrogenase.

nohistochemical staining in a large sample of molecularly characterized diffuse gliomas. Negative immunohistochemical staining of the p16 protein predicted worse overall survival in all glioma patients and in the IDH-mutant subgroup, especially in IDH-mutant astrocytomas, after adjusting for other prognostic factors such as tumor recurrence, p53 overexpression, and EGFR amplification. Our results were expected in light of existing knowledge that the p16 protein is encoded by the *CDKN2A* gene [1] and that *CDKN2A* homozygous deletion is a significant prognostic factor in IDH-mutant glioma patients [9,28]. In addition, when the p16 retained expression tumors were divided into two additional categories of overexpression and focal expression, the tumors with p16 overexpression also demonstrated worse outcomes compared to tumors with p16 focal expression in the whole gliomas and IDH-mutant gliomas including IDH-mutant astrocytomas and ODG. Considering that immunohistochemistry is a relatively simple and convenient test to be used in routine practice, assessing p16 protein expression patterns with immunohistochemical methods would be a useful way to predict glioma prognosis in the field.

Previously, several studies have examined the association between p16 immunohistochemistry and molecular tests such as PCR or FISH to detect *CDKN2A* deletions in glioma samples [5,13,29-31]. Some of them reported that the association was good, while others did not agree. Reis et al [5]. reported that p16 expression by immunohistochemistry correlated poorly with *CDKN2A* deletion by FISH, and suggested that FISH be used to evaluate *CDKN2A* status. This study differed from ours because the p16 immunohistochemistry data were used as continuous variables. In addition, this group counted the total number of signals regardless of whether the deletion pattern was hemizygous or homozygous when assessing the *CDKN2A* deletion by FISH. The problem with using the p16 expression data as a continuous variable is that it may not reflect the effect of p16 acting nonlinearly, as shown in our current study. In this study, Ki-67 was high in both the p16 loss and p16 overexpression subgroups, which was also associated with poor survival in each subgroup. The prior study appears to be the only study that has examined the relationship between p16 immunohistochemistry and survival in glioma patients molecularly diagnosed with both IDH and 1p/19q information to date. This group also found that there was a weak but significant association between p16 immunonegativity and poor overall survival in 83 astrocytoma patients.

In our study, although there was a correlation between *CDKN2A* FISH and p16 immunohistochemistry, the degree of agreement between the two tests was fair, or at most moderate. There-

fore, our results did not show a sufficient value to suggest that substitution between the two tests is reasonable. Fifty-five out of 197 (27.9%) tumors without *CDKN2A* homozygous deletion (determined by FISH) demonstrated a loss of p16 expression. In contrast, 41 out of 129 (31.8%) tumors with *CDKN2A* homozygous deletion (by FISH) demonstrated p16 immunopositivity in the present study. Such discrepancy may come from the fact that the expression of the p16 protein is controlled not only by cytogenetic alterations, but also by other mechanisms such as point mutations or epigenetic regulations such as EZH2 mediated transcriptional repression [31]. Furthermore, immunopositive cases with *CDKN2A* deletion by FISH may be due to a problem on the immunohistochemistry side, such as a hidden mixture of normal tissue. Alternatively, this result may also be due to a problem on the FISH side, such as a false-positive FISH result caused by partial hybridization failure, truncation artifacts, or a suboptimal cutoff value [32]. Similar false-positive FISH results were previously reported in another study on mesotheliomas [33], which were attributed to suboptimal hybridization of the FISH probes. False-positive FISH results may also be attributable to the heterogeneity of p16 immunostaining and *CDKN2A* deletions in the same tumor, as previously demonstrated in gliomas [34]. Given that FISH is relatively expensive, difficult to perform correctly, and requires a skilled technician, one must reconsider whether FISH is reliable and the gold standard of diagnosis. It is also noteworthy that p16 immunohistochemistry may function better as a prognostic marker than as a diagnostic one, because it reflects cases in which protein expression of the *CDKN2A* gene is suppressed by mechanisms other than deletion, such as epigenetic silencing or point mutations. In IDH-mutant gliomas, DNA methylation occurs frequently due to the so-called glioma CpG island methylator phenotype (G-CIMP) [35]. Detecting the absence of expressed proteins by immunohistochemistry may reflect a more ultimate situation than detecting the deletion of a gene by molecular testing.

In addition to p16 loss, we also examined whether the overexpression of p16 protein has any prognostic implications. Contrary to a cell cycle inhibitor's original function, p16 overexpressing tumors were found to have a high proliferation index as measured by Ki-67, and to have poor prognosis, especially in IDH mutated tumors. p16 is a component of the cell cycle regulation pathway that converges into the tumor suppressor protein Rb. Disruption of Rb results in p16 overexpression in cancer tissue due to positive feedback [21]. Nakamura et al. [36] found that loss of expression of the *RB1* gene was common in secondary glioblastoma. Therefore, the p16 overexpressing tumors observed

in our study may be tumors that have excessively increased their p16 level to compensate for the loss of Rb. Therefore, p16 overexpression seems to be a desperate effort to stop uncontrolled proliferation due to failure of the Rb pathway. Our finding that a high Ki-67 labeling index was observed in the p16 overexpression group is considered to be in good agreement with this situation. Therefore, for p16 overexpressing tumors, we must determine whether there is another genetic abnormality in the Rb pathway components that include *RB1* deletion or *CDK4/6* amplification, and whether this is associated with prognosis.

In the previous literature, there were inconsistent findings on whether a *CDKN2A* homozygous deletion was associated with poor survival in *IDH*-mutant and 1p/19q-codeleted ODGs [4,8, 28]. Similarly, our study did not show any prognostic significance of p16 protein loss in ODG. However, our results must be interpreted with caution given the small sample of ODG cases and a relatively short follow-up period for lower-grade gliomas. Therefore, further research is likely needed. It was also significant that p16 overexpression was not observed in all of our study's 30 ODGs. More samples are needed to confirm that the ODGs do not have p16 overexpression.

A limitation of this study is that it was retrospective in nature. Therefore, the data collection was inevitably limited, and other factors that may be related to prognosis were not all included or excluded. Most importantly, the FISH data should be reevaluated. We were not able to review these data because the preserved FISH pictures were limited. In addition, we cannot rule out the possibility that the immunohistochemical readings were overestimated or underestimated if the tumor had heterogeneous p16 expression, because the analysis was performed using TMA slides. Meanwhile, p16 overexpression was a statistically significant prognostic factor, which was confirmed in univariate analysis of *IDH*-mutant gliomas including astrocytomas and ODG. This significance was concealed after multivariate analysis or after being divided into subgroups, which may be due to insufficient sample sizes and short follow-up. Therefore, larger studies are necessary.

In summary, this study demonstrated that the pattern of p16 expression was significantly correlated with the prognosis in *IDH*-mutant glioma patients. p16 immunohistochemistry was correlated with *CDKN2A* FISH. The loss of p16 expression was strongly associated with shortened overall survival. In addition, the overexpression of p16 was also related to a worse outcome. We suggest that detecting p16 protein expression by immunohistochemistry could be used as a useful surrogate test or an initial screening assay to predict patient prognosis while replacing *CDKN2A* genetic testing. Nevertheless, further studies in other cohorts may

be required to confirm these results.

Ethics Statement

All procedures performed in the current study were approved by the Seoul National University Hospital Institutional Review Board (IRB No. H-2008-111-1150) in accordance with the 1964 Helsinki declaration and its amendments. Formal written informed was waived for cases collected before February 2013. Otherwise, informed consent was obtained from each patient.

ORCID

Jin Woo Park	https://orcid.org/0000-0003-0801-8208
Jeongwan Kang	https://orcid.org/0000-0002-2111-2912
Ka Young Lim	https://orcid.org/0000-0001-8240-6175
Hyunhee Kim	https://orcid.org/0000-0003-3353-1628
Seong-Ik Kim	https://orcid.org/0000-0001-7713-3782
Jae Kyung Won	https://orcid.org/0000-0003-1459-8093
Chul-Kee Park	https://orcid.org/0000-0002-2350-9876
Sung-Hye Park	https://orcid.org/0000-0002-8681-1597

Author Contributions

Conceptualization: SHP, JWP. Data curation: JWP, SHP. Formal analysis: JWP. Funding acquisition: SHP. Investigation: JWP, JK, KYL, HK, SIK, JKW, SHP. Methodology: JWP, SHP. Resources: CKP. Supervision: SHP. Writing—original draft: JWP. Writing—review & editing: JWP, SHP, JKW. Approval of final manuscript: all authors.

Conflicts of Interest

The authors declare that they have no potential conflicts of interest.

Funding Statement

This study was supported by a grant of the Korea Health Technology R&D Project through the Korea Health Industry Development Institute (KHI-DI), funded by the Ministry of Health & Welfare, Republic of Korea (grant number: HI14C1277).

References

1. Foulkes WD, Flanders TY, Pollock PM, Hayward NK. The *CDKN2A* (p16) gene and human cancer. *Mol Med* 1997; 3: 5-20.
2. Serrano M. The tumor suppressor protein p16INK4a. *Exp Cell Res* 1997; 237: 7-13.
3. Raschke S, Balz V, Efferth T, Schulz WA, Florl AR. Homozygous deletions of *CDKN2A* caused by alternative mechanisms in various human cancer cell lines. *Genes Chromosomes Cancer* 2005; 42: 58-67.
4. Appay R, Dehais C, Maurage CA, et al. *CDKN2A* homozygous deletion is a strong adverse prognosis factor in diffuse malignant *IDH*-mutant gliomas. *Neuro Oncol* 2019; 21: 1519-28.
5. Reis GF, Pekmezci M, Hansen HM, et al. *CDKN2A* loss is associated with shortened overall survival in lower-grade (World Health Organization Grades II-III) astrocytomas. *J Neuropathol Exp Neurol* 2015; 74: 442-52.
6. Shirahata M, Ono T, Stichel D, et al. Novel, improved grading system(s) for *IDH*-mutant astrocytic gliomas. *Acta Neuropathol* 2018; 136: 153-66.
7. Yang RR, Shi ZF, Zhang ZY, et al. *IDH* mutant lower grade (WHO Grades II/III) astrocytomas can be stratified for risk by *CDKN2A*, *CDK4* and *PDGFRA* copy number alterations. *Brain Pathol* 2020; 30: 541-53.

8. Aoki K, Nakamura H, Suzuki H, et al. Prognostic relevance of genetic alterations in diffuse lower-grade gliomas. *Neuro Oncol* 2018; 20: 66-77.
9. Brat DJ, Aldape K, Colman H, et al. cIMPACT-NOW update 5: recommended grading criteria and terminologies for *IDH*-mutant astrocytomas. *Acta Neuropathol* 2020; 139: 603-8.
10. Louis DN, Wesseling P, Aldape K, et al. cIMPACT-NOW update 6: new entity and diagnostic principle recommendations of the cIMPACT-Utrecht meeting on future CNS tumor classification and grading. *Brain Pathol* 2020; 30: 844-56.
11. Frazao L, do Carmo Martins M, Nunes VM, et al. *BRAF* V600E mutation and 9p21: *CDKN2A/B* and *MTAP* co-deletions: markers in the clinical stratification of pediatric gliomas. *BMC Cancer* 2018; 18: 1259.
12. Miettinen H, Kononen J, Sallinen P, et al. *CDKN2/p16* predicts survival in oligodendrogliomas: comparison with astrocytomas. *J Neurooncol* 1999; 41: 205-11.
13. Bortolotto S, Chiado-Piat L, Cavalla P, et al. *CDKN2A/p16* inactivation in the prognosis of oligodendrogliomas. *Int J Cancer* 2000; 88: 554-7.
14. Kirla R, Salminen E, Huhtala S, et al. Prognostic value of the expression of tumor suppressor genes p53, p21, p16 and p16, and Ki-67 labelling in high grade astrocytomas treated with radiotherapy. *J Neurooncol* 2000; 46: 71-80.
15. Jeon YK, Park K, Park CK, Paek SH, Jung HW, Park SH. Chromosome 1p and 19q status and p53 and p16 expression patterns as prognostic indicators of oligodendroglial tumors: a clinicopathological study using fluorescence in situ hybridization. *Neuropathology* 2007; 27: 10-20.
16. Puduvalli VK, Kyritsis AP, Hess KR, et al. Patterns of expression of Rb and p16 in astrocytic gliomas, and correlation with survival. *Int J Oncol* 2000; 17: 963-9.
17. Arifin MT, Hama S, Kajiwara Y, et al. Cytoplasmic, but not nuclear, p16 expression may signal poor prognosis in high-grade astrocytomas. *J Neurooncol* 2006; 77: 273-7.
18. Milde-Langosch K, Bamberger AM, Rieck G, Kelp B, Loning T. Overexpression of the p16 cell cycle inhibitor in breast cancer is associated with a more malignant phenotype. *Breast Cancer Res Treat* 2001; 67: 61-70.
19. O'Neill CJ, McCluggage WG. p16 expression in the female genital tract and its value in diagnosis. *Adv Anat Pathol* 2006; 13: 8-15.
20. Lam AK, Ong K, Giv MJ, Ho YH. p16 expression in colorectal adenocarcinoma: marker of aggressiveness and morphological types. *Pathology* 2008; 40: 580-5.
21. Romagosa C, Simonetti S, Lopez-Vicente L, et al. p16(Ink4a) overexpression in cancer: a tumor suppressor gene associated with senescence and high-grade tumors. *Oncogene* 2011; 30: 2087-97.
22. Chaurasia A, Park SH, Seo JW, Park CK. Immunohistochemical analysis of ATRX, IDH1 and p53 in glioblastoma and their correlations with patient survival. *J Korean Med Sci* 2016; 31: 1208-14.
23. Koh J, Cho H, Kim H, et al. *IDH2* mutation in gliomas including novel mutation. *Neuropathology* 2015; 35: 236-44.
24. Kim SI, Lee Y, Won JK, Park CK, Choi SH, Park SH. Reclassification of mixed oligoastrocytic tumors using a genetically integrated diagnostic approach. *J Pathol Transl Med* 2018; 52: 28-36.
25. Chung CT, Santos Gda C, Hwang DM, et al. FISH assay development for the detection of p16/CDKN2A deletion in malignant pleural mesothelioma. *J Clin Pathol* 2010; 63: 630-4.
26. Berger AH, Knudson AG, Pandolfi PP. A continuum model for tumour suppression. *Nature* 2011; 476: 163-9.
27. Lotan TL, Wei W, Ludkovski O, et al. Analytic validation of a clinical-grade PTEN immunohistochemistry assay in prostate cancer by comparison with PTEN FISH. *Mod Pathol* 2016; 29: 904-14.
28. Lu VM, O'Connor KP, Shah AH, et al. The prognostic significance of *CDKN2A* homozygous deletion in *IDH*-mutant lower-grade glioma and glioblastoma: a systematic review of the contemporary literature. *J Neurooncol* 2020; 148: 221-9.
29. Burns KL, Ueki K, Jhung SL, Koh J, Louis DN. Molecular genetic correlates of p16, cdk4, and pRb immunohistochemistry in glioblastomas. *J Neuropathol Exp Neurol* 1998; 57: 122-30.
30. Purkait S, Jha P, Sharma MC, et al. *CDKN2A* deletion in pediatric versus adult glioblastomas and predictive value of p16 immunohistochemistry. *Neuropathology* 2013; 33: 405-12.
31. Purkait S, Sharma V, Jha P, et al. *EZH2* expression in gliomas: correlation with *CDKN2A* gene deletion/ p16 loss and MIB-1 proliferation index. *Neuropathology* 2015; 35: 421-31.
32. Fuller CE, Perry A. Fluorescence in situ hybridization (FISH) in diagnostic and investigative neuropathology. *Brain Pathol* 2002; 12: 67-86.
33. Chiosea S, Krasinskas A, Cagle PT, Mitchell KA, Zander DS, Dacic S. Diagnostic importance of 9p21 homozygous deletion in malignant mesotheliomas. *Mod Pathol* 2008; 21: 742-7.
34. Piva R, Cavalla P, Bortolotto S, et al. *CDKN2/p16* inactivation and p16 immunohistochemistry in astrocytic gliomas. *Int J Oncol* 1998; 12: 55-8.
35. Noushmehr H, Weisenberger DJ, Diefes K, et al. Identification of a CpG island methylator phenotype that defines a distinct subgroup of glioma. *Cancer Cell* 2010; 17: 510-22.
36. Nakamura M, Yonekawa Y, Kleihues P, Ohgaki H. Promoter hypermethylation of the *RBI* gene in glioblastomas. *Lab Invest* 2001; 81: 77-82.

A study of pathological characteristics and *BRAF* V600E status in Langerhans cell histiocytosis of Vietnamese children

Thu Dang Anh Phan¹, Bao Gia Phung², Tu Thanh Duong¹, Vu Anh Hoang³,
Dat Quoc Ngo¹, Nguyen Dinh The Trinh⁴, Tung Thanh Tran⁴

¹Department of Pathology, University of Medicine and Pharmacy at Ho Chi Minh City, Ho Chi Minh City;

²Department of Pathology, City Children Hospital, Ho Chi Minh City;

³Center for Molecular Biomedicine, University of Medicine and Pharmacy at Ho Chi Minh City, Ho Chi Minh City;

⁴Department of Pathology, Children Hospital 1, Ho Chi Minh City, Vietnam

Background: Langerhans cell histiocytosis (LCH) is more common in children than adults and involves many organs. In children, the *BRAF* V600E mutation is associated with recurrent and high-risk LCH. **Methods:** We collected paraffin blocks of 94 pediatric LCH patients to detect *BRAF* V600E mutation by sequencing. The relationship between *BRAF* V600E status and clinicopathological parameters were also critically analyzed. **Results:** *BRAF* V600E mutation exon 15 was detected in 45 cases (47.9%). Multiple systems LCH showed a significantly higher *BRAF* V600E mutation rate than a single system ($p = .001$). No statistical significance was evident for other clinical characteristics such as age, sex, location, risk organs involvement, and CD1a expression. **Conclusions:** In Vietnamese LCH children, the proportion of *BRAF* V600E mutational status was relatively high and related to multiple systems.

Key Words: Langerhans cell histiocytosis; *BRAF* V600E mutation; Sequencing

Received: July 27, 2020 **Revised:** November 22, 2020 **Accepted:** November 30, 2020

Corresponding Author: Thu Dang Anh Phan, MD, PhD, Department of Pathology, University of Medicine and Pharmacy at Ho Chi Minh City, Ho Chi Minh City 700000, Vietnam
Tel: +84-838-558-411, Fax: +84-838-552-304, E-mail: phandanganhthu@ump.edu.vn

Langerhans cell histiocytosis (LCH) is a rare disease defined by proliferation of Langerhans cells with highly heterogeneous presentations and clinical courses [1,2]. The condition can occur at any age but is more common in children. LCH can involve one organ, so-called single system, or more than one organ, termed multisystem or multiple systems (MS-LCH). LCH has been referred to by various names, including localized eosinophilic granuloma of the bone, Letterer-Siwe disease, Hand-Schuller-Christian disease, and histiocytosis X [3,4]. Children under 2 years old with MS-LCH commonly exhibit risk organ involvement, such as the liver, spleen, and hematopoietic system. Although typical morphology can identify the pathologic Langerhans cells, confirming their nature requires positive staining for CD1a and CD207 or identifying Birbeck particles under electron microscopy [5,6].

The clinical prognosis of LCH can be extremely variable. The patients with multiple systems, risk organ involvement likely have a more unsatisfactory outcome and are at risk for reactiva-

tions [7]. Fortunately, recent molecular findings promise a targeted therapy for high-risk pediatric patients with risk organ involvement, for those who fail standard treatment and those with relapses [4].

BRAF is an oncogene that has a critical role in the Ras-ERK signaling cascade, a primary regulator of cell growth, proliferation, differentiation, and apoptosis. Therefore, *BRAF* mutations contribute to many human cancers' pathogenesis, most commonly melanoma, thyroid papillary carcinoma, and colorectal carcinoma [8,9]. The primary mutation point is the valine codon in position 600 located in exon 15 (V600E mutation), which replaces nucleotide at 1799 T → A in the *BRAF* gene, resulting in the replacement of valine amino acid by glutamate [8-10].

The *BRAF* V600E mutation is also the potential target for treatment with Vemurafenib—an inhibitor used in many malignancies, most notably melanoma, and recently reported in LCH [9,11]. Thus, *BRAF* V600E may be a potential marker for targeted therapy in aggressive LCH. Several studies have shown

that the presence of *BRAF* V600E mutation is associated with a higher risk of recurrence and organ involvement in pediatric LCH [12-14]. This study analyzed the *BRAF* V600E mutation by sequencing tumor DNA and the relationship between the genetic alteration and clinicopathological characteristics of LCH children.

MATERIALS AND METHODS

Patients and sample collection

The study consisted of 94 cases diagnosed with LCH at the Department of Pathology, Children’s Hospital 1, Ho Chi Minh City, Vietnam, from 2012 to 2018. Formalin-fixed paraffin-embedded (FFPE) tissue with well-defined histology of LCH on hematoxylin and eosin (H&E) stained sections and positive CD1a staining (using monoclonal antibody CD1a, clone 010, Dako, Glostrup, Denmark) were collected. We analyzed the intensity of CD1a expression as low expression (moderate membrane and cytoplasmic staining) and high expression (strong membrane and cytoplasmic staining).

All paraffin blocks were well preserved and available for DNA sequencing. All slides were re-examined to confirm the diagnosis and to select the paraffin blocks for molecular testing. Clinical information, age, sex, location, histopathology, and risk organ were obtained.

Analysis of *BRAF* V600E mutation

Tumor cells were selected based on H&E slides and were targeted for DNA extraction by macrodissection scraping. DNA was isolated from a 5-µm-thick tumor using the ReliaPrep FFPE gDNA Miniprep System kit (Promega, Madison, WI, USA) according to the manufacturer’s protocol. Amplification of the *BRAF* exon 15 was performed using TaKaRa Taq HotStart Polymerase (Takara Bio, Shiga, Japan) with primers *BRAF*-600F (5'-ACTCTTCATAATGCTTGCTC-3') and *BRAF*-600R (5'-CCACAAAATGGATCCAGACA-3'). Polymerase chain reaction (PCR) included initial denaturation at 98°C for 3 minutes followed by 45 cycles of 98°C for 10 seconds, 60°C for 30 seconds, and 72°C for 40 seconds, with a final elongation of 72°C for 2 minutes. PCR product was purified enzymatically using the ExoSAP IT PCR Product Cleanup Reagent (Thermo Scientific, Waltham, MA, USA) to remove excess primers and dNTPs before Sanger sequencing using the BigDye Terminator v3.1 Kit and the ABI 3500 Genetic Analyzer (Applied Biosystems, Foster City, CA, USA). PCR fragment was sequenced and analyzed in both directions. The sequence was finally compared to

the reference sequence of the *BRAF* gene (GenBank accession number: NG_007873).

Statistical analyses

The correlation between *BRAF* V600E mutation and age, sex, tumor location, and organ involvement was analyzed by the chi-square test. $p < .05$ was considered a significant difference. Statistical analyses were performed using SPSS ver. 16.0 (SPSS Inc., Chicago, IL, USA).

RESULTS

Characteristics of pediatric LCH

In 94 cases of LCH, the median age was 3.02 years (range, 0 to 12 years; minimum, 10 days old). LCH was most frequently found in the age group of under 3 (60.6%), in which 1-year-old patients were predominant (56.1%, 32/ 57 cases). LCH was more common in males than in females, with a male: female ratio of 1.4. Soft tissues were the most common biopsy location (n = 39, 41.5%), followed by the skin (n = 30, 31.9%), bones (n = 18, 19.1%), lymph nodes (n = 6, 6.4%) and lung (n = 1, 1.1%). The clinicopathologic features are summarized in Table 1. Forty-eight patients (51.1%) had single system involved, while 46 patients (48.9%) had multiple systems involved. Risk organ involvement was observed in 35 patients (37.2%). The Langerhans cells were pathologically characterized by abundant pale cyto-

Table 1. The clinical characteristics and *BRAF* V600E status of Vietnamese pediatric Langerhans cell histiocytosis

Clinical parameter	Total	<i>BRAF</i> V600E mutated
No.	94	45 (47.9)
Age (yr)	3.0 ± 2.9 (0–12 yr; minimum, 10 days)	
Under 3 yr	57 (60.6)	27 (46.6)
Sex		
Male	55 (58.5)	25 (55.6)
Female	39 (41.5)	20 (44.4)
Location		
Skin	30 (31.9)	13 (28.9)
Lymph node	6 (6.4)	2 (4.4)
Soft tissues	39 (41.5)	23 (51.1)
Bone	18 (19.1)	7 (15.5)
Lung	1 (1.1)	0
System involvement		
Single system	48 (51.1)	15 (31.3)
Multiple system	46 (48.9)	30 (65.2)
Risk organ involvement	35 (37.2)	18 (51.4)
CD1a expression		
Low	31 (33.0)	12 (38.7)
High	63 (67.0)	33 (52.4)

Values are presented as number (%).

plasm and folded nuclei (Fig. 1) that expressed CD1a. The intensity of CD1a staining was also divided into low and high expression (33% vs. 67%).

BRAF mutation analysis

Sequencing analyses for all 94 patients successfully defined *BRAF* V600E status. *BRAF* V600E mutation exon 15 was found in 45 cases (47.9%) (Fig. 2). In Table 2, we demonstrate the relation between *BRAF* V600E mutation and clinical parameters. Multiple system LCH showed a significantly higher *BRAF* V600E mutation rate than the single system LCH ($p = .001$). There was no significant difference between *BRAF* status and other clinical characteristics such as age, sex, location, risk organs involvement, and CD1a expression.

DISCUSSION

BRAF mutations play the leading role in the oncogenesis of human cancers because of their involvement in the Ras-ERK signaling cascade, which regulates cellular motility, proliferation, and survival. Recent studies have found somatic mutations that trigger mitogen-activated protein kinase signaling in most LCH patients [13,15-19]. In particular, the *BRAF* V600E mutation is found in more than 50% of LCH lesions in children, while other modifications of the codon V600 such as V600K, V600D, or V600R are not present in this disease [20]. The *BRAF* mutation presentation appears to be complicated; however, the most common point mutation is V600E (the valine codon in position 600, located in exon 15). Most *BRAF* mutations are detected in

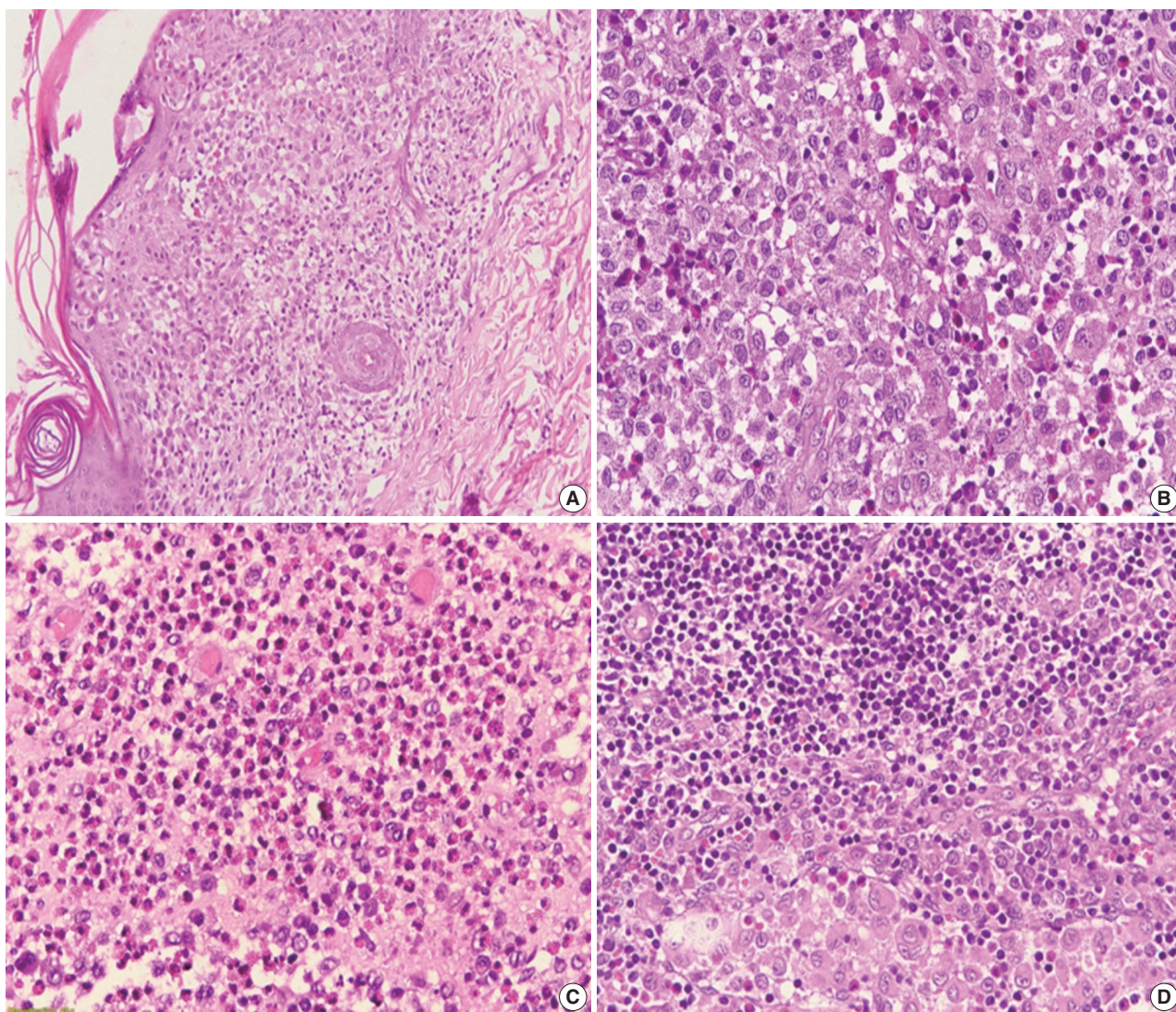


Fig. 1. Langerhans cell histiocytosis on hematoxylin and eosin staining: (A) skin lesion, (B) soft tissue of the head and neck, (C) bone lesion, and (D) lymph node lesion.

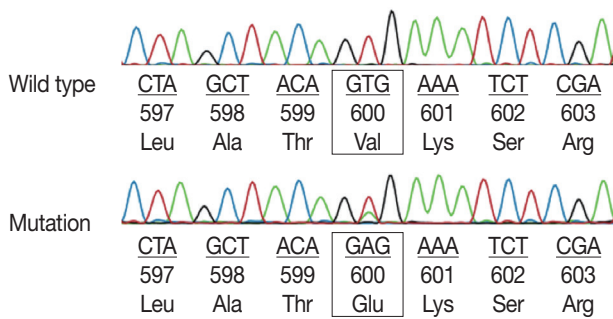


Fig. 2. The *BRAF* V600E status in pediatric Langerhans cell histiocytosis.

Table 2. The correlation of *BRAF* V600E status and clinical parameters of Vietnamese LCH patients (n=94)

Clinical parameter	<i>BRAF</i> V600E mutated	<i>BRAF</i> V600E Wild type	p-value
Age (yr)			.903
<3	27	30	
≥3	18	19	
Sex			.577
Male	25	30	
Female	20	19	
Skin lesions			.546
Present	13	17	
Absent	32	32	
Soft tissue			.070
Present	23	16	
Absent	22	33	
Bone lesions			.396
Present	7	11	
Absent	38	38	
System involvement			.001
Single system	15	33	
Multiple systems	30	16	
Risk organ involvement	18	17	.595
CD1a expression			.212
Low	12	19	
High	33	30	

LCH, Langerhans histiocytosis; NS, nonsignificant.

exons 11 and 15 by DNA-based sequencing assays [8]. In particular, more than 80% of all *BRAF* mutations are in exon 15, which results in changing valine for glutamic acid at codon 600 (V600E) [10]. Exon 11 mutations seem to be rare in LCH. Alayed et al. [21] detected *BRAF* mutations in LCH by pyrosequencing assays and found exon 15 *BRAF* V600E mutation and no exon 11 mutations in all cases.

This study found 47.9% of cases with *BRAF* mutations detected in exon 15 (*BRAF* V600E). Our data showed that the *BRAF* V600E mutation in Vietnamese pediatric LCH was relatively high but unrelated to sex, age, and risk organ involvement. In previous studies on Caucasian children, *BRAF* mutation frequency varied from 33% to 69% [12,13,16,19,22]. The study of Heritier et al. [12] on 315 pediatric LCH patients determined

173 cases (54.6%) with *BRAF* V600E mutation. They also showed a significant relationship between *BRAF* V600E mutation with age under 3 years old and multisystem disease, mostly when there was a risk of organ involvement. Badalian-Very et al. [23] also reported that the incidence of *BRAF* V600E mutation was 57% in 61 LCH patients, predominantly in patients with bone involvement. The mutation rate was also reportedly higher in young patients, especially children under age 15. Ozer et al. [24] showed that 70% of pediatric LCH patients younger than 2 years of age significantly harbored *BRAF* V600E mutation. However, the ratio of *BRAF* V600E status in pediatric LCH reported in some Asian populations was lower. Sasaki et al. [25] demonstrated 21% *BRAF* V600E mutations in Japanese patients (4/19 cases); Go et al. [26] showed 25% (7/28 cases) in South Korean patients. These studies showed a different *BRAF* V600E status across the various population, which raised a possible question of racial involvement on genetic profile.

Moreover, the *BRAF* V600E mutation status showed variable distribution in some specific organs. Liu et al. [27] showed that 50% of bone lesions in the head and neck (18/36 cases) were identified with *BRAF* V600E mutation. Other studies found the transformation in over 70% of skin cases [12,24], especially in multifocal skin involvement and multisystem disease. In the present study, the *BRAF* V600E mutation was detected mostly in LCH of the soft tissues (51.1%), followed by skin (28.9%), bone (15.5%), and lymph nodes (4.4%). In our study, 13/30 (43.3%) skin cases harbored *BRAF* V600E mutation, lower than Ozer et al. [24] (77.8%) and Heritier et al. [12] (77.0%). False-negative results may occur in small-sized tumors such as skin lesions due to an insufficient amount of tumor cells. In this study, 7/18 (38.9%) cases of LCH bone lesions harbored *BRAF* mutation; therefore, the current decalcifying solution possibly did little harm to DNA quality. Furthermore, no significant relation between *BRAF* V600E status and LCH location was observed in this study and others [12,24].

In 94 patients of this study, *BRAF* V600E mutation was significantly associated with multisystem involvement (p=0.001). Similarly, Heritier et al. [12] showed that *BRAF* V600E mutation correlated with high-risk LCH, including multiple systems and risk organ involvement, resulting in permanent, irreversible damage. Adding to these points, Heritier et al. [12] showed that patients with *BRAF* V600E more commonly displayed resistance to combined vinblastine corticosteroid therapy, higher reactivation rate, long-term consequences from disease or treatment. Ozer et al. [24] also found a statistical relationship between *BRAF* mutation and risk organ lesions. However, in this study, risk or-

gan lesions showed no significant relation to *BRAF* status. The prevalence of LCH *BRAF* mutation and its association with increased risk condition such as multiple systems or risk organs involvement possibly suggests a targeted treatment using *BRAF* inhibitors for those that harbor the mutation.

In conclusion, the *BRAF* V600E status was detected with high frequency in Vietnamese pediatric LCH and may become a useful prognostic marker due to its association with multiple system LCH. The identification of aggressive LCH based on genetic alterations is required for disease management and *BRAF* inhibitors.

Ethics Statement

The study was approved by the Institutional Review Board of Biomedical Research at the Children's Hospital (IRB No. 1693/Children's Hospital 1; date: July 22, 2019) and performed in accordance with the principles of the Declaration of Helsinki. Written informed consents were obtained.

ORCID

Thu Dang Anh Phan	https://orcid.org/0000-0002-4062-0904
Bao Gia Phung	https://orcid.org/0000-0002-0875-1285
Tu Thanh Duong	https://orcid.org/0000-0002-6564-6799
Vu Anh Hoang	https://orcid.org/0000-0003-4232-6001
Dat Quoc Ngo	https://orcid.org/0000-0003-1461-0216
Nguyen Dinh The Trinh	https://orcid.org/0000-0001-6236-3892
Tung Thanh Tran	https://orcid.org/0000-0001-5511-7175

Author Contributions

Conceptualization: TDAP, BGP, TTD, VAH, DQN, NDTT, TTT. Data curation: TDAP, BGP, TTD. Formal analysis: TDAP, BGP, TTD. Funding acquisition: TDAP, BGP, TTD. Methodology: TDAP, BGP, TTD, VAH. Re-sources: NDTT, TTT, TDAP, BGP. Supervision: DQN, NDTT, TTT. Writing—original draft: TDAP, BGP, TTD. Writing—review & editing: TDAP, DQN. Approval of final manuscript: all authors.

Conflicts of Interest

The authors declare that they have no potential conflicts of interest.

Funding Statement

This work was funded partly by the University of Medicine and Pharmacy at Ho Chi Minh city.

Acknowledgments

We thank Professor Lewis Hassell, Department of Pathology, Oklahoma University Health Sciences Center, for English proofreading.

References

- Guyot-Goubin A, Donadieu J, Barkaoui M, Bellec S, Thomas C, Clavel J. Descriptive epidemiology of childhood Langerhans cell histiocytosis in France, 2000-2004. *Pediatr Blood Cancer* 2008; 51: 71-5.
- Salotti JA, Nanduri V, Pearce MS, Parker L, Lynn R, Windebank KP. Incidence and clinical features of Langerhans cell histiocytosis in the UK and Ireland. *Arch Dis Child* 2009; 94: 376-80.
- Arceci RJ. The histiocytoses: the fall of the Tower of Babel. *Eur J Cancer* 1999; 35: 747-67.
- Gadner H, Minkov M, Grois N, et al. Therapy prolongation improved outcome in multisystem Langerhans cell histiocytosis. *Blood* 2013; 121: 5006-14.
- Abla O, Weitzman S. Treatment of Langerhans cell histiocytosis: role of BRAF/MAPK inhibition. *Hematology Am Soc Hematol Educ Program* 2015; 2015: 565-70.
- Birbeck MS, Breathnach AS, Everall JD. An electron microscope study of basal melanocytes and high-level clear cells (Langerhans cell) in vitiligo. *J Invest Dermatol* 1961; 37: 51-64
- Minkov M. Multisystem Langerhans cell histiocytosis in children: current treatment and future directions. *Paediatr Drugs* 2011; 13: 75-86.
- Davies H, Bignell GR, Cox C, et al. Mutations of the *BRAF* gene in human cancer. *Nature* 2002; 417: 949-54.
- Fiskus W, Mitsiades N. B-Raf inhibition in the clinic: present and future. *Annu Rev Med* 2016; 67: 29-43.
- Wooster R, Futreal AP, Stratton MR. Sequencing analysis of *BRAF* mutations in human cancers. *Methods Enzymol* 2006; 407: 218-24.
- Ascierto PA, Kirkwood JM, Grob JJ, et al. The role of *BRAF* V600 mutation in melanoma. *J Transl Med* 2012; 10: 85.
- Heritier S, Emile JF, Barkaoui MA, et al. *BRAF* mutation correlates with high-risk Langerhans cell histiocytosis and increased resistance to first-line therapy. *J Clin Oncol* 2016; 34: 3023-30.
- Berres ML, Lim KP, Peters T, et al. *BRAF*-V600E expression in precursor versus differentiated dendritic cells defines clinically distinct LCH risk groups. *J Exp Med* 2015; 212: 281.
- Mehes G, Irsai G, Bedekovics J, et al. Activating *BRAF* V600E mutation in aggressive pediatric Langerhans cell histiocytosis: demonstration by allele-specific PCR/direct sequencing and immunohistochemistry. *Am J Surg Pathol* 2014; 38: 1644-8.
- Brown NA, Furtado LV, Betz BL, et al. High prevalence of somatic *MAP2K1* mutations in *BRAF* V600E-negative Langerhans cell histiocytosis. *Blood* 2014; 124: 1655-8.
- Haroche J, Charlotte F, Arnaud L, et al. High prevalence of *BRAF* V600E mutations in Erdheim-Chester disease but not in other non-Langerhans cell histiocytoses. *Blood* 2012; 120: 2700-3.
- Nelson DS, Quispel W, Badalian-Very G, et al. Somatic activating *ARAF* mutations in Langerhans cell histiocytosis. *Blood* 2014; 123: 3152-5.
- Sahm F, Capper D, Preusser M, et al. *BRAF*V600E mutant protein is expressed in cells of variable maturation in Langerhans cell histiocytosis. *Blood* 2012; 120: e28-34.
- Satoh T, Smith A, Sarde A, et al. *B-RAF* mutant alleles associated with Langerhans cell histiocytosis, a granulomatous pediatric disease. *PLoS One* 2012; 7: e33891.
- Ballester LY, Cantu MD, Lim KP, et al. The use of *BRAF* V600E mutation-specific immunohistochemistry in pediatric Langerhans cell histiocytosis. *Hematol Oncol* 2018; 36: 307-15.
- Alayed K, Medeiros LJ, Patel KP, et al. *BRAF* and *MAP2K1* mutations in Langerhans cell histiocytosis: a study of 50 cases. *Hum Pathol* 2016; 52: 61-7.
- Roden AC, Hu X, Kip S, et al. *BRAF* V600E expression in Langerhans cell histiocytosis: clinical and immunohistochemical study on 25 pulmonary and 54 extrapulmonary cases. *Am J Surg Pathol* 2014; 38: 548-51.
- Badalian-Very G, Vergilio JA, Degar BA, et al. Recurrent *BRAF* mutations in Langerhans cell histiocytosis. *Blood* 2010; 116: 1919-23.
- Ozer E, Sevinc A, Ince D, Yuzuguldu R, Olgun N. *BRAF* V600E

- mutation: a significant biomarker for prediction of disease relapse in pediatric Langerhans cell histiocytosis. *Pediatr Dev Pathol* 2019; 22: 449-55.
25. Sasaki Y, Guo Y, Arakawa F, et al. Analysis of the *BRAF*V600E mutation in 19 cases of Langerhans cell histiocytosis in Japan. *Hematol Oncol* 2017; 35: 329-34.
 26. Go H, Jeon YK, Huh J, et al. Frequent detection of *BRAF*(V600E) mutations in histiocytic and dendritic cell neoplasms. *Histopathology* 2014; 65: 261-72.
 27. Liu X, Zhang Y, Zhou CX. High prevalence of *BRAF* V600E mutations in Langerhans cell histiocytosis of head and neck in Chinese patients. *Int J Surg Pathol* 2019; 27: 836-43.

Deep learning for computer-assisted diagnosis of hereditary diffuse gastric cancer

Sean A. Rasmussen¹, Thomas Arnason¹, Weei-Yuarn Huang²

¹Department of Pathology and Laboratory Medicine, Queen Elizabeth II Health Sciences Centre and Dalhousie University, Halifax, NS;

²Department of Laboratory Medicine and Molecular Diagnostics, Sunnybrook Health Science Center, University of Toronto, Toronto, ON, Canada

Background: Patients with hereditary diffuse gastric cancer often undergo prophylactic gastrectomy to minimize cancer risk. Because intramucosal poorly cohesive carcinomas in this setting are typically not grossly visible, many pathologists assess the entire gastrectomy specimen microscopically. With 150 or more slides per case, this is a major time burden for pathologists. This study utilizes deep learning methods to analyze digitized slides and detect regions of carcinoma. **Methods:** Prophylactic gastrectomy specimens from seven patients with germline *CDH1* mutations were analyzed (five for training/validation and two for testing, with a total of 133 tumor foci). All hematoxylin and eosin slides containing cancer foci were digitally scanned, and patches of size 256×256 pixels were randomly extracted from regions of cancer as well as from regions of normal background tissue, resulting in 15,851 images for training/validation and 970 images for testing. A model with DenseNet-169 architecture was trained for 150 epochs, then evaluated on images from the test set. External validation was conducted on 814 images scanned at an outside institution. **Results:** On individual patches, the trained model achieved a receiver operating characteristic (ROC) area under the curve (AUC) of 0.9986. This enabled it to maintain a sensitivity of 90% with a false-positive rate of less than 0.1%. On the external validation dataset, the model achieved a similar ROC AUC of 0.9984. On whole slide images, the network detected 100% of tumor foci and correctly eliminated an average of 99.9% of the non-cancer slide area from consideration. **Conclusions:** Overall, our model shows encouraging progress towards computer-assisted diagnosis of hereditary diffuse gastric cancer.

Key Words: Machine learning; Pathology; Computer-assisted diagnosis; Stomach neoplasms; Deep learning

Received: June 9, 2020 **Revised:** December 22, 2020 **Accepted:** December 22, 2020

Corresponding Author: Sean A. Rasmussen, MD, PhD, Division of Anatomical Pathology, Queen Elizabeth II Health Sciences Centre and Dalhousie University, 7th floor, MacKenzie Building, 5788 University Ave, Halifax, NS B3H 1V8, Canada
 Tel: +1-289-925-6176, Fax: +1-902-473-1049, E-mail: sean.rasmussen@nshealth.ca

Patients with germline mutations in the *CDH1* gene are at high risk for gastric poorly cohesive (signet ring cell) carcinoma, also referred to as hereditary diffuse gastric cancer. To minimize the risk, current guidelines recommend that patients undergo prophylactic gastrectomy prior to developing symptomatic cancer [1]. In many of the prophylactic gastrectomy specimens from these patients, there is no grossly visible lesion. Consequently, many pathology labs have a protocol of submitting the entire stomach for microscopic examination to determine whether the patient had any evidence of cancer at the time of gastrectomy. This requires the assessment of hundreds of hematoxylin and eosin (H&E) slides for each case, which represents a significant cost to the healthcare system in terms of pathologist time. Furthermore, patients often wait an extended period of time to receive

a final diagnosis because of the time required for this analysis. Increased efficiency in the analysis of these specimens would represent a significant benefit in terms of both resource utilization and patient care. This study utilizes deep learning methods to automatically analyze digitized H&E slides from prophylactic gastrectomy specimens and detect regions suspicious for intramucosal signet ring cell carcinoma.

In recent years, deep learning methods using convolutional neural networks (CNNs) have emerged as the most powerful tools for automated medical image analysis. For example, these models have shown impressive accuracy detecting pneumonia from chest radiographs [2] or retinopathy from retinal fundus images [3]. With the advent of digital pathology, it is becoming increasingly feasible to apply these same strategies to whole slide

images in pathology. Several groups have already begun to examine tasks in pathology that might benefit from computer assistance. Relatively large-scale efforts have shown that CNNs can help to identify metastases in lymph nodes [4,5] or mitotic figures in breast cancer [6]. Importantly, it has recently been shown that pathologists working with the assistance of CNNs to identify lymph node metastases can achieve superior speed and accuracy relative to pathologists working without computer assistance [7].

In the current study, we create the first dataset of manually annotated digitized histopathology images of hereditary diffuse gastric cancer. Using this data, we train a model using DenseNet-169 architecture [8]. This is an efficient model architecture [9] that utilizes direct connections between early and late layers in the model without requiring that information pass through intermediate layers. It has previously demonstrated strong performance on a variety of pathology image classification tasks [10]. With this model, we address two key questions. First, can a CNN be trained to accurately classify individual small images of hereditary diffuse gastric cancer? Second, can such a trained model be applied to large whole slide images to effectively highlight areas containing signet ring cell carcinoma?

MATERIALS AND METHODS

Patients and data collection

The lab information system at our institution was searched to identify seven consecutive patients with established germline *CDH1* mutations who underwent prophylactic total gastrectomy. All patients had foci of intramucosal carcinoma identified microscopically. Patients were not excluded based on age, sex, or medical history. The seven patients we identified included four female and three male patients. The age at the time of gastrectomy ranged from 35 to 59 years (mean, 42.9 years). The number of slides containing intramucosal signet ring cell carcinoma ranged from 5 to 24 per case (mean, 13.4), and the number of lesions per slide ranged from 1 to 7 (mean, 1.4).

The seven gastrectomy specimens were divided into training and testing datasets. Five cases were used for training and optimizing the model, and two cases were reserved for testing so that no data from these test cases would be seen by the model prior to the final analysis.

For all H&E slides from the gastrectomy specimens, foci of intramucosal signet ring cell carcinoma were identified by one of the gastrointestinal pathologists at our institution. The slides with cancer were digitally scanned at $200\times$ ($0.496\ \mu\text{m}$ per pixel) magnification using an Aperio ScanScope XT (Leica Biosys-

tems, Concord, ON, Canada). Within each scanned whole slide image, regions containing cancer were manually annotated by a pathology resident using QuPath v0.2.0-m2 software [11]. Patches of size 256×256 pixels were then randomly extracted from these regions such that the central 128×128 pixel region overlapped with annotated cancer. The number of patches extracted per lesion was based on the size of the carcinoma focus, such that there was one patch per $2,000\ \mu\text{m}^2$ of carcinoma. In the case of tumor foci smaller than $2,000\ \mu\text{m}^2$, two patches were extracted. To create patches of normal gastric tissue, a total of 150 representative normal regions were digitally scanned (116 from training cases, 34 from test cases). 256×256 pixel patches were then randomly extracted from these regions, with the number of extracted patches per region chosen to create roughly balanced datasets in both the training and test groups. For test cases, this resulted in 15 patches per region being extracted, and for training cases (where the tumor foci were larger on average) this resulted in 70 patches per region being extracted.

In total, 94 H&E slides were scanned and 133 individual tumor foci were manually annotated. An example of a manually annotated tumor region is shown in Fig. 1, illustrating the complex borders of some tumor foci. A total of 16,822 patches were extracted, distributed between training and testing sets as shown in Fig. 2. Signet ring cell carcinoma was present in 8,192 of these patches, while the remaining 8,630 patches contained only background gastric tissue.

To create an external validation dataset, the lab information system at an outside institution (Sunnybrook Health Sciences Centre, Toronto, ON, Canada) was searched to identify recent cases with suspected or confirmed hereditary diffuse gastric can-

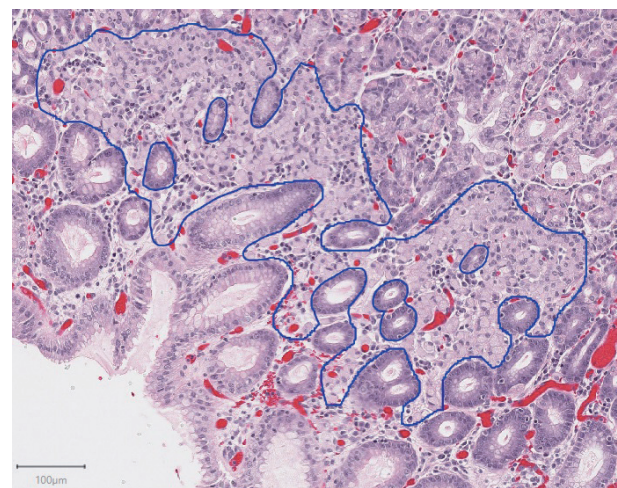


Fig. 1. A representative example of a manually annotated tumor region.

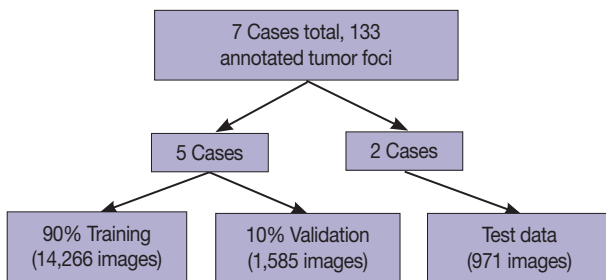


Fig. 2 . Distribution of image patches into training, validation, and test data.

cer. Two cases were identified, with three slides containing carcinoma (out of 110 H&E slides in total). These slides were scanned using the Aperio (Leica Biosystems) scanner at Sunnybrook Health Sciences Centre, and 256×256 pixel patches were extracted in a manner identical to that described above for test cases. This resulted in a total of 814 patches, with 394 of these containing carcinoma.

CNN training

Image patches from the five training cases were randomly divided into training (90%) and validation (10%) sets. A model was trained using DenseNet-169 architecture with compression of 0.5, dropout of 0.2, and bottleneck layers as described in Huang et al. [8]. The model was coded in Python using TensorFlow v1.14.0 [12] with the Keras API. We trained for 100 epochs with stochastic gradient descent at learning rate 0.1, 30 epochs at learning rate 0.01, and 20 epochs at learning rate 0.001. Momentum for batch normalization was set at 0.99. Data was augmented during training with rotations of 0° , 90° , 180° , or 270° . The model was evaluated on the validation images after each epoch and at the end of training to monitor progress and fine tune training parameters. Various learning rate schedules and minor variations on model architecture were applied. In particular, we found that the addition of dropout layers (which are optional in the DenseNet architecture [8]) was useful to reduce overfitting in this relatively small dataset. Only the most successful model based on validation performance was evaluated on the test set.

Training was completed on an NVIDIA GeForce GTX 1060 6GB GPU (Nvidia Corporation, Santa Clara, CA, USA).

Data analysis

The first issue to address was whether the trained model could accurately classify individual image patches. After training on patches from the first five cases, the model was evaluated

on patches extracted from the two test cases. Receiver operating characteristic (ROC) analysis was completed and the area under the curve (AUC) was calculated based on the model's predicted classification on these images compared to ground truth annotations. An identical analysis was conducted on patches extracted from the external validation cases.

The second issue to address was whether the trained model could efficiently analyse whole slide images and identify areas suspicious for carcinoma. We used an approach similar to that described by Liu et al. [5]. Whole slide images from the two test cases were tiled into patches of size 256×256 pixels with 128 pixels of overlap between adjacent patches. The trained model then made a prediction on each patch. In this way, each tumor focus would be analyzed in multiple overlapping patches, so even if one patch resulted in a false-negative, the tumor focus may still be detected in an adjacent/overlapping patch. When a patch was predicted to be positive, the image was rotated 180° and another prediction was made. The final prediction was called positive only if both individual predictions exceeded the threshold value. The threshold value for classifying a patch as positive for carcinoma was chosen based on the value needed to maintain 90% sensitivity for carcinoma patches in the validation dataset. This approach was chosen in an effort to minimize false-positives, while still maintaining adequate sensitivity for individual tumor foci.

Sensitivity was calculated for the whole slide image analysis based on the number of tumor foci that overlapped with at least one patch predicted positive by the model. We also calculated the false-positive rate as a percentage of the non-cancer slide area that was predicted positive by the model.

RESULTS

Our first major objective was to determine whether the trained model could correctly classify individual patches as containing signet ring cell carcinoma or not. To assess this, the trained model was evaluated on patches from the test set, which it had not seen during training. On these images, the trained model achieved an ROC AUC of 0.9986 (Fig. 3). This would permit sensitivity of 95% with a false-positive rate of 0.2%, or a sensitivity of 90% with a false-positive rate of less than 0.1%. Fig. 4 illustrates several examples of correctly classified patches containing signet ring cell carcinoma or normal tissue.

We conducted an identical analysis on the external validation dataset to determine whether the model's performance could be generalized to images from slides stained and scanned at an out-

side institution. On external validation images, the model achieved a similar ROC AUC of 0.9984. This would permit sensitivity of 95% with a false-positive rate of 0.5%, or a sensitivity of 90% with a false-positive rate of less than 0.1%.

Our second major objective was to determine whether the trained model could be used to effectively analyze whole slide images with an acceptable sensitivity and false-positive rate. On 13 whole slide images from the test cases, the sensitivity for tumor patches was 100% (24 out of 24 tumor foci overlapped with at least one patch predicted positive by the model). An example of the model's output following analysis of a whole slide image is illustrated in Fig. 5.

On average, false-positive results accounted for 0.098% of

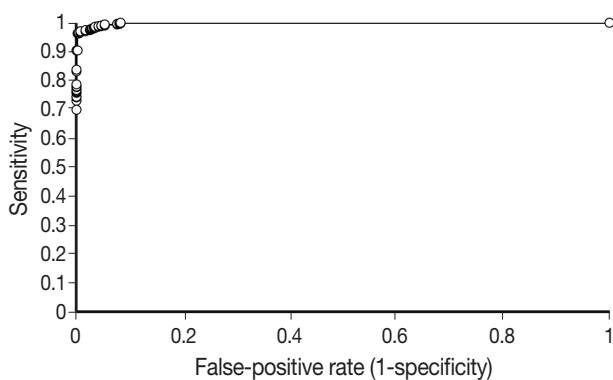


Fig. 3. Receiver operating characteristic curve for classification of individual patches from test data. The area under the curve is 0.9986.

the non-cancer slide area (ranging from 0% to 0.17%). This was equivalent to a mean of 0.53 mm² (approximately 0.14 100× microscope fields) of false-positive area per slide (ranging from 0 to 0.91 mm²). In other words, the model correctly eliminated more than 99.9% of the non-cancer area from whole slide images, while correctly identifying all tumor foci present in the testing data. However, 12 out of 13 whole slide images from the test set had at least one false-positive region.

DISCUSSION

In this study, we created the first dataset of annotated digital histopathology images from patients with hereditary diffuse gastric cancer. We used this data to train a CNN with DenseNet-169 architecture to accurately classify individual patches of cancer versus patches of normal background gastric tissue. The model's performance on this task was consistent when it was evaluated on a small external validation dataset. Additionally, we applied the trained model to the far more difficult problem of analyzing whole slide images from a test set of cases that were not seen during training. On whole slide images, the model identified all tumor foci with a relatively low false-positive rate.

The trained model performed exceptionally well on the classification of individual image patches (including images from our institution and external validation images). Its success on this task suggests that the classification of these patches is usu-

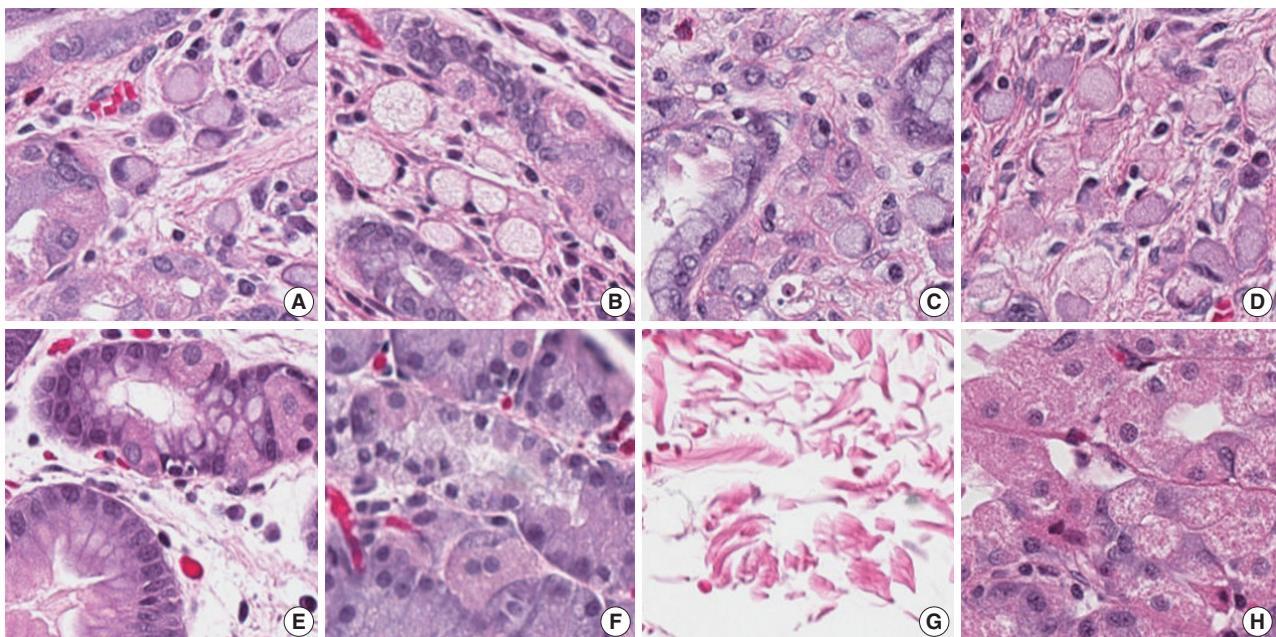


Fig. 4. Examples of 256×256 pixel patches correctly classified as cancer (A–D) or normal (E–H) by the trained model.

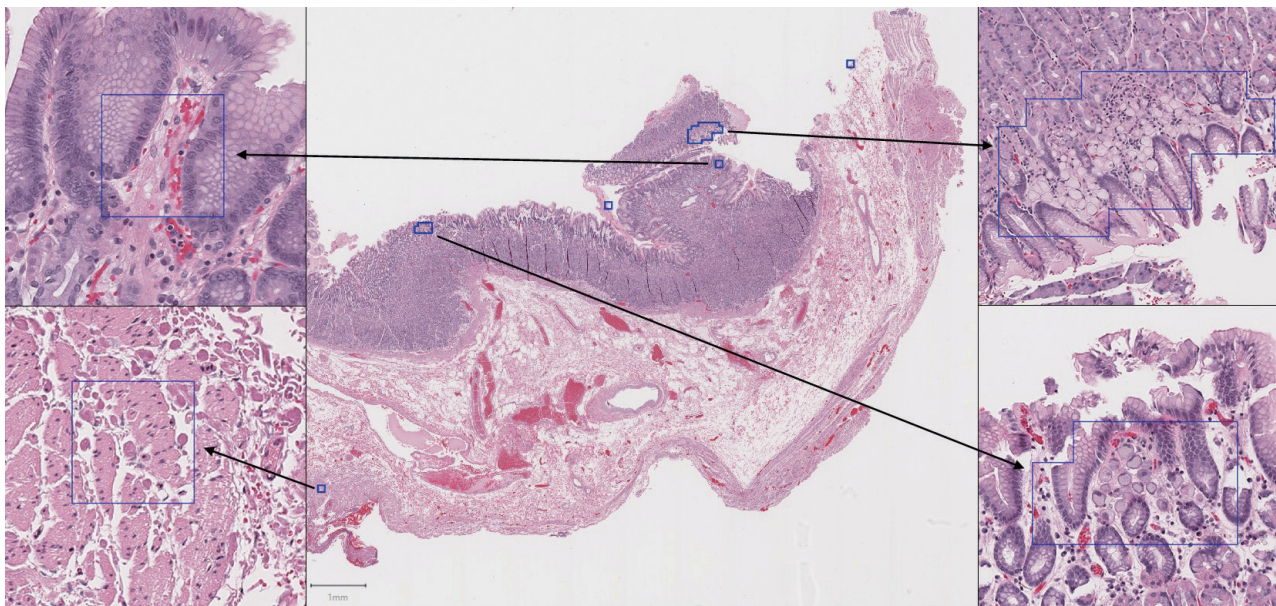


Fig. 5. A portion of a whole slide image analyzed by the trained model. Panels on the right show close ups of correctly identified tumors. Panels on the left show false-positive patches.

ally relatively easy. Any pathologist looking at the images in Fig. 4 would have little trouble determining which contained cancer or normal tissue, and the trained model likewise seems to have little difficulty with this distinction. For a human pathologist, the task becomes much more difficult when foci of cancer are presented in the context of a series of whole slide images from a total gastrectomy. This requires hours of sustained pathologist attention while scanning every part of the sampled tissue on each of hundreds of slides, typically at $100\times$ magnification. Unlike a human, a computer can scan every cell of every slide at $200\times$ magnification with no fatigue or loss of concentration. In our analysis, this resulted in 100% sensitivity for tumor foci.

However, as illustrated in Fig. 5, the trained model has its own set of difficulties when it analyzes a whole slide image. The number of images of normal background tissue in the training dataset is relatively small compared to the number of images of normal tissue encountered when scanning an entire whole slide image. Because a machine learning algorithm can only make predictions based on images that it has encountered during training, it will inevitably encounter areas in a whole slide image that are unlike images it has seen before, and therefore more difficult to classify. Practically, this results in occasional false-positive patches, which were present on almost every slide analyzed. The false-positive results accounted for a small portion of the total slide area, equivalent to an average of 0.14 $100\times$ microscope fields per slide, but these false-positive regions would require

interpretation by a pathologist following automated computer analysis.

A major barrier to the implementation of an automated slide analysis system is the digitization of all relevant slides. This is a time-consuming and expensive process, but some centers have begun to routinely digitize all surgical cases, encouraging pathologists to routinely sign out cases using digital images [13]. Even after digitizing slides, automated analysis itself can be slow, requiring between 1 and 2 hours per slide in the current study. This time could be significantly improved with more powerful hardware, but remains an important consideration when assessing the potential benefits of computer-assisted diagnosis.

Despite the successes of CNN models in pathology, there are significant barriers to their implementation. Effective training requires a large number of images containing the lesion of interest. The most successful studies analyzing whole slide images have used massive training slide datasets to maximize the experience of the model during training and minimize false-positives during testing. For example, Campanella et al. [4] utilized 44,732 whole slide images, representing a dataset many orders of magnitude greater than that used in the current study. While such an approach is undeniably impressive, it is less practical in the case of rare diseases like hereditary diffuse gastric cancer. Furthermore, most approaches require that lesional areas are manually annotated with “ground truth” labels prior to training. This is particularly time consuming in hereditary diffuse

gastric cancer because of the multifocal, poorly circumscribed nature of the lesions. To our knowledge, our dataset currently represents the only fully annotated set of digital images of hereditary diffuse gastric cancer, meaning that approaches requiring larger datasets are not yet feasible.

While the external validation data from the current study suggests that the model may generalize well to image at other institutions, it must be acknowledged that the external validation dataset we used was quite small. This reflects the difficulty of creating usable data for cases of hereditary diffuse gastric cancer, as no large-scale datasets currently exist. The model would undoubtedly benefit from being trained on a larger volume of data generated from several different labs. The current work clearly demonstrates the potential utility of deep learning in the context of hereditary diffuse gastric cancer, and further refinements as additional datasets become available in the future will continue to improve on the baseline we have established here.

It should also be noted that the use of DenseNet-169 architecture in the current study is somewhat arbitrary. While this architecture is well known and compares favorably to other common network architectures in digital pathology [9,10], there is no reason to think that a model using another popular architecture would not be similarly successful. Because accuracy on the current task was so high, a comparison between network architectures would likely not be informative. This is not to suggest that DenseNet is necessarily superior, but only to show that deep learning in general is well suited to addressing the issue of hereditary diffuse gastric cancer.

This model, trained on a relatively small set of images, shows encouraging progress towards computer-assisted diagnosis of hereditary diffuse gastric cancer. The case of hereditary diffuse gastric cancer may represent an ideal example of the value and effectiveness of computer-assisted diagnosis, as the strengths of computers (tirelessly scanning a large number of images) and pathologists (making intelligent decisions when encountering images that they have never encountered previously) complement each other. In an ideal scenario, a trained model could scan every slide from an entire gastrectomy specimen and present the pathologist with only the most suspicious areas, inevitably including some false-positives. Without scanning through hundreds of slides of each case, the pathologist could then focus their attention on high power images of only the most suspicious areas in order to determine whether cancer was present or whether additional investigations (for example, deeper levels or special stains) were required. Determining whether such a cooperative effort can in fact improve efficiency or accuracy will be the sub-

ject of future research.

Ethics Statement

Data collection and research methods were approved by the relevant research ethics boards (Nova Scotia Health Authority Research Ethics Board #1024339, Sunnybrook Health Sciences Centre Research Ethics Board #3152). Because no identifying information was collected, the requirement for informed consent was waived by the research ethics boards.

ORCID

Sean A. Rasmussen <https://orcid.org/0000-0002-3231-0404>
Thomas Arnason <https://orcid.org/0000-0001-5038-6202>

Author Contributions

Conceptualization: SAR, TA, WYH. Data curation: SAR, TA, WYH. Formal analysis: SAR. Funding acquisition: SAR, WYH. Investigation: SAR, TA, WYH. Methodology: SAR, TA, WYH. Project administration: TA, WYH. Resources: SAR, TA, WYH. Software: SAR. Supervision: TA, WYH. Validation: SAR. Visualization: SAR, TA, WYH. Writing – original draft: SAR. Writing – review & editing: SAR, TA, WYH. Approval of final manuscript: SAR, TA, WYH. Approval of final manuscript: all authors.

Conflicts of Interest

The authors declare that they have no potential conflicts of interest.

Funding Statement

This work was supported by funding from the Nova Scotia Health Authority Research Fund.

References

1. van der Post RS, Vogelaar IP, Carneiro F, et al. Hereditary diffuse gastric cancer: updated clinical guidelines with an emphasis on germline *CDH1* mutation carriers. *J Med Genet* 2015; 52: 361-74.
2. Rajpurkar P, Irvin J, Zhu K, et al. CheXnet: radiologist-level pneumonia detection on chest X-rays with deep learning. Preprint at: <https://arxiv.org/abs/1711.05225> (2017).
3. Gulshan V, Peng L, Coram M, et al. Development and validation of a deep learning algorithm for detection of diabetic retinopathy in retinal fundus photographs. *JAMA* 2016; 316: 2402-10.
4. Campanella G, Hanna MG, Geneslaw L, et al. Clinical-grade computational pathology using weakly supervised deep learning on whole slide images. *Nat Med* 2019; 25: 1301-9.
5. Liu Y, Gadepalli K, Norouzi M, et al. Detecting cancer metastases on gigapixel pathology images. Preprint at: <https://arxiv.org/abs/1703.02442> (2017).
6. Li C, Wang X, Liu W, Latecki LJ. DeepMitosis: mitosis detection via deep detection, verification and segmentation networks. *Med Image Anal* 2018; 45: 121-33.
7. Steiner DF, MacDonald R, Liu Y, et al. Impact of deep learning assistance on the histopathologic review of lymph nodes for metastatic breast cancer. *Am J Surg Pathol* 2018; 42: 1636-46.
8. Huang G, Liu Z, Van Der Maaten L, Weinberger KQ. Densely connected convolutional networks. *Proc IEEE Comput Soc Conf Comput Vis Pattern Recognit* 2017; 2017: 4700-8.
9. Bianco S, Cadene R, Celona L, Napoletano P. Benchmark analysis of representative deep neural network architectures. *IEEE Access* 2018; 6: 64270-7.
10. Mormont R, Geurts P, Maree R. Comparison of deep transfer

- learning strategies for digital pathology. Proc Comput Soc IEEE Conf Comput Vis Pattern Recognit 2018; 2018: 2375-84.
11. Bankhead P, Loughrey MB, Fernandez JA, et al. QuPath: Open source software for digital pathology image analysis. Sci Rep 2017; 7: 16878.
 12. Abadi M, Agarwal A, Barham P, et al. Tensorflow: large-scale machine learning on heterogeneous distributed systems [Internet]. Mountain View: TensorFlow, 2015 [cited 2020 Jun 9]. Available from: <http://tensorflow.org>.
 13. Hanna MG, Reuter VE, Samboy J, et al. Implementation of digital pathology offers clinical and operational increase in efficiency and cost savings. Arch Pathol Lab Med 2019; 143: 1545-55.

MicroRNA-552 expression in colorectal cancer and its clinicopathological significance

Joon Im¹, Soo Kyung Nam², Hye Seung Lee²

¹Department of Pathology, Seoul National University Bundang Hospital, Seongnam;

²Department of Pathology, Seoul National University Hospital, Seoul National University College of Medicine, Seoul, Korea

Background: MicroRNA-552 (miR-552) has been reported to correlate with the development and progression of various cancers, including colorectal cancer (CRC). This study aimed to investigate miR-552 expression in cancer tissue samples compared to normal mucosal tissue and its role as a diagnostic or prognostic marker in CRC patients. **Methods:** Normal mucosal tissues and primary cancer tissues from 80 surgically resected CRC specimens were used. Quantitative real-time polymerase chain reaction was performed for miR-552 and U6 small nuclear RNA to analyze miR-552 expression and its clinicopathological significance. Immunohistochemistry for p53 and phosphatase and tension homolog (PTEN) was performed to evaluate their association with miR-552 expression. **Results:** miR-552 expression was significantly higher in primary cancer tissues compared to normal mucosal tissues ($p < .001$). The expression level of miR-552 was inversely correlated with that of PTEN ($p = .068$) and p53 ($p = .004$). Survival analysis showed that high miR-552 expression was associated with worse prognosis but this was not statistically significant ($p = .255$). However, patients with CRC having high miR-552 expression and loss of PTEN expression had significantly worse prognosis than others ($p = .029$). **Conclusions:** Our results suggest that high miR-552 expression might be a potential diagnostic biomarker for CRC, and its combined analysis with PTEN expression can possibly be used as a prognostic marker.

Key Words: miR-552; Colorectal neoplasms; p53; PTEN; Prognosis

Received: November 13, 2020 **Revised:** January 6, 2021 **Accepted:** January 17, 2021

Corresponding Author: Hye Seung Lee, MD, PhD, Department of Pathology, Seoul National University Hospital, Seoul National University College of Medicine, 103 Daehak-ro, Jongno-gu, Seoul 03080, Korea

Tel: +82-2-740-8269, Fax: +82-2-765-5600, E-mail: hye2@snu.ac.kr

Colorectal cancer (CRC) is a disease with a high mortality rate affected by metastasis to other organs. The incidence of CRC has increased worldwide, making it the third most common cancer, next only to lung and breast cancers. Its mortality rate ranks second globally [1]. In South Korea, CRC is the second most common type of cancer after stomach cancer, caused by a westernized dietary pattern [2]. Moreover, its mortality rate has been rapidly increasing.

Previous studies on the mechanism of colorectal carcinogenesis have demonstrated the potential of microRNAs (miRNAs) as prognostic and diagnostic markers [3-5]. miRNAs are small non-coding, single-stranded RNA molecules consisting of 19–25 nucleotides capable of controlling hundreds of target genes [6,7]. A miRNA either disassembles the mRNA or hinders its translation to protein, preventing protein expression [8]. RNase III Dicer disassembles pre-miRNA into a mature double-stranded

miRNA of approximately 22 nucleotides; thereafter, it combines with the RNA-induced silencing complex, splitting the mRNA itself or preventing mRNA transcription [9]. miRNAs are also involved in the activity of over 50% of human genes by affecting gene expression and dysregulation, which prevents the formation and progression of tumors. Therefore, miRNAs are involved in formation or progression of various cancers [10]. For example, miRNA are major regulators of the Wnt/ β -catenin signaling pathway during cell proliferation and survival [11-13]. Previous studies suggest that there are changes in miRNA expression in various cancer cells compared to normal cells [14-16]. Therefore, alterations in miRNA expression can be used for cancer diagnosis [17,18].

Previous studies have shown that miR-552 is involved in the carcinogenesis, progression, and metastasis of CRC [19-22]. It has been reported that miR-552 promotes the proliferation and

invasion of CRC cells by directly targeting DACH1 through the Wnt/ β -catenin signaling pathways [23]. miR-552 has been shown to activate the Wnt/ β -catenin signaling pathway to regulate the expression of the tumor suppressors p53 and phosphatase and tension homolog (PTEN) [22,24]. However, the correlation of miR-552 expression and its clinicopathological significance in CRC patients has not been investigated much.

This study aimed to verify the diagnostic and prognostic roles of miR-552 expression in patients with CRC. In this study, miR-552 expression was investigated via quantitative real-time reverse transcription polymerase chain reaction (qRT-PCR) and analyzed for an association with clinicopathological features. Moreover, immunohistochemistry (IHC) for p53 and PTEN was conducted to confirm the association with miR-552.

MATERIALS AND METHODS

Patients and samples

A total of 80 patients with CRC were enrolled for this study. Normal mucosal tissues and primary cancer tissues were collected from the CRC patients who underwent surgical resection at Seoul National University Bundang Hospital. The histopathological differentiation was classified according to the World Health Organization standards (5th edition) [25], and pTNM was classified according to the American Joint Committee on Cancer (8th edition) [26]. The clinicopathological characteristics of each patient including sex, age, location, tumor size, and presence of lymphatic invasion were obtained from medical charts and pathology reports. The patients were followed up from the date of surgery either to the date of death or to the date of last follow-up.

Tissue microarray

The specimens of patients with CRC who underwent surgical resection were collected from the formalin-fixed-paraffin-embedded (FFPE) tissue. In each case, a 2 mm core sample was obtained from the tumor area, and the samples from 80 patients were arranged into two tissue microarray (TMA) blocks.

miRNA isolation

The RecoverALL Total Nucleic Acid Isolation Kit (Life Technologies, Carlsbad, CA, USA) was used to extract total RNA from the FFPE tissues. RNA extraction was performed as per the manufacturer's manual. The purity and quantity of the extracted RNA were measured using a NanoDrop 2000/2000c spectrophotometer (Thermo Fisher Scientific, Wilmington, DE, USA).

cDNA synthesis

cDNA synthesis was performed on 10 ng of RNA from each sample using the TaqMan MicroRNA Reverse Transcript Kit (Applied Biosystems, Foster City, CA, USA). cDNA was synthesized using a C1000 Touch Thermal Cycler (Bio-Rad, Laboratories, Foster City, CA, USA) with the following cycle: 16°C for 30 minutes, 42°C for 30 minutes, and 85°C for 5 minutes.

qRT-PCR

The TaqMan small RNA assay kit (ABI, Applied Biosystems) was used to quantify miR-552, following the manufacturer's instruction. qRT-PCR was conducted on the synthesized cDNA, to evaluate miRNA expression, with the following cycle: 95°C for 10 minutes, 95°C for 15 seconds, and 60°C for 1 minute. U6 small nuclear RNA was used as the standardized control for the target miRNA, miR-552.

qRT-PCR was performed to obtain the average value for quantifying the expression. Each value of the threshold cycle value (Ct value), obtained based on U6 expression was standardized and analyzed by a relative quantification method. U6 was used as the internal miRNA control, and the Δ Ct (to compare normal and tumor tissues) and $\Delta\Delta$ Ct values were calculated. The fold change of the gene was calculated using the estimated $2^{-\Delta\Delta C_t}$ [27].

IHC

IHC for p53 (1:1,000, clone DO-7, DAKO, Santa Clara, CA, USA) and PTEN (1:1,000, clone Y184, Abcam, Cambridge, UK) was performed on 3- μ m-thick sections from the TMA block using a Ventana automated immunostainer (BenchMark XT, Ventana Medical Systems, Tucson, AZ, USA), in accordance with the manufacturer's instructions. IHC was interpreted by intensity (negative, weak, and strong) and area (%). The PTEN and p53 expression were classified into three categories: (1) strong staining in $\geq 10\%$ of the tumor cells was considered as strong positive, (2) samples without any nuclear staining of tumor cells were interpreted as negative, and (3) samples exhibiting weak staining in any area or patchy strong staining in $< 10\%$ of tumor cells were regarded as weakly positive [28].

Statistical analysis

The miR-552 expression change was indicated by the median with range. High and low miR-552 subgroups were classified according to miR-552 expression levels with a cut-off of the median value [29]. Wilcoxon matched-pairs signed rank test was used to compare the miR-552 manifestations of the two groups,

and the Kruskal-Wallis test was used to compare TNM stage sequential trends. For comparison of variables via category on clinical findings, the chi square or Fisher exact test was used. Kaplan-Meier curves with log-rank test were used for survival analysis. The Cox proportional hazards model was used for univariate and multivariate regression analyses. Linear-by-linear association analysis was used to compare miR-552 with p53, and PTEN expression patterns. PASW ver. 18.0 (IBM Co., Armonk, NY, USA) was used for statistical analysis. A p-value < .05 was considered statistically significant.

RESULTS

Expression of miR-552 in CRC tissue

Primary cancer tissues and matched normal mucosal tissues were used to investigate the expression levels of miR-552 in patients with CRC. The relative expression value of miR-552 was identified based on the internal control of U6. The expression of miR-552 was approximately four times higher in primary cancer tissues than normal mucosal tissues; this was statistically significant ($p < .001$) (Fig. 1A).

Relationship between the clinicopathological characteristics of CRC and miR-552 expression

qRT-PCR results showed that miR-552 expression increased in the primary cancer tissue of patients with CRC. Based on these results, the correlation with clinicopathological characteristics was analyzed by dividing the cases into low and high miR-552 subgroups based on the median of the miR-552 $\Delta\Delta Ct$ values (Table 1). Clinicopathological characteristics such as age, sex, tumor location, histologic grade, tumor size, pT, pN, M, pTNM stage, and venous invasion were compared with the miR-552 expression status. The miR-552 high expression group tended to be male,

located in the right colon (ascending to transverse colon), have a low histologic grade, and be of advanced stage, but without statistical significance ($p > .05$).

Table 1. Correlation between the clinicopathological characteristics of patients with colorectal cancer and miR-552 expression

Variable	miR-552 expression		Total	p-value
	Low	High		
Age (yr)	72.00 (37–96)	74.00 (44–97)	72.00 (37–97)	.616
Sex				.369
Male	20 (50.0)	24 (60.0)	44 (55.0)	
Female	20 (50.0)	16 (40.0)	36 (45.0)	
Tumor location				.576
Right	7 (17.5)	9 (22.5)	16 (20.0)	
Left	33 (82.5)	31 (77.5)	64 (80.0)	
Histologic grade				.675
Low grade	36 (90.0)	38 (95.0)	74 (92.5)	
High grade	4 (10.0)	2 (5.0)	6 (7.5)	
Tumor size	4.25 (0.9–9.0)	4.75 (1.8–10.0)	4.50 (0.9–10.0)	.505
pT				.189
pT1–2	12 (30.0)	7 (17.5)	19 (23.8)	
pT3–4	28 (70.0)	33 (82.5)	61 (76.3)	
pN				.056
pN0–1	35 (87.5)	28 (70.0)	63 (78.8)	
pN2	5 (12.5)	12 (30.0)	17 (21.3)	
M				.204
M0	32 (80.0)	27 (67.5)	59 (73.8)	
M1	8 (20.0)	13 (32.5)	21 (26.3)	
pTNM				.128
I	11 (27.5)	5 (12.5)	16 (20.0)	
II	5 (12.5)	10 (25.0)	15 (18.8)	
III	16 (40.0)	12 (30.0)	28 (35.0)	
IV	8 (20.0)	13 (32.5)	21 (26.3)	
Venous invasion				> .99
No	28 (70.0)	28 (70.0)	56 (70.0)	
Yes	12 (30.0)	12 (30.0)	24 (30.0)	
Total	40	40	80	

Values are presented as median (range) or number (%).
miR-552, microRNA-552.

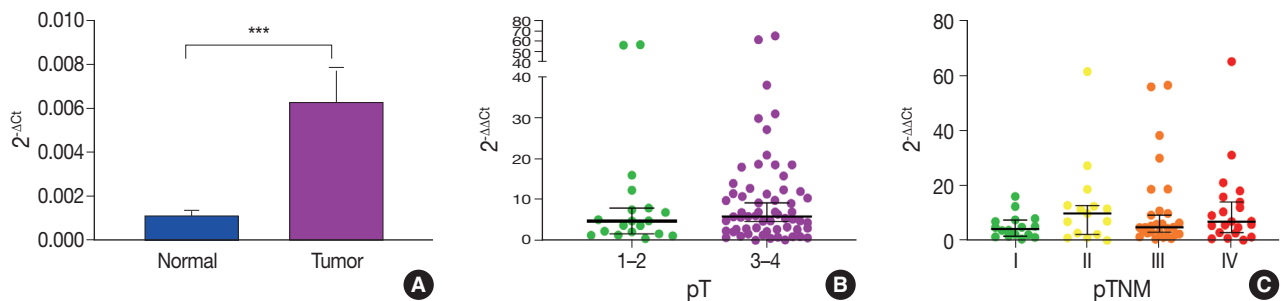


Fig. 1. The expression level of miR-552 in the patients with colorectal cancer. (A) Comparative analysis of microRNA-552 (miR-552) expression in normal mucosal tissues (normal) and primary cancer tissues (tumor) in 80 patients with colorectal cancer using quantitative real-time reverse transcription polymerase chain reaction (by Wilcoxon matched-pairs signed rank test, $***p < .001$). (B) miR-552 expression is relevant according to pT stages (Mann Whitney test; $p = .393$). (C) miR-552 expression is relevant according to pTNM stages (Kruskal-Wallis test, $p = .414$).

When the median miR-552 values were compared according to pT and pTNM stage (Fig. 1B, C), the expression of miR-552 was higher in pT3–4 than pT1–2, and higher in stage II–IV than stage I, but the difference was not statistically significant ($p = .393$ and $p = .414$, respectively).

Relationship between miR-552 expression status and PTEN and p53 protein expression

IHC was performed to determine the expression of p53 and PTEN proteins (Fig. 2) and the association with the miR-552 expression pattern was analyzed and compared. Negative expres-

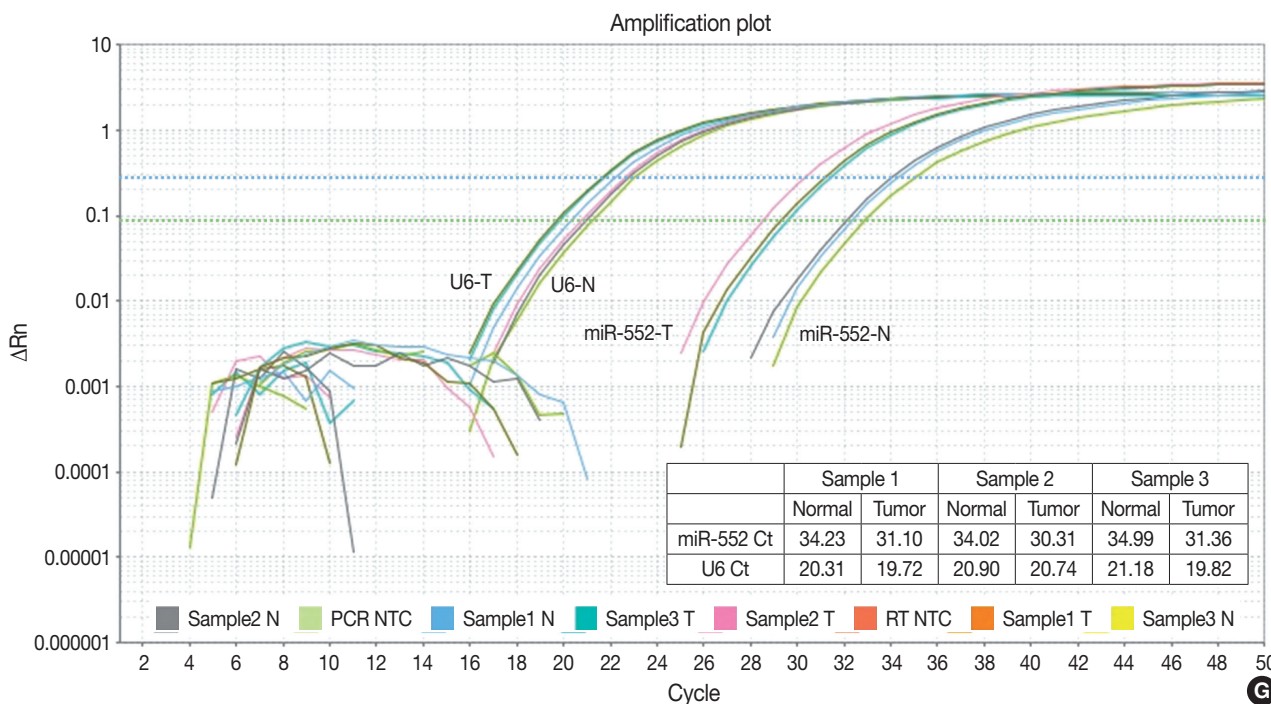
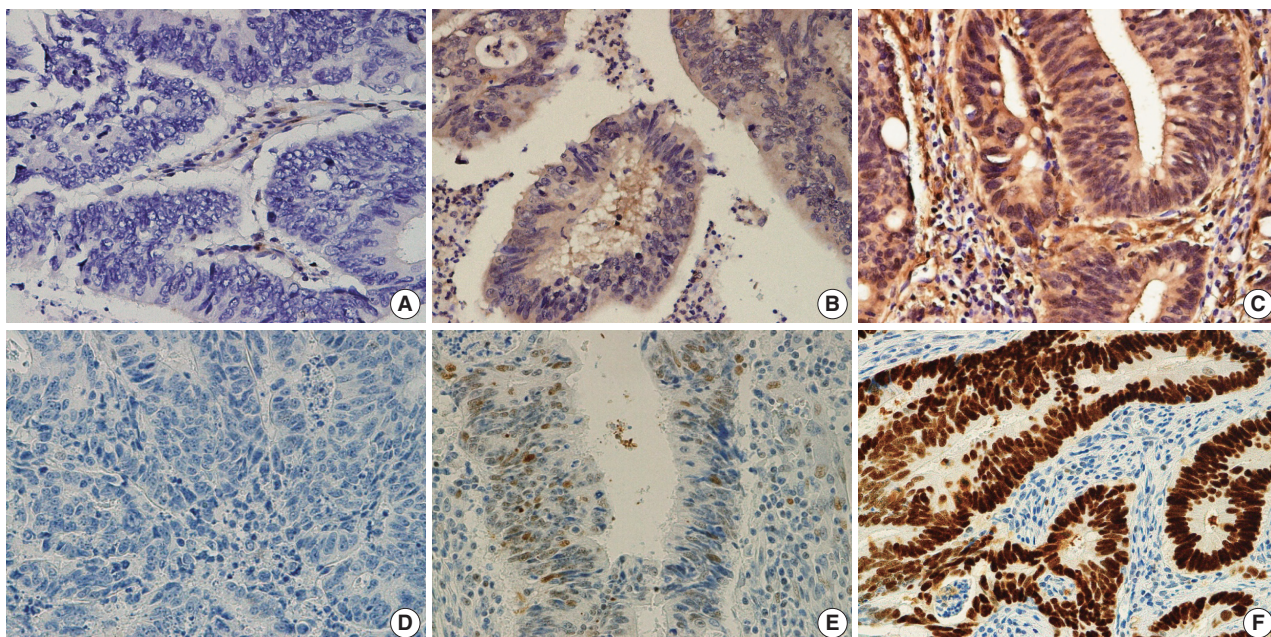


Fig. 2. Immunohistochemical staining of phosphatase and tension homolog (PTEN) and p53 expression in patients with colorectal cancer: (A) negative staining of PTEN, (B) weak positive staining of PTEN, (C) positive staining of PTEN, (D) negative staining of p53, (E) weak positive staining of p53, and (F) positive staining of p53. (G) Representative amplification curves of microRNA-552 (miR-552) and U6 by real-time polymerase chain reaction (PCR) methods. NTC, no template control.

sion of PTEN and p53 was more frequently found in the high miR-552 subgroup than in low subgroup ($p = .068$ and $p = .004$, respectively) (Table 2).

Prognostic significance of miR-552 expression

Our study showed that miR-552 was upregulated in cancer tissue when compared with normal tissue in patients with CRC. Thereafter, we performed univariate and multivariate survival analyses according to the miR-552 expression status. Kaplan-Meier survival curves showed that the miR-552 high subgroup was associated with worse prognosis, but this was not statistically sig-

nificant ($p = .255$) (Fig. 3A). However, the miR-552 high and PTEN-negative subgroup had significantly worse outcome than the other subgroups ($p = .029$) (Fig. 3B). When multivariable Cox regression analysis was performed with pTNM stage and age, high miR-552 and PTEN-negative subgroup had a tendency of worse prognosis, but with borderline statistical significance ($p = .077$) (Supplementary Table S1).

DISCUSSION

The incidence of CRC is increasing every year. However, early diagnosis is difficult and the disease has a high mortality rate due to metastasis. Many recent studies have suggested altered expression of miRNAs in various cancers. For CRCs, researchers investigated how miRNAs contribute to carcinogenesis and regulate the invasion and metastasis of cancer during disease progression. miR-552, one of the miRNAs whose expression is altered in different types of cancers, has been found to be related to colorectal, ovarian, breast, liver, and pancreatic cancers [23,24,30-32]. In this study, the expression of miR-552 in normal mucosa and primary cancer tissue and the association with clinicopathological characteristics of patients with CRC were analyzed. The results showed that miR-552 in CRC showed an increased expression in primary cancer tissue compared to normal mucosal tissue. This is in accordance with the results of previous studies [19,33].

Table 2. The relationship between PTEN and p53 protein expression by immunohistochemistry and miR-552 expression (linear-by-linear association)

	miR-552 expression		Total	p-value
	Low	High		
PTEN				.068
Negative	3 (7.7)	7 (17.5)	10 (12.7)	
Weak	13 (33.3)	17 (42.5)	30 (38.0)	
Positive	23 (59.0)	16 (40.0)	39 (49.4)	
p53				.004
Negative	3 (7.7)	14 (35.0)	17 (21.5)	
Weak	3 (7.7)	3 (7.5)	6 (7.6)	
Positive	33 (84.6)	23 (57.5)	56 (70.9)	
Total	39	40	79	

PTEN, phosphatase and tension homolog; miR-552, microRNA-552.

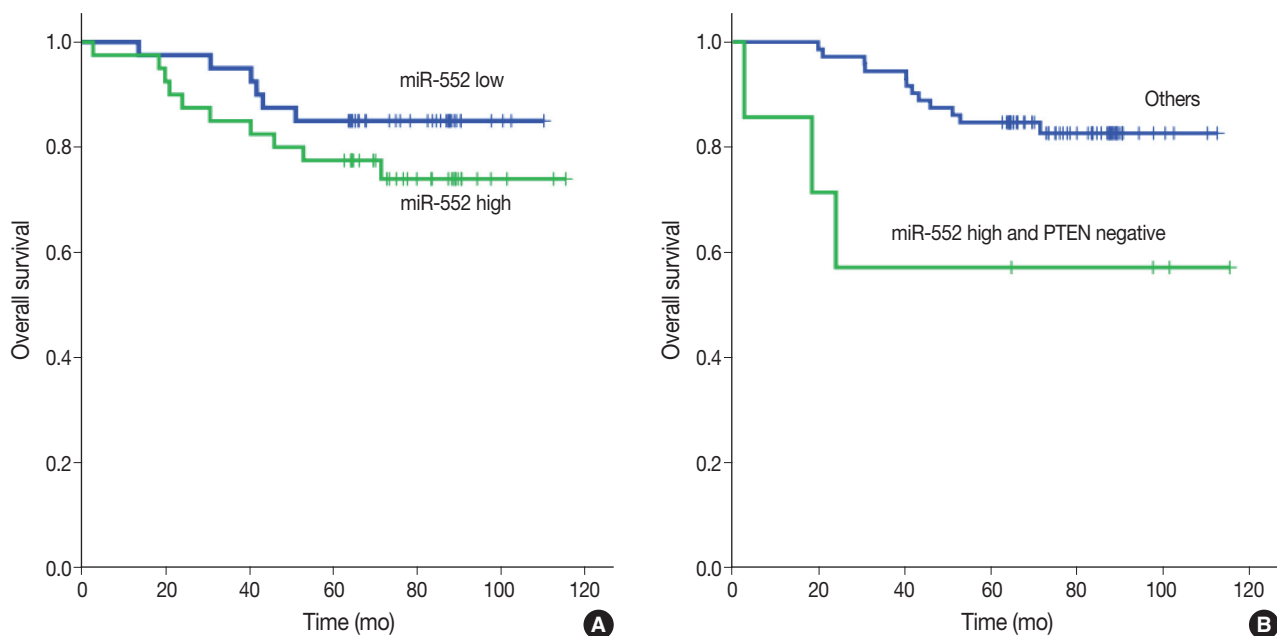


Fig. 3. Kaplan-Meier univariate survival analysis according microRNA-552 (miR-552) and phosphatase and tension homolog (PTEN) expression status in patients with colorectal cancer. (A) miR-552 high group has worse prognosis than low group, but is not statistically significant ($p = .255$). (B) miR-552 high and PTEN-negative group is significantly associated with poor prognosis when compared to others ($p = .029$).

We determined the association between miR-552 and the tumor suppressor genes, PTEN and p53. PTEN catalyzes the dephosphorylation of phosphatidylinositol 3,4,5-trisphosphate (PIP3) [34]. Loss of PTEN function increases PIP3 activity and activates the phosphoinositide 3-kinase/protein kinase B (PKB or AKT; hereafter referred to as AKT) signaling pathway to promote cell growth, proliferation, and survival [35,36]. The protein phosphatase activity of PTEN is involved in regulating the cell cycle, preventing cells from growing or splitting too quickly [24,37]. p53 expression rapidly increases when DNA damage occurs in cells, leading to the expression of DNA repairing enzymes to allow cells to survive, or the expression of BCL-2-associated X protein and p53 upregulated modulator of apoptosis, which induce cell death, causing damaged cells to die on their own [22,38,39]. Abnormalities in PTEN and p53 expression promote cancer development by inducing cell cycle, reducing apoptosis, and decreasing genomic stability. Previous in vivo studies have shown that the 3'-untranslated region of *PTEN* and *p53* mRNA has a potential miR-552 binding site and the two molecules interact, suggesting that miR-552 could regulate the expression of PTEN and p53 [22,24,40,41]. miR-552 directly targets PTEN and p53, reducing PTEN and p53 expression levels when miR-552 is overexpressed [22,24,40]. Our results also revealed frequent loss of PTEN expression or p53 negative expansion in the high miR-552 subgroup using clinical samples of CRC.

miR-552 had a tendency of increased expression in advanced pT or pTNM stage, but without statistical significance. In addition, the high miR-552 subgroup did not have a statistically significant worse prognosis. However, the high miR-552 subgroup with PTEN loss showed a statistically significant worse prognosis. It is suggested that the combined status of miRNAs and their target proteins may be more clinically significant than the miRNAs themselves. Further studies are needed to clarify it.

An analysis of the correlation between clinicopathological characteristics and miR-552 expression in patients with CRC showed that the expression of miR-552 was high regardless of age, sex, and tumor location (Table 1). However, a few previous studies have shown that high miR-552 expression in CRC and other cancers was correlated with aggressive clinicopathological factors, such as higher histologic grade, lymph node metastasis, and advanced TNM stage [19,33]. A potential reason why the results of our study differ from those of the previous studies could be the small sample size of our study. Therefore, a large multicenter study would be necessary in the future. In addition to cancer tissues of patients with CRC, miR-552 expression sta-

tus in other tissues such as blood may be helpful for early diagnosis and detection of cancer recurrence.

miRNAs are expressed directly in cancer cells, or in cancer microenvironment such as cancer-associated fibroblasts (CAFs) and various tumor-infiltrating immune cells. miR-21 expression in CAFs was reported in CRC tissue using the in situ hybridization method [42]. Previous studies have reported that miR-552 expression increased in various cancer tissues and cell-lines including CRC, hepatocellular carcinoma, osteosarcoma, ovarian cancer, gastric cancer, pancreas cancer, and lung cancer, suggesting the possible expression of miR-552 in cancer cells. However, our results could not demonstrate which cells expressed miR-552 because we used the real-time PCR. Further studies are needed to reveal the source of miR-552 expression.

The results of this study suggest that increased miR-552 expression can be used as a diagnostic biomarker in patients with CRC and that the combined analysis with PTEN expression may be used as a prognostic marker, which can help diagnose and treat patients with CRC in the future.

Supplementary Information

The Data Supplement is available with this article at <https://doi.org/10.4132/jptm.2021.01.17>.

Ethics Statement

This study was by the Institutional Review Board of Seoul National University Bundang Hospital (B-1012/117-011). Informed consent was obtained from all individual participants included in the study.

ORCID

Joon Im <https://orcid.org/0000-0001-7204-6364>
 Soo Kyung Nam <https://orcid.org/0000-0002-4372-1516>
 Hye Seung Lee <https://orcid.org/0000-0002-1667-7986>

Author Contributions

Conceptualization: HSL. Funding Acquisition: HSL. Investigation: JI, SKN. Methodology: JI, SKN. Supervision: HSL. Writing—original draft: JI, HSL. Writing—review & editing: JI, SKN, HSL. Approval of final manuscript: all authors.

Conflicts of Interest

H.S.L., a contributing editor of the Journal of Pathology and Translational Medicine, were not involved in the editorial evaluation or decision to publish this article. All remaining authors have declared no conflicts of interest.

Funding Statement

This work was supported by the Seoul National University Foundation (800-20190384).

References

1. Bray F, Ferlay J, Soerjomataram I, Siegel RL, Torre LA, Jemal A. Global cancer statistics 2018: GLOBOCAN estimates of incidence and mortality worldwide for 36 cancers in 185 countries. *CA Can-*

- cer J Clin 2018; 68: 394-424.
2. Hong S, Won YJ, Park YR, et al. Cancer statistics in Korea: incidence, mortality, survival, and prevalence in 2017. *Cancer Res Treat* 2020; 52: 335-50.
 3. Markowitz SD, Bertagnolli MM. Molecular origins of cancer: Molecular basis of colorectal cancer. *N Engl J Med* 2009; 361: 2449-60.
 4. Luo X, Burwinkel B, Tao S, Brenner H. MicroRNA signatures: novel biomarker for colorectal cancer? *Cancer Epidemiol Biomarkers Prev* 2011; 20: 1272-86.
 5. Koga Y, Yasunaga M, Takahashi A, et al. MicroRNA expression profiling of exfoliated colonocytes isolated from feces for colorectal cancer screening. *Cancer Prev Res (Phila)* 2010; 3: 1435-42.
 6. Krek A, Grun D, Poy MN, et al. Combinatorial microRNA target predictions. *Nat Genet* 2005; 37: 495-500.
 7. Lee RC, Feinbaum RL, Ambros V. The *C. elegans* heterochronic gene *lin-4* encodes small RNAs with antisense complementarity to *lin-14*. *Cell* 1993; 75: 843-54.
 8. Bartel DP. MicroRNAs: genomics, biogenesis, mechanism, and function. *Cell* 2004; 116: 281-97.
 9. Jeffrey SS. Cancer biomarker profiling with microRNAs. *Nat Biotechnol* 2008; 26: 400-1.
 10. Calin GA, Sevignani C, Dumitru CD, et al. Human microRNA genes are frequently located at fragile sites and genomic regions involved in cancers. *Proc Natl Acad Sci U S A* 2004; 101: 2999-3004.
 11. Ji J, Yamashita T, Wang XW. Wnt/beta-catenin signaling activates microRNA-181 expression in hepatocellular carcinoma. *Cell Biosci* 2011; 1: 4.
 12. Kim NH, Kim HS, Kim NG, et al. p53 and microRNA-34 are suppressors of canonical Wnt signaling. *Sci Signal* 2011; 4: ra71.
 13. Cai J, Guan H, Fang L, et al. MicroRNA-374a activates Wnt/beta-catenin signaling to promote breast cancer metastasis. *J Clin Invest* 2013; 123: 566-79.
 14. Calin GA, Croce CM. MicroRNA signatures in human cancers. *Nat Rev Cancer* 2006; 6: 857-66.
 15. Lu J, Getz G, Miska EA, et al. MicroRNA expression profiles classify human cancers. *Nature* 2005; 435: 834-8.
 16. Volinia S, Calin GA, Liu CG, et al. A microRNA expression signature of human solid tumors defines cancer gene targets. *Proc Natl Acad Sci U S A* 2006; 103: 2257-61.
 17. Calin GA, Croce CM. MicroRNA-cancer connection: the beginning of a new tale. *Cancer Res* 2006; 66: 7390-4.
 18. Hayes J, Peruzzi PP, Lawler S. MicroRNAs in cancer: biomarkers, functions and therapy. *Trends Mol Med* 2014; 20: 460-9.
 19. Wang N, Liu W. Increased expression of miR-552 acts as a potential predictor biomarker for poor prognosis of colorectal cancer. *Eur Rev Med Pharmacol Sci* 2018; 22: 412-6.
 20. Xia ZS, Wang L, Yu T, et al. MiR-5000-3p, miR-5009-3P and miR-552: potential microRNA biomarkers of side population cells in colon cancer. *Oncol Rep* 2014; 32: 589-96.
 21. Oberg AL, French AJ, Sarver AL, et al. miRNA expression in colon polyps provides evidence for a multihit model of colon cancer. *PLoS One* 2011; 6: e20465.
 22. Kwak B, Kim DU, Kim TO, Kim HS, Kim SW. MicroRNA-552 links Wnt signaling to p53 tumor suppressor in colorectal cancer. *Int J Oncol* 2018; 53: 1800-8.
 23. Cao J, Yan XR, Liu T, et al. MicroRNA-552 promotes tumor cell proliferation and migration by directly targeting DACH1 via the Wnt/beta-catenin signaling pathway in colorectal cancer. *Oncol Lett* 2017; 14: 3795-802.
 24. Zhao W, Han T, Li B, Ma Q, Yang P, Li H. miR-552 promotes ovarian cancer progression by regulating PTEN pathway. *J Ovarian Res* 2019; 12: 121.
 25. Nagtegaal ID, Odze RD, Klimstra D, et al. The 2019 WHO classification of tumours of the digestive system. *Histopathology* 2020; 76: 182-8.
 26. Weiser MR. AJCC 8th Edition: Colorectal Cancer. *Ann Surg Oncol* 2018; 25: 1454-5.
 27. Schmittgen TD, Livak KJ. Analyzing real-time PCR data by the comparative C(T) method. *Nat Protoc* 2008; 3: 1101-8.
 28. Hwang HJ, Nam SK, Park H, et al. Prediction of TP53 mutations by p53 immunohistochemistry and their prognostic significance in gastric cancer. *J Pathol Transl Med* 2020; 54: 378-86.
 29. Tong F, Ying Y, Pan H, Zhao W, Li H, Zhan X. MicroRNA-466 (miR-466) functions as a tumor suppressor and prognostic factor in colorectal cancer (CRC). *Bosn J Basic Med Sci* 2018; 18: 252-9.
 30. Kim HK, Lim NJ, Jang SG, Lee GK. miR-592 and miR-552 can distinguish between primary lung adenocarcinoma and colorectal cancer metastases in the lung. *Anticancer Res* 2014; 34: 2297-302.
 31. Qu W, Wen X, Su K, Gou W. MiR-552 promotes the proliferation, migration and EMT of hepatocellular carcinoma cells by inhibiting AJAP1 expression. *J Cell Mol Med* 2019; 23: 1541-52.
 32. Chen T, Lei S, Zeng Z, et al. Linc00261 inhibits metastasis and the WNT signaling pathway of pancreatic cancer by regulating a miR-5525p/FOXO3 axis. *Oncol Rep* 2020; 43: 930-42.
 33. Li C, Wang Z, Chen S, Zhang J, Qu K, Liu C. MicroRNA-552 promotes hepatocellular carcinoma progression by downregulating WIF1. *Int J Mol Med* 2018; 42: 3309-17.
 34. Maehama T, Dixon JE. The tumor suppressor, PTEN/MMAC1, dephosphorylates the lipid second messenger, phosphatidylinositol 3,4,5-trisphosphate. *J Biol Chem* 1998; 273: 13375-8.
 35. Xiong B, Cheng Y, Ma L, Zhang C. MiR-21 regulates biological behavior through the PTEN/PI-3 K/Akt signaling pathway in human colorectal cancer cells. *Int J Oncol* 2013; 42: 219-28.
 36. Vivanco I, Sawyers CL. The phosphatidylinositol 3-Kinase AKT pathway in human cancer. *Nat Rev Cancer* 2002; 2: 489-501.
 37. Brandmaier A, Hou SQ, Shen WH. Cell cycle control by PTEN. *J Mol Biol* 2017; 429: 2265-77.
 38. Miyashita T, Reed JC. Tumor suppressor p53 is a direct transcriptional activator of the human bax gene. *Cell* 1995; 80: 293-9.
 39. Somasundaram K. Tumor suppressor p53: regulation and function. *Front Biosci* 2000; 5: D424-37.
 40. Han T, Zhang Y, Yang X, et al. miR-552 regulates liver tumor-initiating cell expansion and sorafenib resistance. *Mol Ther Nucleic Acids* 2020; 19: 1073-85.
 41. Bi X, Lv X, Liu D, et al. METTL3-mediated maturation of miR-126-5p promotes ovarian cancer progression via PTEN-mediated PI3K/Akt/mTOR pathway. *Cancer Gene Ther* 2020 Sep 16 [Epub]. <https://doi.org/10.1038/s41417-020-00222-3>.
 42. Lee KS, Nam SK, Koh J, et al. Stromal expression of microRNA-21 in advanced colorectal cancer patients with distant metastases. *J Pathol Transl Med* 2016; 50: 270-7.

Adenocarcinoma of the minor salivary gland with concurrent *MAML2* and *EWSR1* alterations

Sangjoon Choi¹, Junhun Cho¹, Seung Eun Lee², Chung-Hwan Baek³, Yi-Kyung Kim⁴, Hyung-Jin Kim⁴, Young Hyeon Ko¹

¹Department of Pathology and Translational Genomics, Samsung Medical Center, Sungkyunkwan University School of Medicine, Seoul;

²Department of Pathology, Konkuk University Medical Center, Konkuk University School of Medicine, Seoul;

Departments of ³Otorhinolaryngology-Head and Neck Surgery and ⁴Radiology, Samsung Medical Center, Sungkyunkwan University School of Medicine, Seoul, Korea

Salivary gland tumors are histologically diverse, and each entity has distinctive histopathological and molecular features. We report two cases of salivary gland tumors with unique histological and molecular findings, which have not been documented previously. The tumors were located in the base of the tongue in both patients. Most tumor cells were arranged in cords and nests, giving a trabecular-like appearance. Focally, glandular structures with intraluminal mucin and perivascular pseudorosette-like configurations were identified. Tumor cells had eosinophilic to clear cytoplasm, and showed mild nuclear atypia. They were positive for pancytokeratin and negative for S-100, p63, c-KIT, androgen receptor, and neuroendocrine markers. Multiple foci of capsular or lymphovascular invasion were identified, but the Ki-67 labeling index was low (<5%). Fluorescence in situ hybridization revealed concurrent alterations of *MAML2* and *EWSR1* gene. Further investigations with a larger number of cases with similar histological and molecular features will accurately classify this tumor.

Key Words: Salivary gland; Neoplasm; *EWSR1* gene; *MAML2* gene

Received: June 1, 2020 **Revised:** December 1, 2020 **Accepted:** December 11, 2020

Corresponding Author: Young Hyeon Ko, MD, Department of Pathology and Translational Genomics, Samsung Medical Center, Sungkyunkwan University School of Medicine, 81 Irwon-ro, Gangnam-gu, Seoul 06351, Korea

Tel: +82-2-3410-2762, Fax: +82-2-3410-6396, E-mail: yhko310@skku.edu

Salivary gland neoplasms are uncommon and account for only 3%–10% of head and neck tumors [1]. Tumors of the salivary gland are classified into distinct subgroups by their characteristic histological features, immunoprofiles, and genetic alterations, and the histological subgroups have unique clinical characteristics. In the current World Health Organization (WHO) classification of head and neck tumors, salivary gland tumors are classified into 21 malignant tumors, 11 benign tumors, and one tumor with uncertain malignant potential. However, tumors with characteristic histological types that do not meet the current diagnostic criteria are still being reported. Moreover, salivary gland neoplasms are often diagnostically challenging because of the morphologic overlap in some of the tumors and the presence of variants and mimickers. As immunostaining is usually not helpful in distinguishing peculiar cases, molecular analysis is necessary for accurate tumor classification.

We recently encountered two cases of minor salivary gland

neoplasms with unique morphology, which do not meet the diagnostic criteria for a specific entity and are unclassifiable in the current WHO classification of head and neck tumors. The tumors were comprised of only epithelial components with trabecular arrangement and they formed focal mucin-producing glandular structures, and fluorescence in situ hybridization (FISH) analysis showed concurrent alteration of *MAML2* gene as well as *EWSR1* gene. This genetic change is exceedingly rare in head and neck tumors and only one case report has been published regarding dual gene rearrangement of *MAML2* and *EWSR1* [2].

Histological features of these tumors have not been reported previously, and their biological behaviors are unknown. Herein, we describe detailed clinicopathological and molecular characteristics of two minor salivary gland adenocarcinoma cases with *MAML2* and *EWSR1* alterations. We anticipate this report will extend the knowledge on this rare, but distinct tumor of the minor salivary gland.

CASE REPORT

Case 1

A 48-year-old woman (patient 1) who had a history of hyperthyroidism and rheumatoid arthritis was referred to our hospital for examination of a mass in the base of her tongue, which was found accidentally during cervical magnetic resonance imaging (MRI) for neck pain evaluation. Clinically, the mass was palpable at the right sublingual gland site, but the patient had no symptoms.

MRI revealed a solid and cystic lesion measuring 3 cm in the right tongue base that seemed to have originated from the right sublingual gland. Positron emission tomography revealed ¹⁸F-fluorodeoxyglucose uptake of the mass and mild hypermetabolic lymph nodes in the right level 1b area, which were suspicious of metastasis. Distant metastasis to other organs was not identified. The patient subsequently underwent sublingual mass excision. She developed no local or distant recurrence of the disease 20 months after the surgery.

Case 2

Patient 2 was sent to us for consultation. This 63-year-old otherwise healthy woman was admitted for chronic tonsillitis with pain.

Computed tomography revealed a submucosal mass measuring 2.1 cm in the right tongue base with focal cystic and necrotic areas. The bilateral neck lymph nodes were not significantly enlarged. Excisional biopsy was performed on the tongue base mass. The patient was referred to our hospital for further treatment. There was no evidence of recurrence or metastasis during the 14-month follow-up.

Pathological findings

We examined surgically resected specimens obtained from the right tongue base mass from each patient. The gross examination of the resected tumors showed relatively well-circumscribed, white tan-colored, solid masses with focal cystic changes and hemorrhage. Microscopically, the tumors were highly vascularized, and tumor cells were arranged in variably sized nests and cords that were separated by delicate fibrous septa containing thin blood vessels, which formed a trabecular-like pattern (Figs. 1A, 2A). Cytologically, the tumor cells were round to ovoid or sometimes spindle shaped and tended to have long and clear to abundant eosinophilic and granular cytoplasm. The tumor cells had small- to medium-sized nuclei with mild to moderate nuclear membrane irregularity, vesicular chromatin, and incon-

spicuous nucleoli. The nuclei were aligned side by side perpendicular to the basement membrane around the vessels of the septum.

In the tumor from patient 1, the nucleus was positioned away from the basement membrane and toward the fibrovascular septa, which imparted the appearance of reverse polarity. The blood vessels between tumor cell nests were usually thin, but perivascular hyalinization was prominent in some areas. Around these blood vessels, perivascular pseudorosette-like arrangements of nuclei were observed (Fig. 1B). Peripheral nuclear palisading was seen in this area. Focally, glandular structures with intraluminal and intracytoplasmic mucins were identified in both patients' tumors (Figs. 1C, 2B). There was no identifiable perineural invasion by the tumor cells; however, capsular invasion and lymphovascular invasion were occasionally found (Fig. 1D). Mitotic figures and tumor necrosis were not identified. There was no metastasis in the right level 1b lymph node from patient 1.

The tumor cells showed diffuse positivity for cytokeratin (AE1/AE3) (Figs. 1E, 2C). The pseudorosette-like components identified in patient 1 were weakly positive for cytokeratin. They also displayed CD99 immunoreactivity, which highlighted thick hyalinized blood vessels (Fig. 1F). Immunohistochemical staining for chromogranin, CD56, smooth muscle actin (SMA), S-100, c-KIT, and androgen receptor (AR) were negative in tumor cells. The lack of p63 staining indicated an absence of myoepithelial differentiation in this tumor (Fig. 1G). CD34 staining revealed marked vascular proliferation between the tumor glands or nests. The Ki-67 labeling index was < 5% (Figs. 1H, 2D). Special staining for mucin using mucicarmine, periodic acid–Schiff, and periodic acid–Schiff–diastase showed the presence of intraluminal and cytoplasmic mucin in the tumor cells.

We performed break apart FISH analysis with *MAML2*, *EWSR1*, and *ETV6* probes to confirm genetic changes of this tumor. A minimum of 50 tumor cell nuclei were evaluated. FISH results were interpreted as positive when > 10% of tumor cells showed a split of the red and green signals by ≥ 2 signal diameters, or when a green signal deletion was identified. Both cases had evidence of *MAML2* and *EWSR1* alterations and were negative for *ETV6*. One case had alteration (partial deletion or unbalanced translocation) of *MAML2* and translocation of *EWSR1* (Fig. 3A, B). The other case showed translocations of *MAML2* and *EWSR1* (Fig. 3C, D).

Targeted next-generation sequencing (NGS) using CancerSCAN NGS panel was performed only for case 1 because of the lack of available tissue in case 2. Deep targeted sequencing detected 19 single nucleotide variants (SNV) including *TOP1*, *PMS2*,

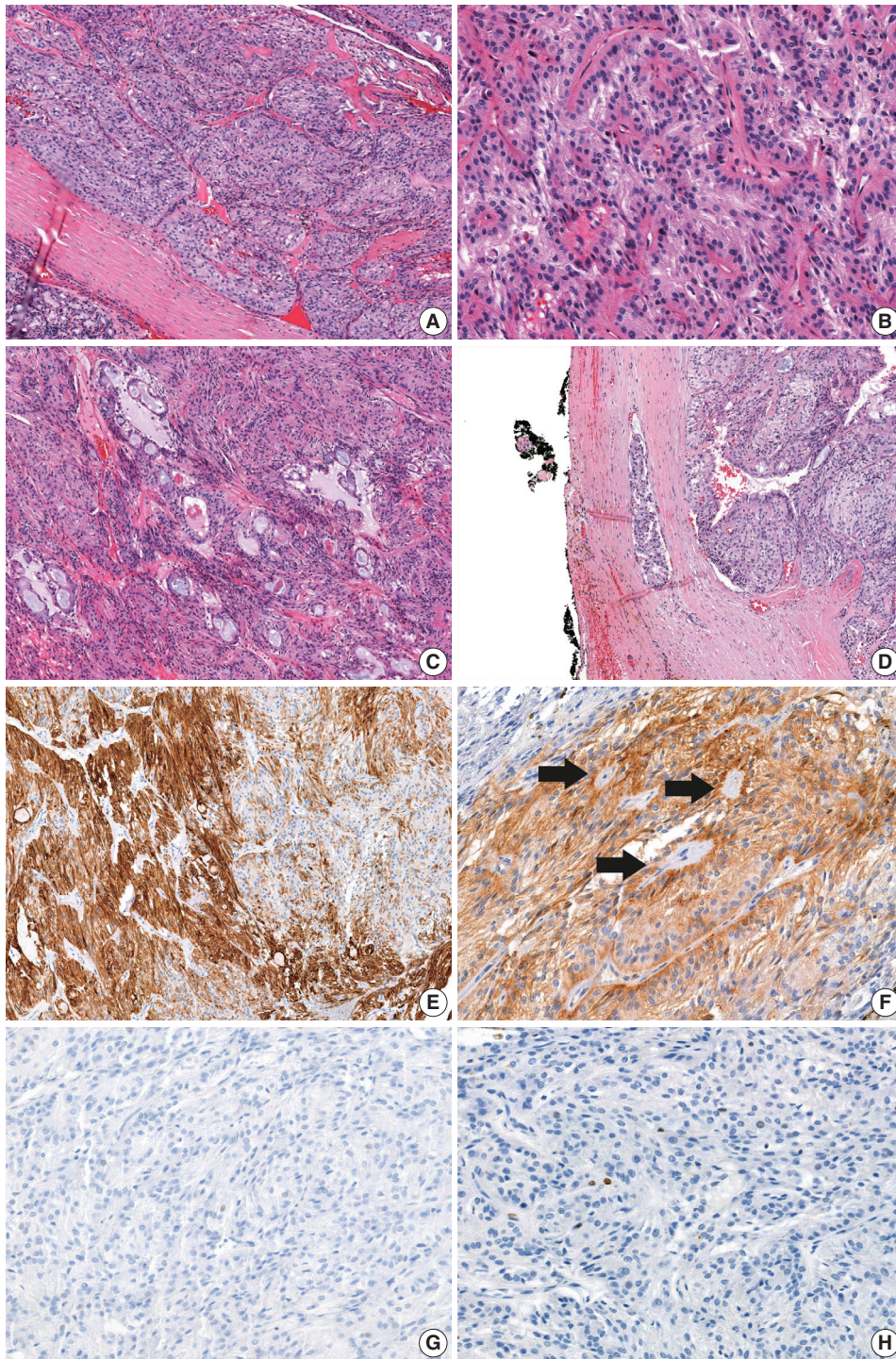


Fig. 1. Histopathological findings and immunostaining results for case 1. (A) Low-power image shows cords and nests of tumor cells separated by fibrous septa. The tumor cells appear round to polygonal and contain bland-looking nuclei with fine chromatin and abundant eosinophilic granular cytoplasm. Mucinous cells are scattered throughout the tumor. (B) In some areas, tumor cell nuclei show peripheral palisading around blood vessels, which give a perivascular pseudorosette-like appearance. (C) Focally, tumor cells show glandular differentiation and intraluminal mucin secretion. (D) Endolymphatic tumor emboli are found in the peritumoral fibrous capsule. (E) Cytokeratin (AE1/AE3) staining is positive in both the trabecular and glandular components (left side), but focal staining is observed in the rosettoid area (right side). (F) Tumor cells around the hyalinized vasculatures (arrows) with pseudorosette-like arrangement exhibit positive CD99 immunoreactivity. (G) Immunohistochemical staining for p63 reveals the lack of myoepithelial differentiation of this tumor. (H) The Ki-67 labeling index in tumor cells is very low (<1%).

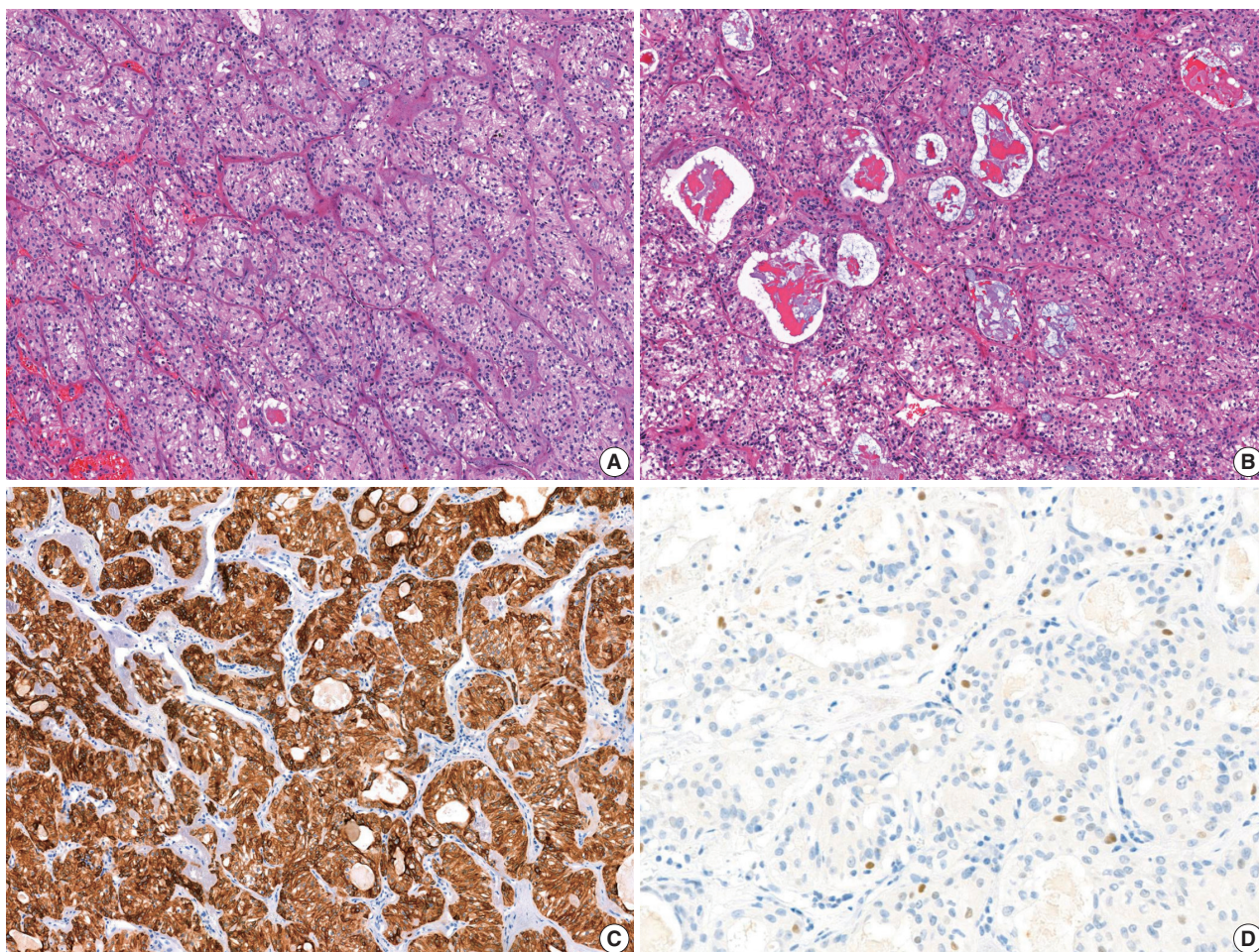


Fig. 2. Histopathological findings and immunostaining results for case 2. (A) Low-power image shows the tumor cells arranged in nests and cords which are surrounded by thick fibrous septa, forming trabecular growth pattern. The tumor cells possess lightly eosinophilic to clear cytoplasm. (B) Glandular components with intraluminal and intracytoplasmic mucin secretion are found in multiple areas. (C) Cytokeratin (AE1/AE3) staining reveals diffuse strong positive reactivity. (D) Focal p63 expressions are found in only a few tumor cells.

NPM1, *NF1*, *MAP2K4*, *HSP90AA1*, and *GNAQ*. Seventeen variants were nonsynonymous SNVs, and two were stop-gain SNV and non-frameshift deletion. Despite the high tumor purity (>80%), all of the alterations had very low variant allele frequency (<5.0%), and these variants were regarded as subclonal changes with genetic heterogeneity of tumor cells or possible sequencing errors.

DISCUSSION

Classification of salivary gland tumors is based mainly on histomorphology, lineage, and biological features [1]. Although no single antibody is specific for a tumor entity, the combination of immunohistochemical markers is helpful in the differential diagnosis of salivary gland neoplasms. With advances in the molecular diagnostics, specific genetic alterations in salivary gland

tumors have been identified, and the classification is being further refined [3].

The two cases of salivary gland tumors reported here displayed unique histological changes that have not been described previously. The tumors displayed a corded and nested growth pattern with focal glandular differentiation and prominent vascularization. They had bland, round nuclei with inconspicuous nucleoli, and eosinophilic or clear cytoplasm. One of the two cases displayed pseudorosette-like arrangements around thickened blood vessels. Immunohistochemical staining for cytokeratin, SMA, S-100, c-KIT, p63, AR, and neuroendocrine markers revealed epithelial differentiation of the tumor cells, which were devoid of a myoepithelial component. Because this histological feature does not fit into any known type of salivary gland neoplasm, these tumors were initially diagnosed as adenocarcinoma, not otherwise specified.

Characteristic chromosomal rearrangements are found in many

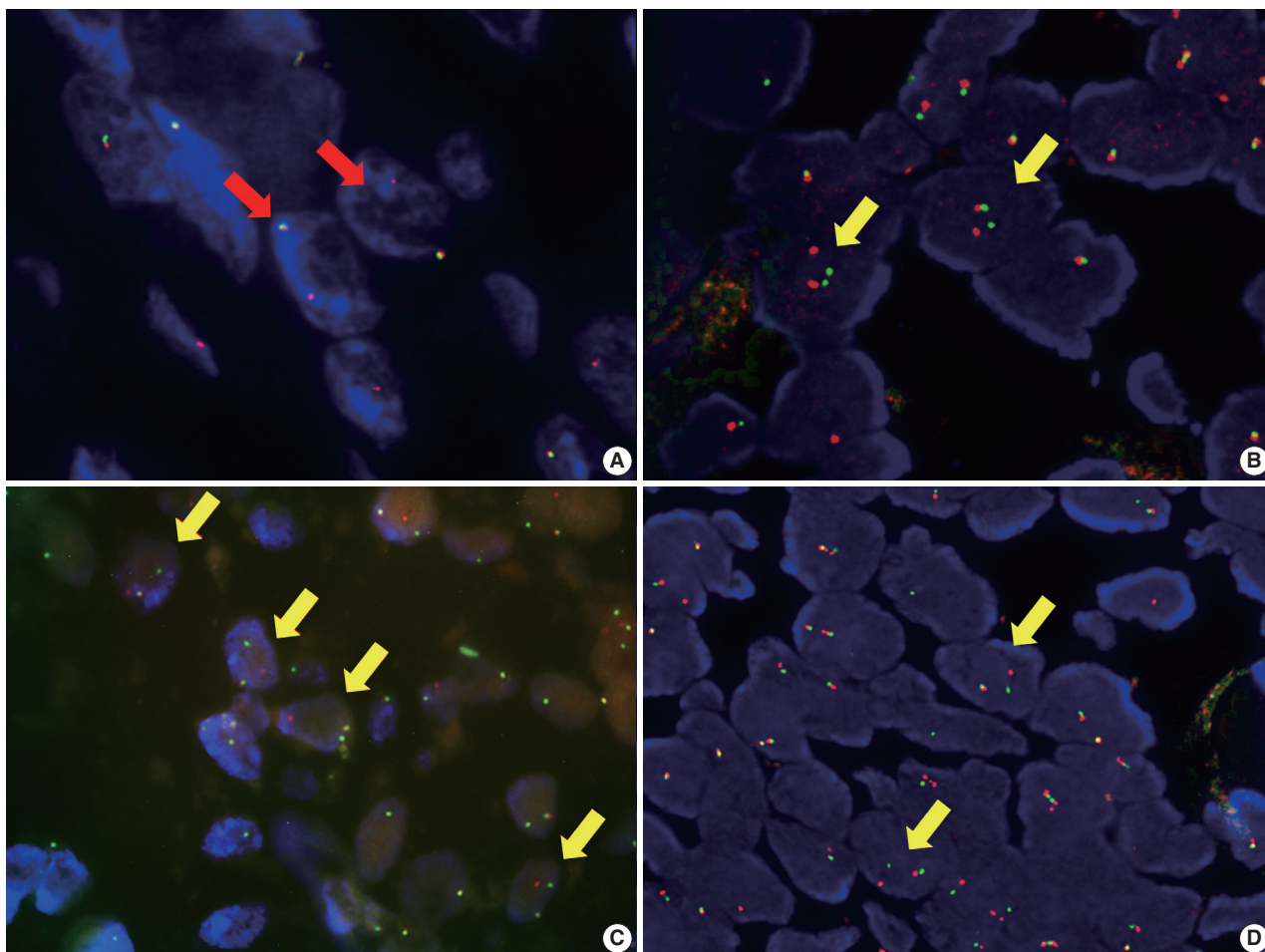


Fig. 3. Representative image of fluorescence in situ hybridization (FISH) analysis for *MAML2* and *EWSR1* from case 1 (A, B) and 2 (C, D). (A, B) In case 1, FISH analysis for *MAML2* reveal one fused signal and a single red signal (red arrows), suggesting partial deletion or unbalanced translocation of *MAML1* (A). (B) *EWSR1* shows one fused signal and separate red and green signal (yellow arrows), indicating translocation of *EWSR1*. (C, D) Case 2 shows several cells with split of red and green signals (yellow arrows) for *MAML2* (C) and *EWSR1* (D), indicating concurrent *MAML1* and *EWSR1* rearrangement.

salivary gland neoplasms. For example, *CRTC1–MAML2* fusion in mucoepidermoid carcinoma (MEC), *ETV6–NTRK3* fusion in secretory carcinoma, *MYB–NFIB* fusion in adenoid cystic carcinoma, and *EWSR1–ATF1* fusion in clear cell carcinoma (CCC) are well-known translocations and they are diagnostic for each tumor [4]. However, the presence of dual gene rearrangement in tumors of the salivary gland is extremely rare. Currently, there has been only one case report of intraosseous maxillary tumor harboring *MAML2* and *EWSR1* rearrangement [2]. The tumor consisted of sheets and nests of clear tumor cells with intervening hyalinized and desmoplastic septa. Epidermoid cells and mucinous cells were scattered throughout the tumor. FISH analysis showed rearrangement of both *MAML2* and *EWSR1* genes. Based on histomorphology and the cytogenetic findings, Hamza et al. [2] presumed this tumor as a hybrid of clear cell variant of MEC and

clear cell odontogenic carcinoma. Similarly, in our case, positive results of *MAML2* and *EWSR1* analysis suggest the possibility of MEC or CCC. Interestingly, tumor cells showing one fused signal and a single red signal of *MAML2* probe were frequently observed in one case, which could represent partial deletion or unbalanced translocation of the *MAML2* gene. This unusual FISH pattern has also been previously reported in high-grade MEC [5].

MEC is the most common malignant salivary gland tumor. They are composed of varying proportions of squamoid, mucin-producing, and intermediate cells forming cystic and solid patterns. They are classified as low, intermediate, and high-grade, and the grading criteria include the proportion of mucous-cells, tumor invasiveness, anaplasia, mitotic rates, tumor necrosis, perineural or lymphovascular invasion, and the proportion of cystic component. Low-grade MECs are usually well circumscribed,

mucous cell-rich, and have a prominent cystic component [6-8]. Most MECs are characterized by specific gene fusions involving *MAML2*, with a high tendency in low to intermediate grade tumors [9,10]. In our case, the tumor cells are mainly arranged in cords and nests exhibiting trabecular-like pattern, and partly form glands with intracytoplasmic and luminal mucin production. Although well-circumscribed tumor border and the presence of mucin-producing cells are reminiscent of low-grade MEC, epidermoid cells or intermediate cells which are helpful in diagnosis of MEC are not observed. Furthermore, variants of MECs known to date (oncocyctic, Warthin-like, ciliated, and sclerosing) [10-13] did not cover the histological characteristics as in our cases.

CCC is a low-grade salivary gland carcinoma, frequently arising in the minor salivary glands, particularly in the base of the tongue. CCCs are composed of malignant cells with solid sheets, nests, cords, and trabecular growth pattern surrounded by hyalinizing stroma. Tumor cells may also show mucinous differentiation either focally or diffusely [14]. Diffuse and strong p63-reactivity and *EWSR1-ATF1* gene fusion is consistently identified in CCC [15]. In our patients, most tumor cells showed a corded and nested configuration with some glandular differentiation, and cytoplasmic clearing were partly observed. However, immunohistochemical staining revealed a lack of p63 expression in both cases, which does not match pathological characteristics of CCC.

In our cases, we used break apart probes to identify rearrangement of *MAML2* and *EWSR1*, but unfortunately, we could not reveal the fusion partners. Nevertheless, based on positive FISH results of both genes, we suspect that these tumors possibly possess pathologic and molecular characteristics of both MEC and CCC. Identifying the specific fusion partner of *MAML2* and *EWSR1* would be helpful in refining this tumor entity.

The Ki-67 labeling index has been reported as a prognostic indicator and may be used for the differential diagnosis between malignant and benign tumors of the salivary gland [16,17]. Ki-67 labeling index is usually < 5% in benign tumors and > 10% in malignant tumors. The tumors described here had a low Ki-67 labeling index—both < 5%. Based on the Ki-67 labeling index, this tumor could be defined as a benign neoplasm. However, histologic features, especially lymphovascular or capsular invasion, support that these tumors are malignant. The very low Ki-67 labeling index suggests that these tumors are low-grade malignancy. A larger number of cases with long-term follow-up is needed to determine the exact prognosis.

We identified 19 somatic variants (*TOP1*, *PMS2*, *NPM1*, *NF1*, *MAP2K4*, *HSP90AA1*, and *GNAQ*) in the samples from

patient 1. These variants have not been previously reported for any other types of salivary gland tumors and may be associated with neoplastic transformation or progression. However, allele frequency of these variants was so low that it is doubtful that these genes have any diagnostic significance.

In conclusion, we have presented two cases of adenocarcinoma of minor salivary glands with concurrent *MAML2* and *EWSR1* alteration, which displayed unique histological changes that have not been previously described in other types of salivary gland neoplasms. Cords, nests, and trabecular-like arrangements of tumor cells are predominant, with foci of glandular components composed of mucous-cells. Well-circumscribed border, bland tumor nuclei, low Ki-67 labeling index, and non-aggressive clinical behavior suggest that these tumors are low-grade malignancies. Further investigations involving more cases sharing similar histological and molecular features are needed to define this unusual type of salivary gland tumor.

Ethics Statement

This study was approved by the Institutional Review Board of Samsung Medical Center with a waiver of informed consent (IRB No. 2020-02-146-001) and was performed in accordance with the principles of the 1964 Helsinki Declaration.

ORCID

Sangjoon Choi	https://orcid.org/0000-0003-2108-0575
Junhun Cho	https://orcid.org/0000-0002-6089-9340
Seung Eun Lee	https://orcid.org/0000-0002-7459-0061
Chung-Hwan Baek	https://orcid.org/0000-0003-3602-4699
Yi-Kyung Kim	https://orcid.org/0000-0002-9395-4879
Hyung-Jin Kim	https://orcid.org/0000-0003-3576-3625
Young Hyeon Ko	https://orcid.org/0000-0002-4383-0579

Author Contributions

Conceptualization: YHK. Data curation: SC, JC, SEL, CHB, YKK, HJK, YHK. Formal analysis: SC, JC, YHK. Investigation: SC, JC. Visualization: SC. Writing—original draft: SC, YHK. Writing—review & editing: SC, YHK. Approval of final manuscript: all authors.

Conflicts of Interest

The authors declare that they have no potential conflicts of interest.

Funding Statement

No funding to declare.

Acknowledgments

We are grateful to Dr. Kyung-Ja Cho (Department of Pathology, Asan Medical Center) for providing *MAML2* FISH analysis with valuable comments.

References

1. El-Naggar AK, Chan JK, Grandis JR, Takata T, Sloatweg PJ. WHO classification of head and neck tumours. Lyon: IARC Press, 2017.
2. Hamza A, Yao CM, Lai SY, Bell D. Clear cell tumor of the maxilla

- with *MAML2* and *EWSR1* gene rearrangements: a true hybrid or a fluorescence in situ hybridization fumble? *AJSP Rev Rep* 2020; 25: 12-5.
3. Kato S, Elkin SK, Schwaederle M, et al. Genomic landscape of salivary gland tumors. *Oncotarget* 2015; 6: 25631-45.
 4. Skalova A, Stenman G, Simpson RH, et al. The role of molecular testing in the differential diagnosis of salivary gland carcinomas. *Am J Surg Pathol* 2018; 42: e11-27.
 5. Cipriani NA, Lusardi JJ, McElherne J, et al. Mucoepidermoid carcinoma: a comparison of histologic grading systems and relationship to *MAML2* rearrangement and prognosis. *Am J Surg Pathol* 2019; 43: 885-97.
 6. Auclair PL, Goode RK, Ellis GL. Mucoepidermoid carcinoma of intraoral salivary glands: evaluation and application of grading criteria in 143 cases. *Cancer* 1992; 69: 2021-30.
 7. Hicks MJ, el-Naggar AK, Flaitz CM, Luna MA, Batsakis JG. Histocytologic grading of mucoepidermoid carcinoma of major salivary glands in prognosis and survival: a clinicopathologic and flow cytometric investigation. *Head Neck* 1995; 17: 89-95.
 8. Goode RK, Auclair PL, Ellis GL. Mucoepidermoid carcinoma of the major salivary glands: clinical and histopathologic analysis of 234 cases with evaluation of grading criteria. *Cancer* 1998; 82: 1217-24.
 9. Jee KJ, Persson M, Heikinheimo K, et al. Genomic profiles and *CRTC1-MAML2* fusion distinguish different subtypes of mucoepidermoid carcinoma. *Mod Pathol* 2013; 26: 213-22.
 10. Bishop JA, Cowan ML, Shum CH, Westra WH. *MAML2* rearrangements in variant forms of mucoepidermoid carcinoma: ancillary diagnostic testing for the ciliated and Warthin-like variants. *Am J Surg Pathol* 2018; 42: 130-6.
 11. Fujimaki M, Fukumura Y, Saito T, et al. Oncocytic mucoepidermoid carcinoma of the parotid gland with *CRTC1-MAML2* fusion transcript: report of a case with review of literature. *Hum Pathol* 2011; 42: 2052-5.
 12. Tasaki T, Matsuyama A, Tabata T, et al. Sclerosing mucoepidermoid carcinoma with eosinophilia of the salivary gland: case report and review of the literature. *Pathol Int* 2013; 63: 125-31.
 13. Ishibashi K, Ito Y, Masaki A, et al. Warthin-like mucoepidermoid carcinoma: a combined study of fluorescence in situ hybridization and whole-slide imaging. *Am J Surg Pathol* 2015; 39: 1479-87.
 14. Tanguay J, Weinreb I. What the *EWSR1-ATF1* fusion has taught us about hyalinizing clear cell carcinoma. *Head Neck Pathol* 2013; 7: 28-34.
 15. Weinreb I. Hyalinizing clear cell carcinoma of salivary gland: a review and update. *Head Neck Pathol* 2013; 7 Suppl 1: S20-9.
 16. Larsen SR, Bjorndal K, Godballe C, Krogdahl A. Prognostic significance of Ki-67 in salivary gland carcinomas. *J Oral Pathol Med* 2012; 41: 598-602.
 17. Luukka H, Klemi P, Leivo I, Vahlberg T, Grenman R. Prognostic significance of Ki-67 and p53 as tumor markers in salivary gland malignancies in Finland: an evaluation of 212 cases. *Acta Oncol* 2006; 45: 669-75.

A case of concomitant *EGFR/ALK* alteration against a mutated *EGFR* background in early-stage lung adenocarcinoma

Ki-Chang Lee¹, Jiwon Koh², Doo Hyun Chung², Yoon Kyung Jeon^{2,3}

¹Seoul National University College of Medicine, Seoul; ²Department of Pathology, Seoul National University Hospital, Seoul National University College of Medicine, Seoul; ³Cancer Research Institute, Seoul National University, Seoul, Korea

Rare cases of lung adenocarcinoma (LUAD) with concomitant epidermal growth factor receptor (*EGFR*) mutation and anaplastic lymphoma kinase (*ALK*) translocation have been reported. However, their clonal and evolutionary relationship remains unclear. We report a case of early-stage *EGFR*-mutated LUAD with a focal concomitant *EGFR/ALK* alteration. A 63-year-old male underwent lobectomy to remove a 1.9-cm-sized lung nodule, which was diagnosed with *EGFR*-mutated LUAD. *ALK* immunohistochemistry (IHC) showed focal positivity within the part of the tumor characterized by lepidic pattern, also confirmed by fluorescence in-situ hybridization (FISH). Targeted next-generation sequencing was performed separately on the *ALK* IHC/FISH-positive and -negative areas. *EGFR* L833V/L858R mutations were detected in both areas, whereas *EML4* (echinoderm microtubule-associated protein-like 4)-*ALK* translocations was confirmed only in the *ALK* IHC/FISH-positive area, suggesting the divergence of an *EGFR/ALK* co-altered subclone from the original *EGFR*-mutant clone. Our study suggests that concurrent alterations of *EGFR* and *ALK* can arise via divergent tumor evolution, even in the relatively early phases of tumorigenesis.

Key Words: Lung adenocarcinoma; Epidermal growth factor receptor; Anaplastic lymphoma kinase; Concomitant alteration; Targeted gene sequencing

Received: November 11, 2020 Accepted: December 16, 2020

Corresponding Author: Yoon Kyung Jeon, MD, PhD, Department of Pathology, Seoul National University Hospital, Seoul National University College of Medicine, 103 Daehak-ro, Jongno-gu, Seoul 03080, Korea

Tel: +82-2-740-8323, Fax: +82-2-743-5530, E-mail: ykjeon@snu.ac.kr

Lung adenocarcinoma (LUAD) accounts for >40% of lung cancers. It consists of several heterogeneous molecular subtypes defined by their oncogenic driver mutations [1,2]. Correctly classifying the molecular subtypes of LUAD is important in clinical practice because the presence of a certain driver mutation opens up therapeutic options that can improve the survival of patients with LUAD [1,2]. Epidermal growth factor receptor (*EGFR*) mutations and anaplastic lymphoma kinase (*ALK*) translocations are two of the most important oncogenic drivers in LUAD [2]. Although they are considered to be mutually exclusive [3], recent studies have shown that in some cases, albeit rarely, both *EGFR* mutation and *ALK* translocation are present in LUAD [4-9]. Most of those cases share several clinicopathological characteristics, including their advanced stage (III or IV) and a tumor morphology characteristic of LUAD due to translocated *ALK* [7]. In addition, in two cases, the immunohistochemistry (IHC) results suggested that the mutant-EGFR protein was ex-

pressed in the same tumor population as the *ALK* fusion protein [5,8]. However, here we report a case of early-stage LUAD with a concomitant *EGFR/ALK* alteration in which the *ALK* translocation was spatially segregated in a focal tumor area with a lepidic morphology.

CASE REPORT

A 63-year-old male patient who was a never-smoker presented with an incidentally found solitary pulmonary nodule. A pure ground-glass nodule (GGN) at the right lower lobe (RLL) had been detected 3 years previously, and a recent follow-up chest computed tomography (CT) exam had shown a GGN ~1.7 cm in diameter with a 0.5-cm solid portion (Fig. 1A, B). A positron emission tomography-CT fusion scan showed mild uptake by the GGN but no other hypermetabolic lesion (Fig. 1C). A lobectomy of the RLL was performed, and pathologic evaluation

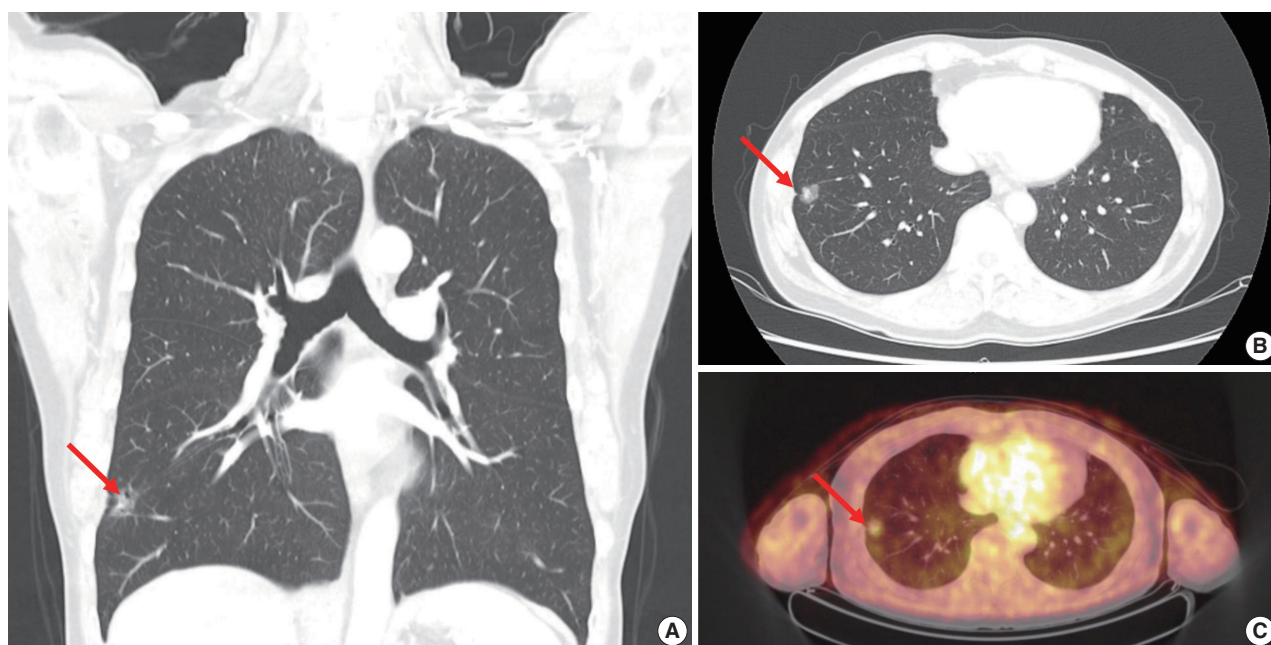


Fig. 1. Radiologic findings of the ground-glass nodule (GGN). (A, B) Coronal and axial computed tomography scan reveals a 1.7-cm GGN (arrows) with an inner solid portion measuring 0.5 cm in the right lower lobe of the lung. (C) The GGN (arrow) shows mild uptake on the positron emission tomography–computed tomography fusion scan, and no other hypermetabolic lesions are found.

of the lesion confirmed a primary LUAD, 1.9×1.4×1.3 cm in size, with a predominantly acinar pattern but also associated lepidic and papillary patterns. There was no evidence of pleural invasion or nodal metastasis (pT1bN0, IA) (Fig. 2).

Tests for *EGFR* mutation and *ALK* translocation were carried out as part of the routine molecular work-ups for non-small cell lung cancer (NSCLC). A missense mutation in *EGFR* exon 21 (L858R) was found by *EGFR* PANAMutypier (PANAGENE, Daejeon, Korea). *ALK* IHC (clone D5F3, Cell Signaling Technology, Danvers, MA, USA) showed focal positivity within the part of the tumor characterized by lepidic pattern (Fig. 2). Fluorescence in-situ hybridization (FISH) using a break-apart probe (Abbott Molecular Inc., Des Plaines, IL, USA) confirmed an *ALK* translocation in the *ALK*-positive area and its absence in the *ALK*-negative area of the tumor.

Targeted next-generation sequencing (NGS) using Axen Cancer Panel 1 (Macrogen Inc., Seoul, Korea), comprising 88 cancer-related genes, was performed separately on the *ALK* IHC/FISH-positive and *ALK* IHC/FISH-negative tumor tissue. *ALK* IHC/FISH-positive area was carefully microdissected from formalin-fixed, paraffin-embedded (FFPE) slide as shown in Fig 2, and *ALK* IHC/FISH-negative tumor tissue was obtained from a separate FFPE block with no *ALK* IHC-positive portions. The tissue from *ALK* IHC/FISH-negative area harbored *EGFR* L858R (variant allele frequency [VAF], 20.0%) and *EGFR* L833V (VAF,

19.5%) mutations (Fig. 3A). The two *EGFR* mutations were found in the same read, suggesting their presence in the same allele. Targeted sequencing of the *ALK* IHC/FISH-positive area revealed an *EML4* (echinoderm microtubule-associated protein-like 4)-*ALK* fusion with breakpoints occurring at intron 18 of *EML4* and intron 19 of *ALK* (Fig. 3B), as well as the same *EGFR* L858R and L833V mutations found in the *ALK* IHC/FISH-negative area, albeit at lower VAFs (5.9% and 3.4%, respectively) (Fig. 3A).

DISCUSSION

Here we report a case of early-stage LUAD with concomitant *EGFR* and *ALK* alterations. In the mutated *EGFR* background of the tumor, a focal area with an additional *ALK* translocation was identified by IHC and FISH. NGS confirmed that the *ALK*-positive lesion harbored dual *EGFR* and *ALK* alterations and that identical *EGFR* mutations were shared by both *ALK*-positive and -negative portions of the tumor, suggesting the divergence of an *EGFR/ALK* co-altered subclone from the original *EGFR*-mutant clone.

Both *EGFR* and *ALK* alterations are major driver mutations in LUAD, and was considered to be mutually exclusive [3]. However, rare cases with concomitant *EGFR* and *ALK* alterations have been reported [4-9]. The prevalence of concomitant *EGFR*

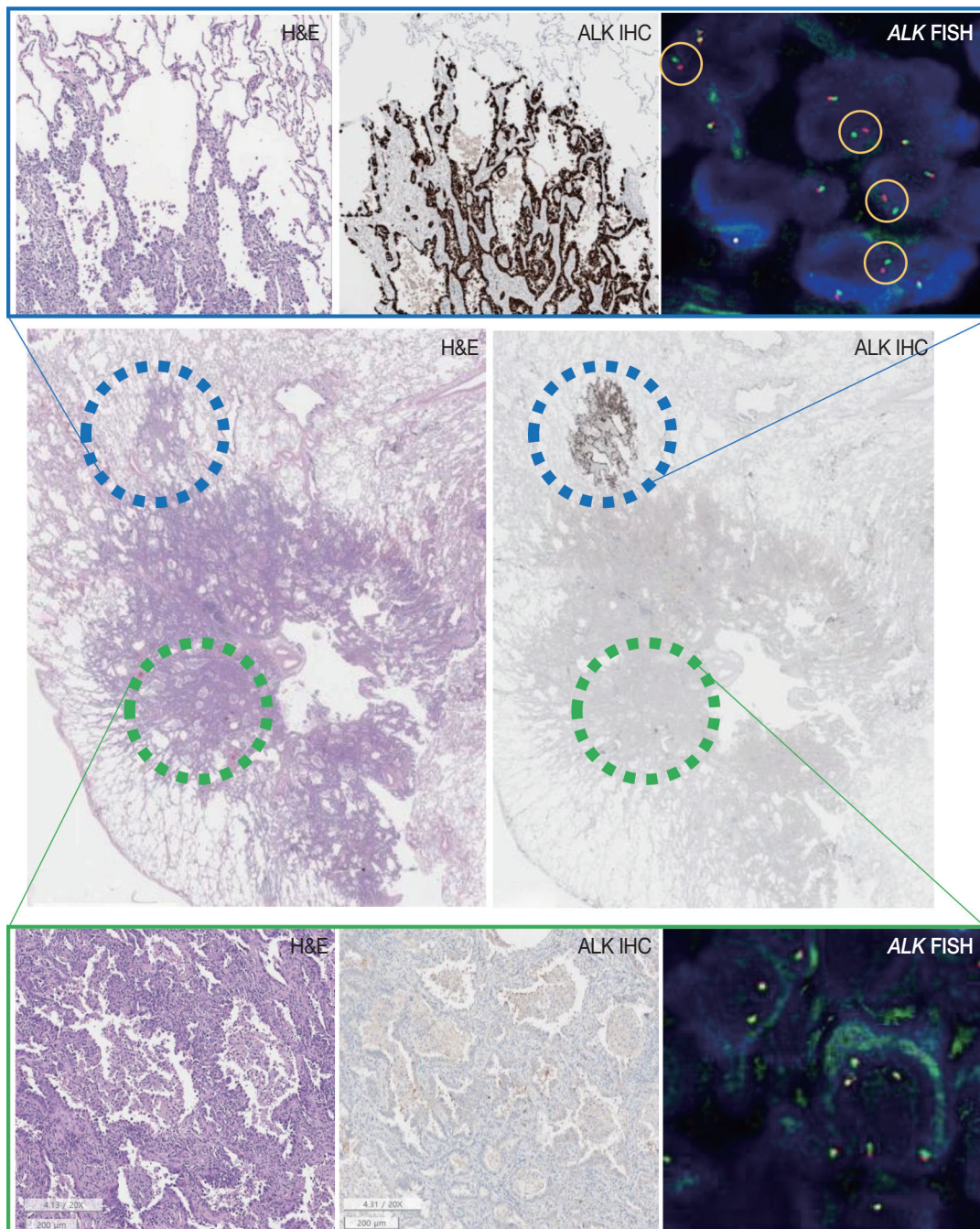


Fig. 2. Pathologic features of the tumor. Microscopic evaluation of the tumor section shows lung adenocarcinoma with a predominantly acinar pattern (green circle) but also a lepidic portion (blue circle). Anaplastic lymphoma kinase (ALK) immunohistochemistry (IHC) reveals the focal expression of ALK within the part of the tumor showing lepidic growth. On ALK fluorescence in-situ hybridization (FISH), split signals (yellow circles) are seen within the ALK IHC-positive area whereas the ALK IHC-negative area is conformed as negative. H&E, hematoxylin and eosin.

mutation and ALK translocation among NSCLC patients was estimated to be 0.9% [6]. Although our case is not the first report of a LUAD carrying both *EGFR* and *ALK* alterations, its clinicopathological features were unique.

In previous reports of LUAD with concomitant *EGFR/ALK*

alterations, the tumors were often clinically advanced [4,5,7-10], whereas in our patient the tumor was stage IA LUAD. These findings suggest that co-alterations of *EGFR* and *ALK* can occur in the very early phase of tumorigenesis. Pathologic evaluation of the tumor revealed the lepidic growth pattern of the ALK-pos-

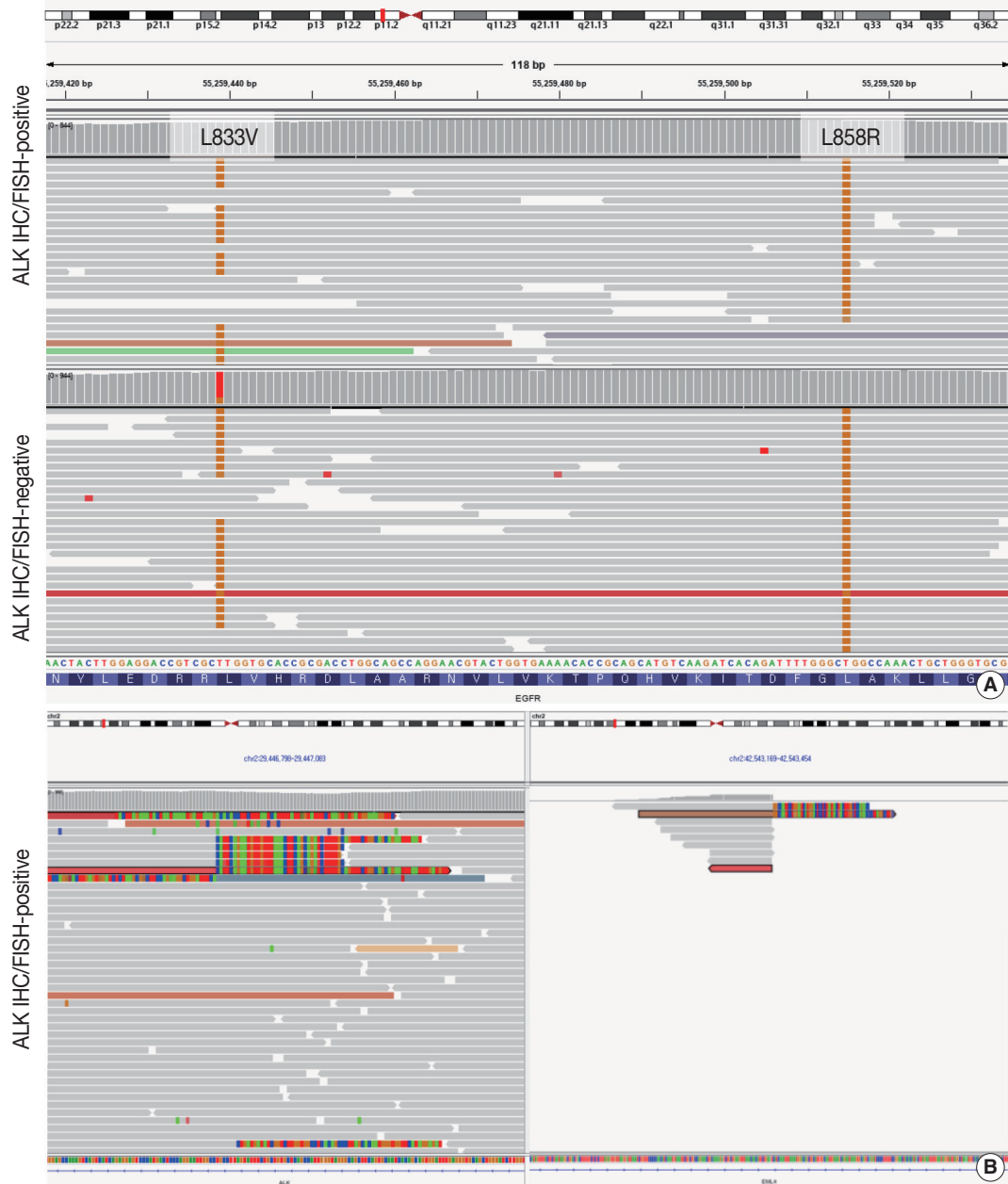


Fig. 3. Results of targeted sequencing of the anaplastic lymphoma kinase (ALK) immunohistochemistry (IHC)/fluorescence in-situ hybridization (FISH)-positive and -negative portions of the tumor. (A) Next-generation sequencing identified epidermal growth factor receptor (*EGFR*) L858R and L833V point mutations in both the *ALK* IHC/FISH-positive and -negative portions of the tumor, albeit with different variant allele frequencies. Tissues for targeted sequencing were obtained from separate slides to avoid potential contamination. Since both *EGFR* mutations were found in the same read, it is likely that they occurred in the same allele. (B) Soft clipped reads of *ALK* (left) and *EML4* (echinoderm microtubule-associated protein-like 4) (right) with breakpoints at intron 18 of *EML4* and intron 19 of *ALK* were found in the *ALK* IHC/FISH-positive portion of the tumor and suggested the fusion of the two genes.

itive portion whereas the pattern in the *ALK*-negative portion was predominantly acinar. LUADs with concomitant *EGFR/ALK* alterations frequently exhibited a solid, cribriform, or micropapillary patterns [7], while our case suggests that LUAD with co-altered *EGFR/ALK* can also include low-grade histologic

patterns. These findings demonstrate that LUAD with concomitant *EGFR/ALK* alterations is not limited to a single morphology but may, instead, be characterized by a wide histologic spectrum.

Despite previous reports of concomitant *EGFR/ALK* co-altered LUADs, the spatial and sequential contexts of the two altera-

tions are poorly understood. Yang et al. [5] identified seven cases of LUAD with co-localized expression of mutant *EGFR* and *ALK*, determined in serial sections of the FFPE tumor samples. Their observations evidenced the intra-tumor and potential intracellular coexistence of *EGFR* and *ALK* alterations in certain LUADs. Our case also shows that *EGFR* and *ALK* can be co-altered in LUAD within the same tumor population, as verified by targeted sequencing. Moreover, the sequencing results provided additional insights, by revealing combined L858R and L833V mutations in the *EGFR* gene. This is an extremely rare finding, with only a single case identified among 783 NSCLCs analyzed [11]. Thus, it is highly unlikely that the *EGFR* L858R and L833V mutations in the *ALK*-positive and *ALK*-negative areas occurred independently, de novo; rather, a more plausible scenario is that the two-point mutations arose as a single first hit, followed by *ALK* translocation in a subclone stemming from the main tumor that subsequently followed a divergent evolution.

The spatial distribution of the mutant *EGFR* and *ALK* fusion proteins in two advanced LUAD cases was previously analyzed using IHC, and the homogeneous co-localization of the *EGFR/ALK* alterations was determined in both [8]. This finding contrasts with the present case, in which the *ALK* translocation was likely to have been a sub-clonal event that gives rise to LUAD with co-altered *EGFR/ALK*. Further studies are needed to verify that, in tumorigenesis of LUAD with concomitant *EGFR/ALK* alterations, the two events were indeed consecutive.

Nevertheless, the possibility of collision tumor cannot be completely ruled out; current extraction-based, bulk sequencing cannot verify that two *EGFR* mutations and *ALK* translocation exist in the very same tumor cell. However, we performed NGS after careful microdissection of the tumor area showing lepidic pattern, where virtually every tumor cells stained positive for *ALK* protein. This implies that the likelihood of the presence of *EGFR*-only-mutated tumor cell population within the microdissected area would be extremely low. Recent advances in single-cell sequencing technology would help deciphering the clonal events in single-cell resolution.

There is currently no consensus regarding the treatment of LUAD with concomitant *EGFR/ALK* alterations, and conflicting results on the efficacy of *EGFR* tyrosine kinase inhibitors (TKI) versus *ALK* inhibitors as first-line treatment have been reported [4-9]. Won et al. [4] found that the clinical outcome of patients treated with *ALK* inhibitors was substantially better than that of patients treated with *EGFR* TKIs. However, based on their own multi-center retrospective analysis and review of published data, Schmid et al. [9] concluded that *EGFR/ALK* co-altered

LUADs were more likely to be resistant to *ALK* inhibitors than to *EGFR* TKIs. Yang et al. [5] attempted to explain these conflicting results by considering the phosphorylation status of *EGFR* and *ALK* as potential predictive biomarkers of treatment response, but the number of patients analyzed was too small to draw definitive conclusions.

In our patient, although kinase inhibitor treatment was not needed, as the tumor was small enough to be locally excised, it is reasonable to assume that the treatment response would have been better with an *EGFR* TKI than with an *ALK* inhibitor, because the *ALK* translocation was present only in a subclone of the tumor. Identification of the initial genetic alteration may therefore aid in determining the primary driver mutation in *EGFR/ALK* co-altered LUAD, even in advance-stage tumors, as it may, in turn, lead to optimal treatment selection.

In summary, we report a case of early-stage, *EGFR*-mutated LUAD with a focal *EGFR/ALK* co-alteration. Our study suggests that concurrent mutations of *EGFR* and *ALK* can arise via divergent tumor evolution, even in the relatively early phases of tumorigenesis.

Ethics Statement

This study was approved by the Institutional Review Board (IRB) of Seoul National University Hospital (No. H-1911-035-1077) and written informed consent from the patient was waived by IRB decision.

ORCID

Ki-Chang Lee	https://orcid.org/0000-0003-2358-8698
Jiwon Koh	https://orcid.org/0000-0002-7687-6477
Doo Hyun Chung	https://orcid.org/0000-0002-9948-8485
Yoon Kyung Jeon	https://orcid.org/0000-0001-8466-9681

Author Contributions

Conceptualization: YKJ, DHC. Data curation: KCL, JK. Formal analysis: KCL, JK, YKJ. Investigation: KCL, JK. Visualization: KCL, JK. Writing—original draft: KCL, JK, YKJ. Writing—review & editing: YKJ, DHC. Approval of final manuscript: all authors.

Conflicts of Interest

The authors declare that they have no potential conflicts of interest.

Funding Statement

This study was funded by Basic Science Research Program (grant No.: NRF-2016R1D1A1B01015964) through the National Research Foundation (NRF) funded by the Ministry of Education, Science and Technology (MEST).

References

- Zheng M. Classification and pathology of lung cancer. *Surg Oncol Clin N Am* 2016; 25: 447-68.
- Lindeman NI, Cagle PT, Aisner DL, et al. Updated molecular testing guideline for the selection of lung cancer patients for treatment with targeted tyrosine kinase inhibitors: guideline from the College

- of American Pathologists, the International Association for the Study of Lung Cancer, and the Association for Molecular Pathology. *Arch Pathol Lab Med* 2018; 142: 321-46.
3. Gainor JF, Varghese AM, Ou SH, et al. *ALK* rearrangements are mutually exclusive with mutations in *EGFR* or *KRAS*: an analysis of 1,683 patients with non-small cell lung cancer. *Clin Cancer Res* 2013; 19: 4273-81.
 4. Won JK, Keam B, Koh J, et al. Concomitant *ALK* translocation and *EGFR* mutation in lung cancer: a comparison of direct sequencing and sensitive assays and the impact on responsiveness to tyrosine kinase inhibitor. *Ann Oncol* 2015; 26: 348-54.
 5. Yang JJ, Zhang XC, Su J, et al. Lung cancers with concomitant *EGFR* mutations and *ALK* rearrangements: diverse responses to *EGFR*-TKI and crizotinib in relation to diverse receptors phosphorylation. *Clin Cancer Res* 2014; 20: 1383-92.
 6. Lee JK, Kim TM, Koh Y, et al. Differential sensitivities to tyrosine kinase inhibitors in NSCLC harboring *EGFR* mutation and *ALK* translocation. *Lung Cancer* 2012; 77: 460-3.
 7. Lee T, Lee B, Choi YL, Han J, Ahn MJ, Um SW. Non-small cell lung cancer with concomitant *EGFR*, *KRAS*, and *ALK* mutation: clinicopathologic features of 12 cases. *J Pathol Transl Med* 2016; 50: 197-203.
 8. Baldi L, Mengoli MC, Bisagni A, Banzi MC, Boni C, Rossi G. Concomitant *EGFR* mutation and *ALK* rearrangement in lung adenocarcinoma is more frequent than expected: report of a case and review of the literature with demonstration of genes alteration into the same tumor cells. *Lung Cancer* 2014; 86: 291-5.
 9. Schmid S, Gautschi O, Rothschild S, et al. Clinical outcome of *ALK*-positive non-small cell lung cancer (NSCLC) patients with de novo *EGFR* or *KRAS* co-mutations receiving tyrosine kinase inhibitors (TKIs). *J Thorac Oncol* 2017; 12: 681-8.
 10. Fan J, Dai X, Wang Z, et al. Concomitant *EGFR* mutation and *EML4-ALK* rearrangement in lung adenocarcinoma is more frequent in multifocal lesions. *Clin Lung Cancer* 2019; 20: e517-30.
 11. Hata A, Yoshioka H, Fujita S, et al. Complex mutations in the epidermal growth factor receptor gene in non-small cell lung cancer. *J Thorac Oncol* 2010; 5: 1524-8.

Malignant rhabdoid tumor of the kidney in an adult with loss of INI1 expression and mutation in the *SMARCB1* gene

Eunkyung Han¹, Jiyeon Kim¹, Min Jung Jung¹, Susie Chin¹, Sang Wook Lee², Ahrim Moon¹

Departments of ¹Pathology and ²Urology, Soonchunhyang University Bucheon Hospital, Soonchunhyang University College of Medicine, Bucheon, Korea

A 57-year-old man with left flank pain was referred to our institute. Computed tomography scans revealed two enhancing masses in the left kidney. The clinical diagnosis was renal cell carcinoma (RCC). He underwent a radical nephrectomy with an adrenalectomy. Two well-circumscribed solid masses in the hilum and the lower pole (4.5 × 3.5 cm and 7.0 × 4.1 cm) were present. Poorly cohesive uniform round to polygonal epithelioid cells making solid sheets accounted for most of the tumor area. The initial diagnosis was RCC, undifferentiated with rhabdoid features. As the tumor showed loss of INI1 expression and a mutation in the *SMARCB1* gene on chromosome 22, the revised diagnosis was a malignant rhabdoid tumor (MRT) of the kidney. To date, only a few cases of renal MRT in adults have been reported. To the best of our knowledge, this is the first report of MRT in the native kidney of an adult demonstrating a *SMARCB1* gene mutation, a hallmark of MRT.

Key Words: Rhabdoid tumor; Kidney; Adult; INI-1; *SMARCB1*

Received: September 29, 2020 **Revised:** November 13, 2020 **Accepted:** January 26, 2021

Corresponding Author: Ahrim Moon, MD, Department of Pathology, Soonchunhyang University Bucheon Hospital, Soonchunhyang University College of Medicine, 170 Jomaru-ro, Bucheon 14584, Korea
 Tel: +82-32-621-5963, Fax: +82-32-621-5961, E-mail: armoon@schmc.ac.kr

Malignant rhabdoid tumor (MRT) of the kidney is an uncommon renal tumor mainly reported in children. This tumor is aggressive with a poor prognosis [1]. It was thought of as a tumor of the pediatric group until recently. Since the first reported case by Lowe et al. [2] in 1990, only limited case reports have been published on MRT of the kidney in adult patients [2-9].

Here, we report a rare case of MRT of the kidney in a 57-year-old male. The diagnosis was supported by immunohistochemistry and molecular studies. The microscopic, immunohistochemical, and molecular characteristics of this tumor are described in this report.

CASE REPORT

A 57-year-old Korean male presented with left flank pain lasting for a day at the urology department of an outside hospital. He was a previous smoker on medication for hypertension. He was diagnosed with spontaneous intracerebral hemorrhage 9 years ago and a ureter stone 7–8 years ago. Physical examination revealed left costovertebral angle tenderness. Under the im-

pression of a ureter stone, a non-contrast computed tomography (CT) was performed, and two masses were found in the left kidney. Additional contrast-enhanced CT scans revealed a 7-cm-sized heterogeneously enhancing lobulated mass in the lower pole of the left kidney involving the Gerota's fascia and a 4.4 cm-sized necrotic mass near the upper pole, raising suspicion for metastasis to a large necrotic lymph node in the hilum (Fig. 1A–C). The clinical diagnosis was renal cell carcinoma (RCC), stage IV. He was sent to our institution for surgical management, where the radiologists reviewed scans and drew the same conclusion (RCC, cT4N1) with some additional information: the mass might have invaded the left posterior abdominal wall, and the left adrenal gland abuts the upper pole mass. The patient underwent a radical nephrectomy with an adrenalectomy.

Specimens were then received for histopathological examination (Fig. 1D, E). The specimen consisting of the left kidney with perinephric fat, ureter, and adrenal gland measured 19 × 12 × 6 cm altogether. The kidney bore two well-circumscribed solid masses in the hilum near the upper pole and the lower pole, measuring 4.5 × 3.5 cm and 7.0 × 4.1 cm, respectively. On cross-

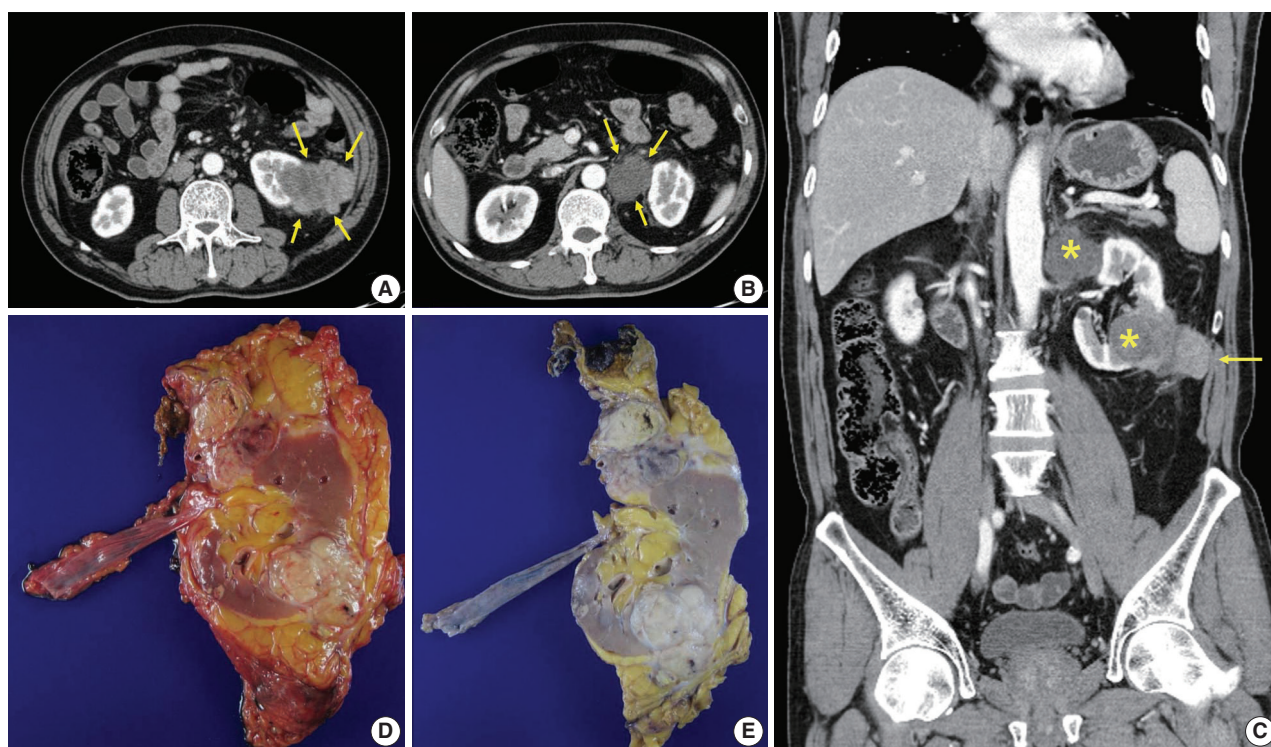


Fig. 1. Radiologic and gross features of the tumor. (A) Axial abdominopelvic computed tomography (CT) scan showing a 6.5-cm-sized heterogeneously enhancing exophytic and lobulated mass (arrows) in the lower pole of the left kidney. Mild fat infiltration is seen around the mass, and invasion of the Gerota's fascia is present. (B) Axial CT scan showing a 3.5-cm-sized mass (arrows) with homogeneously low density in the superior aspect of the left renal hilum. As the tumor compressed the kidney from the exterior, it was interpreted as a necrotic lymph node. (C) Coronally reformatted images of CT showing both masses (asterisks). The lower pole mass invaded the abdominal wall (arrow). (D, E) Surgical specimen before (D) and after (E) fixation. The kidney bore two well-circumscribed solid masses in the hilum near the upper pole and in the lower pole, measuring 4.5×3.5 cm and 7.0×4.1 cm, respectively. They were homogeneously yellowish-gray in color and firm with focal areas of hemorrhage and necrosis.

tions, these two large masses were homogeneously yellowish-gray in color and firm, with focal areas of hemorrhage and necrosis predominantly located in the central portion of the mass. The lower pole mass extended to the pelvicalyceal system and the Gerota's fascia. Renal vessels and the left adrenal gland were close to this tumor without direct contact. The hilar mass did not seem to arise from the renal parenchyma, but rather, it compressed the kidney from the outside. It was best considered a metastatic carcinoma to a lymph node.

Microscopically, the tumor was relatively well-defined, composed almost entirely of solid sheets of tumor cells, and separated by dense fibrous tissue at most interfaces. It had infiltrative borders on invasive fronts (Fig. 2A). Areas of necrosis were also present (Fig. 2B). Poorly cohesive, uniform round to polygonal epithelioid cells making solid sheets were seen in the main large mass on high power view. They had abundant densely eosinophilic cytoplasm with large eccentric nuclei, commonly known as rhabdoid features (Fig. 2C, D); nucleoli were prominent, and

mitoses were frequently seen. Lymphovascular invasion was present. Apart from the main mass, multiple small round nodules with papillary architecture were also seen (Fig. 2E, F, H). A transitional zone between papillary nodules and the main mass was not present on slides. The papillary nodules were considered separate lesions consistent with small papillary adenomas.

Immunohistochemical staining for multiple antigens was done to diagnose this tumor with uncommon morphology. Results are shown in Table 1. Tumor cells were immunohistochemically positive for CD10 and focally positive for epithelial membrane antigen, pan-cytokeratin, and vimentin, but negative for cytokeratin 7 and CD117. They were also negative for immune cell markers (such as leukocyte common antigen, CD3, CD20, CD138, and CD68) and muscular markers such as actin and desmin. The tumor cells were negative for HMB45 and CD99, ruling out the possibility of primitive neuroectodermal tumor/Ewing's sarcoma. Nuclear p53 was focally positive. After intra- and inter-departmental consultation, a diagnosis was made. The pathologic

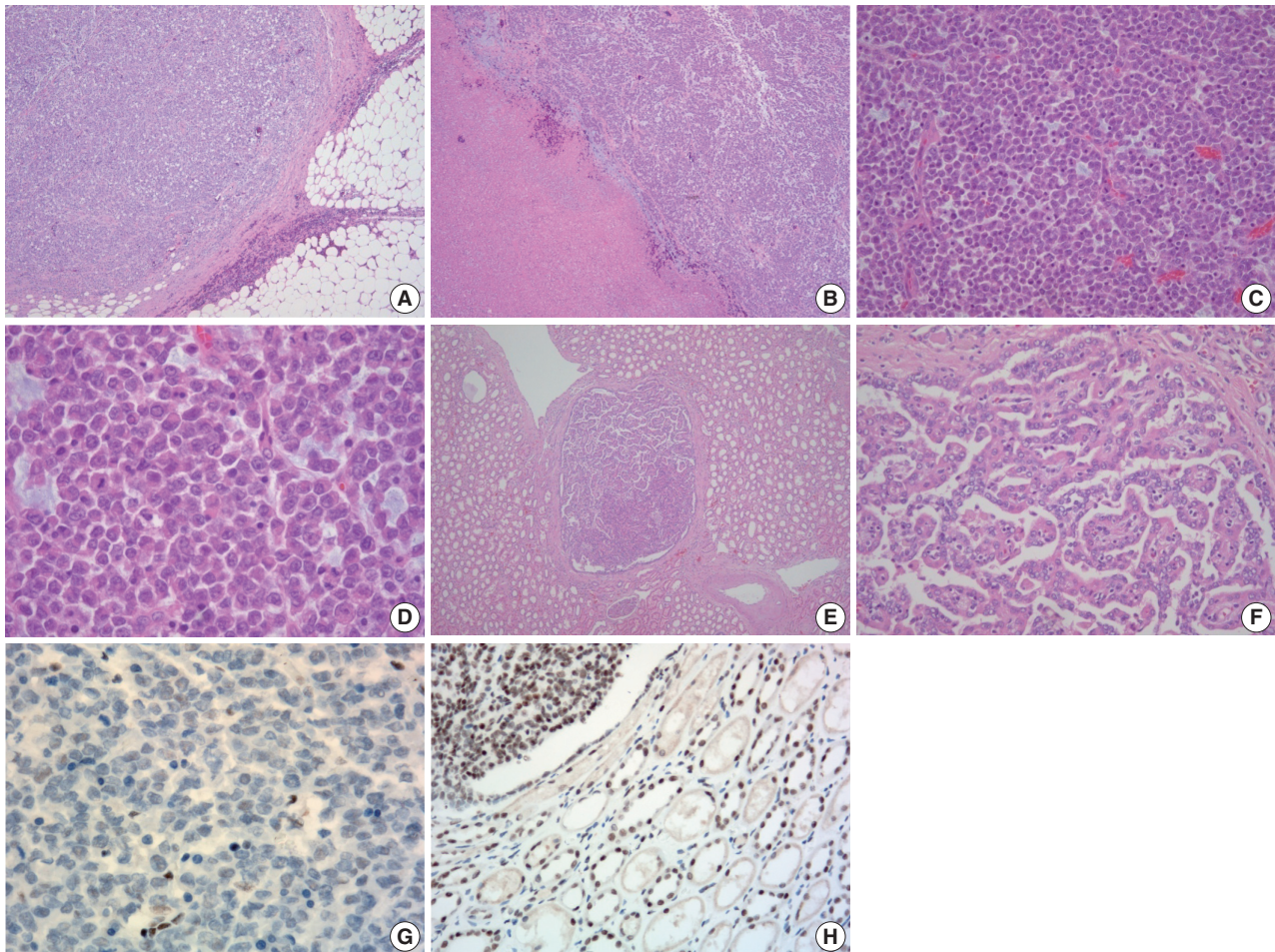


Fig. 2. Histologic and immunohistochemical features of the tumor. (A) Microscopically, the tumor was relatively well-defined and separated by dense fibrous tissue at most interfaces. (B) Areas of necrosis were present. (C) The tumor was composed almost entirely of solid sheets of tumor cells. (D) High power view revealing poorly cohesive uniform round to polygonal epithelioid cells. They had abundant densely eosinophilic cytoplasm with occasional round eosinophilic inclusion and large eccentric nuclei with irregular borders. Nucleoli were prominent. (E, F) Multiple small round nodules with papillary architecture were observed irrespective of the main mass. They were positive for cytokeratin 7 (not shown) and interpreted as papillary adenoma. (G) Tumor cells showing loss of immunoreactivity for integrase interactor 1 (INI-1; 1:100 dilution). (H) Retained immunoreactivity for INI-1 is shown in the normal renal tubular epithelium and papillary area (upper left) (1:100 dilution).

diagnosis for the large main mass in the lower pole at the time was RCC, unclassified with rhabdoid differentiation.

A year after the surgery, his follow-up CT scans showed a newly visible 6.5-cm-sized irregularly lobulated mass with heterogeneous enhancement abutting the left psoas muscle underlying the left nephrectomy site (Fig. 3A). This was considered a regional recurrence invading the left psoas muscle and the posterior aortic wall. After two months, the mass had increased in size. It also extended to the right aortic wall. Another operation to reduce the burden of this newly-developed mass was performed. The specimen sent for examination was a conglomeration of lymph nodes measuring $7.5 \times 6 \times 3.5$ cm in size and 86 g in weight (Fig. 3B). Cross-sections revealed whitish-tan solid and firm cut surfaces

with focal necrosis and hemorrhage (Fig. 3C). Microscopic findings were very similar to the previously resected unclassified RCC, showing solid sheets of rhabdoid cells effacing lymph nodes diffusely and infiltrating capsules to form a conglomerated mass (Fig. 3D–F). The pathologic diagnosis was metastatic carcinoma from the unclassified RCC with pericapsular soft tissue extension and necrosis.

To treat the remnant mass after the surgery, we referred the patient to the oncology department, where he was scheduled for palliative chemotherapy with temsirolimus. Infusions were given every 7 days for 4 weeks, which constituted one cycle. However, after the first infusion of the 4th cycle, he was unable to continue therapy due to the deterioration of his general condition. Upon

cessation, the tumor was aggravated. It had spread to the level IV lymph node of the neck and was pathologically confirmed as metastatic carcinoma. Unfortunately, after three weeks of palliative radiation therapy, the patient died.

Table 1. Results of immunohistochemical staining for tumor cells

Antigen	Result
EMA	Focally positive
Pan-cytokeratin	Focally positive
Vimentin	Focally positive
CD10	Positive
CD99	Negative
CK7	Negative
CD138	Negative
CD68	Negative
Leukocyte common antigen	Negative
CD3	Negative
CD20	Negative
Actin	Negative
Desmin	Negative
CD117	Negative
HMB-45	Negative
P53	Focally positive

EMA, epithelial membrane antigen; CK7, cytokeratin 7; HMB-45, human melanoma black 45.

In the present case, immunohistochemical staining for INI1 and genetic/molecular analysis was not performed at the time of diagnosis due to technical limitations. However, several studies have shown that specific molecular aberration involving switch/sucrose non-fermentable-related, matrix-associated, actin-dependent regulator of chromatin, subfamily B member 1 (*SMARCB1*, *hSNF5/INI1*) on chromosome 22, which can be identified by a lack of immunohistochemical staining with INI1, is a biomarker for malignant rhabdoid tumors [10]. Therefore, additional immunohistochemical staining and next-generation sequencing (NGS) were retrospectively performed to rule out the possibility of a malignant rhabdoid tumor.

We used the Axen cancer panel for NGS that included 535 SNV/InDel genes and 54 fusion genes. NGS revealed a novel mutation in the *SMARCB1* gene on chromosome 22 (c. 1047G>A, p.Trp349*). We further performed additional NGS for both normal and tumor tissues using a customized panel including 88 genes developed by our laboratory. The same result was obtained. Allele frequency was 81% in the tumor tissue and 49% in the normal tissue. The method for NGS was as follows. DNA was quantified using a Qubit 2.0 (Life Technologies, Burlington, Canada). Hybridization-based enrichment libraries were pre-

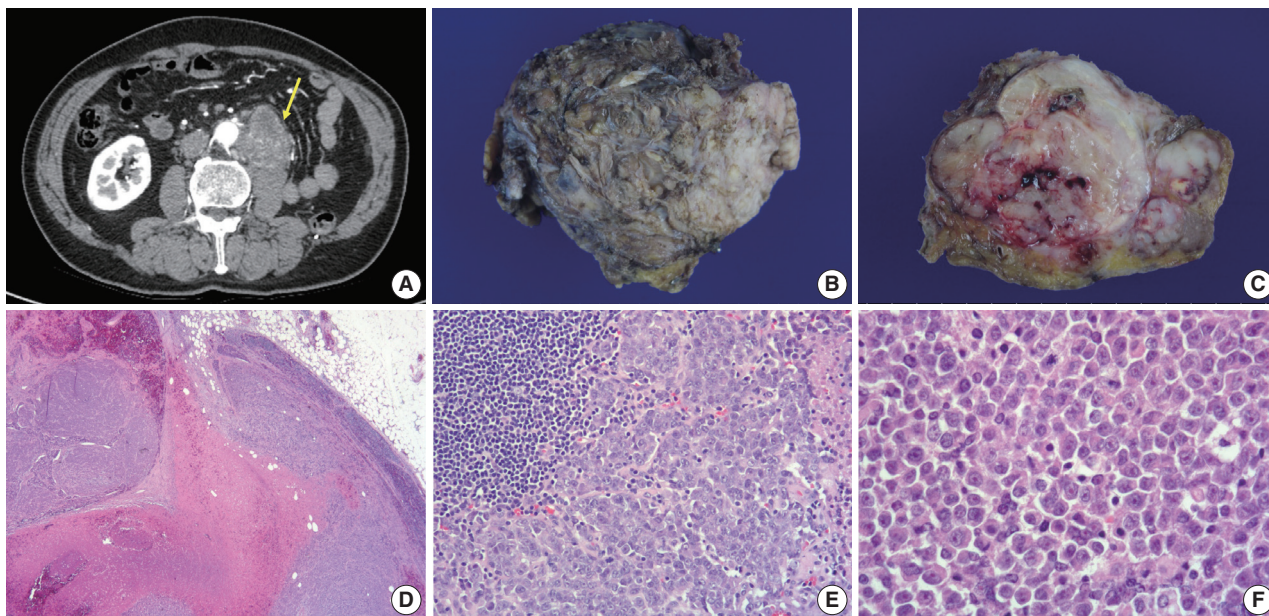


Fig. 3. Radiologic, gross, and histologic features of the newly-developed mass. (A) Follow-up axial abdominopelvic computed tomography scan a year after the surgery, revealing a newly visible 6.5-cm-sized heterogeneous enhancing lobulated mass (arrow) in the anterior aspect of the left psoas muscle underlying the left nephrectomy site, extending to the posterior aspect of the infrarenal abdominal aorta. Thus, aortic invasion was suspected. It was considered a recurrent tumor in the lymph nodes. (B) The specimen sent for examination was a conglomeration of lymph nodes (7.5×6×3.5 cm). (C) Whitish-tan solid and firm cut surfaces with areas of focal necrosis and hemorrhage were seen. (D) Solid sheets of tumor cells diffusely effacing lymph nodes and area of necrosis were seen. (E) Lymphoid tissue (upper left) and poorly cohesive round to polygonal tumor cells are shown. (F) Tumor cells had eosinophilic cytoplasm with occasional round eosinophilic inclusion and large eccentric nuclei with prominent nucleoli, resembling the former tumor from the kidney.

pared using a SureSelectXT Target Enrichment System for Illumina Paired-End Sequencing Library (Agilent Technologies, Palo Alto, CA, USA), following the manufacturer's protocol. Briefly, 200 ng of genomic DNA was fragmented, denatured, and hybridized with capture oligos during library preparation for high-throughput sequencing. Captured sequences were then enriched with streptavidin-conjugated paramagnetic beads and further amplified before being subjected to Illumina sequencing. Fragment sizes for all libraries were measured using a 2100 Bioanalyzer (Agilent Technologies). Then, qPCR was performed with a LightCycler 480 System (Roche Diagnostics, Indianapolis, IN, USA) using a Kapa library quantification kit (KK4854, KAPA Biosystems, Wilmington, MA, USA). Sequencing was performed using an Illumina NextSeq500 platform with an average read length of 2×150 bp per the manufacturer's instructions.

Tumor cells showed a loss of INI1 expression (Fig. 2G). It is known that renal medullary carcinoma can also be entirely solid with sheet-like architecture or with exclusively rhabdoid morphology. It has also been reported that renal medullary carcinoma with rhabdoid features shows the absence of INI1 expression [11]. However, the tumor showed no immunohistochemical staining for PAX8 and PAX2, suggesting it was not from a renal epithelial origin. From a retrospective point of view, all morphologic, immunohistochemical, and molecular findings were sufficient for the diagnosis of MRT of the kidney. Our revised diagnosis of this tumor was MRT of the kidney. The bad prognosis of this patient was compatible with that seen in this tumor group.

DISCUSSION

NGS identified a novel nonsense mutation, c.1047G > A in exon 8/9 of the *SMARCB1* gene, caused by p.Trp349*. This mutation halted the translation of the INI1 protein, a hallmark of MRT. Rhabdoid cells were first described by Gokden et al. [12] in the adult kidney. Rhabdoid cells have been described as variably cohesive epithelioid cells with eccentrically located vesicular nuclei with prominent nucleoli. Large intracytoplasmic eosinophilic hyaline globules are their characteristics. They resemble rhabdomyoblasts but differ from rhabdomyoblasts in that they do not show rhabdomyoblastic differentiation immunohistochemically or ultrastructurally [12]. MRT occurs mainly in the kidney of children less than 1 year of age. It is rare and has an aggressive clinical course [1]. Renal MRT was originally described as a "rhabdomyosarcomatoid variant of Wilms tumor" by Beckwith and Palmer [13] in 1978. However, after Versteeg et al. [14] demonstrated potentially inactivating mutations or de-

letions of both alleles of the *INI1* gene in almost all renal and pure extrarenal MRTs, they were regarded as a distinct entity with a specific molecular pathogenesis. The deletion of 22q11.2 and the mutation of *hSNF5/INI1*, encoding a chromatin-remodeling protein with the potential to alter global transcription patterns, are strongly associated with the development of a rhabdoid tumor phenotype [14,15].

One unique aspect of the present case was the presentation of a rhabdoid tumor of the kidney in an adult. Until recently, only a few cases have been reported on a pure rhabdoid tumor of the kidney in adults. In one study, germline mutation of *hSNF5/INI1* in humans and its deletion in knock-out mice resulted in rhabdoid tumors developing at an early age [15]. Shannon et al. [16] have mentioned that this might be why pure rhabdoid tumors of the kidney are seldom reported in adults. Their study found identical *VHL* mutations in both clear cell and rhabdoid components of composite tumors in two patients. They argued that some rhabdoid tumors might arise from clear cell RCCs. They also mentioned the possibility of a sporadic biallelic inactivation of the gene(s) involved in the development of a rhabdoid phenotype taking place in genetically unstable tumor cells of a preexisting neoplasm [16]. If that is the case, a continuum might exist between an RCC with rhabdoid features and MRT of the kidney. As molecular and genetic studies were not done for the rhabdoid tumor cases of the aforementioned study, immunohistochemical staining for INI1 and genetic testing for the *SMARCB1/INI1* gene should be performed for more cases of RCCs with rhabdoid features and malignant rhabdoid tumors of the kidney of adults to prove the diagnosis.

To obtain papers on MRT of the adult kidney, we searched for previously published case reports in PubMed. Among the results, we found eight case reports of pure MRT of the native kidney arising in an adult patient that was written in English [2-9]. Clinicopathologic characteristics of the cases are summarized in Tables 2 and 3 [2-9]. Age at diagnosis ranged from 32 to 79 years, and sex predominance was not noted. Two cases occurred in Asians, and five cases were presented in Caucasians. The race of the patient in the remaining case report was not recorded. Their initial symptoms were either related to the mass effect or metastasis. The maximal dimension of the mass varied from 3.5 to 12 cm. All cases except three underwent radical nephrectomy. Most of them showed bad outcomes. One case with pulmonary metastasis was treated with interleukin-2 (IL-2) therapy and showed an exceptionally better outcome than others. In another case, chemotherapy, including IL-2, failed [4,5]. Common pathologic findings were as follows. First, they showed solid sheets of

Table 2. Clinical features of malignant rhabdoid tumors of the kidney in adults reported in the literature

Study	Year	Age/Race	Sex	Initial symptom	Size (cm)	Location	Management	Outcome	Medical history
Lowe et al. [2]	1990	32/Caucasian	F	Right flank pain (3 days)	12	Rt. lower	Radical nephrectomy	Multiple metastases (3 mo after the diagnosis), declined further therapy	Meningocele, amniotic bands, hydronephrosis
Clausen et al. [3]	1994	NA/Caucasian	F	NA	NA	NA	NA	NA	NA
Ebbinghaus et al. [4]	1995	56/Caucasian	M	Persistent, non-productive cough (6 mo)	6 x 9	Lt.	Floxuridine (5 mo), interferon-alpha (3 mo), IL-2 (2 discontinued due to angina pectoris)	Good performance (over 18 mo from the diagnosis and 9 months after IL-2 therapy cessation)	CABG due to atherosclerotic coronary artery disease (10 yr)
Peng et al. [5]	2003	38/Caucasian	F	Left flank pain (10 days)	8 x 5	Lt. upper to mid	Radical nephrectomy, several courses of chemotherapy including IL-2	Chemotherapy: failed (died 5 mo after surgery)	-
Zhao et al. [6]	2013	59/Asian (Chinese)	M	Weight loss of 6 kg (several months)	5 x 4 x 5	Lt. lower	Radical nephrectomy	A 10 mo postoperative follow up revealed no indications of tumor recurrence or metastasis	-
Poddaturi et al. [7]	2014	60/Caucasian	M	Progressive fatigue and abdominal distension (6 mo), worsening dyspnea (2 wk)	3.5 x 2.5 x 2	Lt. mid to lower	Radical nephrectomy, retroperitoneal lymph node dissection	Died during reoperation	Hypothyroidism, hypertension, chronic obstructive pulmonary disease
Okumura et al. [8]	2019	79/Asian (Japanese)	F	Pain in the right buttock and difficulty in ambulation	6.4 x 4.8	Lt. upper	Treated with axitinib	Died 5 mo after the first hospital visit (3.5 mo after the treatment initiation)	Cerebral infarction at the age of (15 yr)
Ayari et al. [9]	2019	65/NA	M	Right flank pain with progressive fatigue, a weight loss of 5 kg, abdominal distention (1 mo)	5.6 x 5.3	Rt.	None (died before therapeutic decision)	Died few days after the diagnosis	Hypertension, renal calculi, Lt. nephrectomy for hydronephrotic kidney (20 yr)

F, female; Rt., right; NA, not applicable; M, male; IL-2, interleukin-2; CABG, coronary artery bypass graft; Lt., left.

Table 3. Pathologic features of malignant rhabdoid tumors of the kidney in adults reported in the literature

Study	Year	Gross feature	Extension/Metastasis	IHC
Lowe et al. [2]	1990	Poorly demarcated, solid, hemorrhagic	Extended beyond Gerota's fascia densely adherent to the duodenum and the colon	Keratin (AE1/AE3), vimentin: (+) EMA: focally (+) Desmin, myoglobin, muscle-type actin: (-) NA
Clausen et al. [3]	1994	NA	NA	NA
Ebbinghaus et al. [4]	1995	Only biopsy done	Multiple metastasis to bilateral lungs	Vimentin: focally (+) Desmin, S-100 protein or HMB-45 (-) CK: weak (+)
Peng et al. [5]	2003	White to grayish tan and flesh, focal areas of necrosis	Invaded renal pelvis, calyces, the perihilar and perirenal adipose tissue, extended to the capsule, enlarged hilar lymph node	Vimentin: diffuse (+) EMA, NSE, S-100: focal (+) p53: focal nuclear (+) Keratin (AE1/AE3, CAM5.2, CK7, and CK20): (-) CEA, SMA, myoglobin, light chains, HMB-45, MART-1: (-) Mucin: (-) Lymphoma markers: (-) Ki-67 (MIB-1): >95%
Zhao et al. [6]	2013	White to gray with a fleshy texture, focal areas of necrosis and hemorrhage	Focal invasion into capsule, retroperitoneal and left costophrenic angle lymph node metastases, metastasis to left lung	Vimentin: diffusely (+) NSE, S-100, EMA: focally (+) Pancytokeratin, CK7, myoglobin, desmin, MSA, and SMA: (-)
Podduturi et al. [7]	2014	Poorly circumscribed, soft tan lesion, numerous tan-gray nodules within perinephric and renal sinus	Extended from the hilum to the cortex, metastasis to bilateral lungs	Vimentin, pan-CK: strong (+) Desmin, myoglobin, S-100, melanoma cocktail, TTF-1, CK7, CK20, CDX2, PAX8, CD31, CD34, factor VIII, CD30, CD45: (-) INI-1: (-)
Okumura et al. [8]	2019	Only biopsy done	Multiple metastatic bone and lymph node lesions	Vimentin, EMA, CAM5.2, p53: (+) CK, CD10: focally (+) INI1, CK7, CK20, AMACR, S100, CD45, RCC marker, ALK, α -SMA, desmin, MyoD, myogenin, HMB45, melan A: (-)
Ayari et al. [9]	2019	Only biopsy done	Voluminous lymph nodes along the paraaortic region, compressing the inferior vena cava	Vimentin: strongly (+) Myoglobin, desmin, SMA: (-)

IHC, immunohistochemistry; EMA, epithelial membrane antigen; NA, not applicable; HMB-45, human melanoma black 45; CK, cytokeratin; NSE, neuron-specific enolase; CEA, carcinoembryonic antigen; SMA, smooth muscle actin; MSA, muscle specific actin; TTF-1, thyroid transcription factor-1; INI-1, integrase interactor 1; AMACR, α -methylacyl-CoA racemase; RCC, renal cell carcinoma; ALK, anaplastic lymphoma kinase;

non-cohesive cells with eccentric nuclei and large round eosinophilic cytoplasmic inclusion-like structures. Second, for cases that included an assessment of ultrastructure, large cytoplasmic whorls of intermediate filaments were present. Third, tumor cells were consistently immunohistochemically reactive for vimentin, either focally or diffusely, while they variably expressed cytokeratin and epithelial membrane antigen. These morphological, immunohistochemical, and clinical findings were consistent with previously described characteristics of MRT of the kidney by Wick et al. [17]. However, molecular or genetic investigation concerning the *SMARCB1* gene was not performed for any of the patients. Immunohistochemical staining for INI1 was performed for only one patient.

Pediatric rhabdoid tumor of the kidney has been regarded as a distinct neoplasm, whereas rhabdoid differentiation in adult RCC is usually found in association with conventional (clear cell) tumors, from which it is thought to evolve [16]. In a retrospective analysis of 480 renal tumors conducted by Gokden et al. [12], 23 RCCs with rhabdoid features were found, all of which

had at least 50% of the non-rhabdoid carcinoma components described as conventional (clear cell) RCC. The rhabdoid component was assumed to have arisen from the conventional RCC area [12]. Shannon et al. [16], on the other hand, reported 5 RCCs with rhabdoid differentiation, with three of them being composite tumors and two of them having rhabdoid elements only (which they called pure rhabdoid tumors). Several authors have described that loss of INI1 is helpful to differentiate MRT from other composite tumors, including primary renal neoplasms with rhabdoid differentiation where the expression of INI1 is retained [12,18,19].

Consistent with the role of *SMARCB1* as a tumor suppressor gene, tumors can arise following the inactivation of both *SMARCB1* alleles. While the majority of tumors are histologically classified as rhabdoid tumors, the loss of *SMARCB1* expression has also been observed in other tumors, including epithelioid sarcoma, renal medullary carcinoma, undifferentiated pediatric sarcomas, and a subset of hepatoblastomas. It has been previously estimated that 15% to 20% of all rhabdoid tumors are caused by germline mutations of *SMARCB1*.

Although the present case's initial diagnosis was undifferentiated RCC with rhabdoid features, there was a difference between this case and previously published cases of RCC with rhabdoid features. Unlike previously reported cases, the present case did not have any area with features of conventional RCC. There was no transition zone between the undifferentiated rhabdoid area and the classical RCC area, usually seen in RCC with rhabdoid features [12]. In practice, however, the rhabdoid area of RCC in adults is frequently viewed as a dedifferentiated area rather than raising the possibility for a diagnosis of malignant rhabdoid RCC. Indeed, some authors in the past have argued that pure extrarenal MRT in older patients might merely be poorly differentiated neoplasms with pseudo-rhabdoid features [20]. In addition, MRT of the kidney has been reported only in a limited number of adults at present, while more reports have discussed RCC with rhabdoid features. Furthermore, a small RCC component might have been missed during sampling. These altogether led to a faulty diagnosis of undifferentiated RCC with rhabdoid features.

In the present case, all morphologic, immunohistochemical, and molecular findings supported an MRT of the kidney. To the best of our knowledge, the present case is the first reported case of MRT of the native kidney in an adult, demonstrating both the loss of INI1 expression and the mutation of the *SMARCB1* gene. This case points out again that MRT should no longer be considered merely a childhood tumor entity but rather a tumor that can also develop in adults. As a result, when an undifferentiated area with rhabdoid morphology is found in an adult tumor, one should initially look for areas showing classical morphological features of tumors that commonly arise in the affected organ. If these features are found, the transition zone between the two areas would be helpful to determine whether the rhabdoid area is the dedifferentiated area of the original tumor. If not found, additional sampling of the tumor with thorough inspection might be needed. When it comes to the conclusion that the tumor consists entirely of rhabdoid cells, immunohistochemical staining for INI1 and molecular or genetic investigation of the *SMARCB1/INI1* gene on chromosome 22 could be helpful to diagnose an MRT in an adult.

Ethics Statement

The study protocol conformed to the ethical guidelines of the World Medical Association Declaration of Helsinki and was approved by the Institutional Review Board of Soonchunhyang University Bucheon Hospital (IRB No 2017-11-018). The IRB approved this study as a waiver of patients consent because it met all of the following criteria: (1) The risk of doing the research is not greater than the minimum risk; (2) The right to receive the study subject or the welfare will not be infringed due to the exemption of consent; (3) The study cannot be carried out without actual exemption from consent.

ORCID

Eunkyung Han <https://orcid.org/0000-0003-1697-3336>
 Jiyeon Kim <https://orcid.org/0000-0002-6126-227X>
 Min Jung Jung <https://orcid.org/0000-0001-8870-5475>
 Susie Chin <https://orcid.org/0000-0003-2754-1483>
 Sang Wook Lee <https://orcid.org/0000-0001-9660-4092>
 Ahrim Moon <https://orcid.org/0000-0002-3450-4915>

Author Contributions

Conceptualization: AM. Investigation: EH, JK, MJJ, SC, SWL. Writing—original draft preparation: EH. Writing—review and editing: AM.

Conflicts of Interest

The authors declare that they have no potential conflicts of interest.

Funding Statement

This work was supported by a grant (NRF-2017R1C1B5075679) of the National Research Foundation (NRF) funded by the Korea government (MEST). It was also supported by Soonchunhyang University Research Fund. The authors have disclosed that they have no significant relationships with or financial interest in any commercial companies pertaining to this article.

References

- Schmidt D, Harms D, Zieger G. Malignant rhabdoid tumor of the kidney. Histopathology, ultrastructure and comments on differential diagnosis. *Virchows Arch A Pathol Anat Histopathol* 1982; 398: 101-8.
- Lowe W, Weiss RM, Todd MB, True LD. Malignant rhabdoid tumor of the kidney in an adult. *J Urol* 1990; 143: 110-1.
- Clausen HV, Horn T, Anagnostaki L, Larsen S. Malignant rhabdoid tumour of the kidney in an adult: a case report with immunohistochemical and ultrastructural investigation. *Scand J Urol Nephrol Suppl* 1994; 157: 123-8.
- Ebbinghaus SW, Herrera G, Marshall ME. Rhabdoid tumor of the kidney in an adult: review of the literature and report of a case responding to interleukin-2. *Cancer Biother* 1995; 10: 237-41.
- Peng HQ, Stanek AE, Teichberg S, Shepard B, Kahn E. Malignant rhabdoid tumor of the kidney in an adult: a case report and review of the literature. *Arch Pathol Lab Med* 2003; 127: e371-3.
- Zhao G, Na R, Yang Y, Han R. Pure malignant rhabdoid tumor of the left kidney in an adult: a case report and review of the literature. *Oncol Lett* 2013; 5: 1481-4.
- Poddaturi V, Campa-Thompson MM, Zhou XJ, Guileyardo JM. Malignant rhabdoid tumor of the kidney arising in an adult patient. *Proc (Bayl Univ Med Cent)* 2014; 27: 239-41.
- Okumura Y, Adachi Y, Shirahase T, et al. Malignant rhabdoid tumor in an adult kidney: a case report. *Mol Clin Oncol* 2019; 11: 55-8.
- Ayari Y, Ben Rhouma S, Boussaffa H, et al. Malignant rhabdoid tumor in a solitary kidney arising in an adult patient with chronic obstructive renal calculi. *Int J Surg Case Rep* 2019; 58: 85-7.
- Sultan I, Qaddoumi I, Rodriguez-Galindo C, Nassan AA, Ghandour K, Al-Hussaini M. Age, stage, and radiotherapy, but not primary tumor site, affects the outcome of patients with malignant rhabdoid tumors. *Pediatr Blood Cancer* 2010; 54: 35-40.
- Cheng JX, Tretiakova M, Gong C, Mandal S, Krausz T, Taxy JB. Renal medullary carcinoma: rhabdoid features and the absence of INI1 expression as markers of aggressive behavior. *Mod Pathol*

- 2008; 21: 647-52.
12. Gokden N, Nappi O, Swanson PE, et al. Renal cell carcinoma with rhabdoid features. *Am J Surg Pathol* 2000; 24: 1329-38.
 13. Beckwith JB, Palmer NF. Histopathology and prognosis of Wilms tumors: results from the First National Wilms' Tumor Study. *Cancer* 1978; 41: 1937-48.
 14. Versteeg I, Sevenet N, Lange J, et al. Truncating mutations of hSNF5/INI1 in aggressive paediatric cancer. *Nature* 1998; 394: 203-6.
 15. Roberts CW, Galusha SA, McMenamin ME, Fletcher CD, Orkin SH. Haploinsufficiency of Snf5 (integrase interactor 1) predisposes to malignant rhabdoid tumors in mice. *Proc Natl Acad Sci U S A* 2000; 97: 13796-800.
 16. Shannon B, Stan Wisniewski Z, Bentel J, Cohen RJ. Adult rhabdoid renal cell carcinoma. *Arch Pathol Lab Med* 2002; 126: 1506-10.
 17. Wick MR, Ritter JH, Dehner LP. Malignant rhabdoid tumors: a clinicopathologic review and conceptual discussion. *Semin Diagn Pathol* 1995; 12: 233-48.
 18. Perry A, Fuller CE, Judkins AR, Dehner LP, Biegel JA. INI1 expression is retained in composite rhabdoid tumors, including rhabdoid meningiomas. *Mod Pathol* 2005; 18: 951-8.
 19. Przybycin CG, McKenney JK, Reynolds JP, et al. Rhabdoid differentiation is associated with aggressive behavior in renal cell carcinoma: a clinicopathologic analysis of 76 cases with clinical follow-up. *Am J Surg Pathol* 2014; 38: 1260-5.
 20. Weeks DA, Beckwith JB, Mierau GW. Rhabdoid tumor: an entity or a phenotype? *Arch Pathol Lab Med* 1989; 113: 113-4.

Multiple hepatocyte nuclear factor 1A (HNF1A)-inactivated hepatocellular adenomas arising in a background of congenital hepatic fibrosis

Yangkyu Lee¹, Hyunjin Park², Kyoungbun Lee³, Youngeun Lee³, Kiryang Lee³, Haeryoung Kim³

¹Department of Pathology, Seoul National University Bundang Hospital, Seoul National University College of Medicine, Seongnam;

²Department of Pathology, Gangnam Severance Hospital, Yonsei University College of Medicine, Seoul;

³Department of Pathology, Seoul National University Hospital, Seoul National University College of Medicine, Seoul, Korea

Hepatocellular adenomas (HCAs) are benign hepatocellular neoplasms with distinct molecular subtypes [1,2]. Hepatocyte nuclear factor 1A (*HNF1A*)-inactivated hepatocellular adenoma (H-HCA) occupies about 35% of all HCAs [1,2]. H-HCA demonstrates somatic (90%) or germline (10%) inactivating mutations of *HNF1A* gene, which encodes a transcription factor involved in several metabolic pathways of hepatocytes, and inactivation of *HNF1A* promotes lipogenesis [3]. Clinically, H-HCAs occur predominantly in females, are frequently associated with oral contraceptives, and a subset of H-HCA with germline *HNF1A* mutations is associated with maturity-onset diabetes type 3 (MODY3). Morphologically, H-HCAs frequently show steatosis and loss of liver fatty acid-binding protein (LFABP) expression in the tumor cells [1,2].

Here, we report a rare case of a young male patient with multiple H-HCAs in a background of congenital hepatic fibrosis (CHF).

CASE REPORT

A 25-year-old man was admitted to the hospital for liver transplantation for multiple hepatic masses that were incidentally discovered by imaging. He had previously been diagnosed with CHF on liver biopsy 14 years ago, and had received transjugular intrahepatic portosystemic shunt for portal hypertension at that time. He had no history of metabolic syndrome, al-

cohol intake or prior intake of androgens and his body mass index was 25.2 kg/m². There was no evidence of other abnormalities associated with CHF, and there was no remarkable family history. Preoperative liver function tests were as follows: aspartate aminotransferase 35 U/L, alanine aminotransferase 29 U/L, gamma-glutamyl transferase 19 U/L, alkaline phosphatase 79 U/L, total bilirubin 4.2 mg/dL, and direct bilirubin 1.3 mg/dL. Serological tests for hepatitis B and C virus were negative. On computed tomography, there were multiple fat-containing nodules in both hepatic lobes.

The liver weighed 1,242 g, and sections revealed nine discrete tan-to-yellow nodules in both lobes, measuring 9.5×6.5×7.5 cm in the largest one. The background liver was firm with a reticular appearance (Fig. 1). On microscopic examination, the background liver showed the typical histological features of CHF: broad fibrous bands rimmed by small bile ductular structures with ductal plate malformation patterns (Fig. 1). The pathological findings of the nine nodules are summarized in Table 1 and Figs. 2 and 3. Six nodules were diagnosed as H-HCAs and the three smaller nodules as large regenerative nodule (LRN) or focal nodular hyperplasia (FNH)-like nodules, based on the histopathological and immunohistochemical characteristics. Notably, although LFABP loss was seen in all six H-HCAs, nodules #1, #2, and #9 showed only patchy mild steatosis, and nodules #1 and #2 also demonstrated focal peliosis and mild ductular reaction. The remaining 4 H-HCAs demonstrated diffuse steatosis. On follow-up, the patient is currently well without evidence of recurrence.

Received: September 15, 2020 Revised: November 9, 2020

Accepted: November 12, 2020

Corresponding Author: Haeryoung Kim, MD, PhD

Department of Pathology, Seoul National University Hospital, Seoul National University College of Medicine, 103 Daehak-ro, Jongno-gu, Seoul 03080, Korea
 Tel: +82-2-740-8322, Fax: +82-2-765-5600, E-mail: haeryoung.kim@snu.ac.kr

DISCUSSION

To our knowledge, this is the second reported case of H-

HCA arising in a background of CHF. Hepatocellular nodules, including FNH and FNH-like nodules, HCAs and even hepatocellular carcinomas (HCCs), have been demonstrated to occur in the setting of hepatic vascular abnormalities, such as Budd-Chiari syndrome and congenital extrahepatic portosystemic

shunts [4-8]. While CHF belongs to a group of fibropolycystic diseases of the liver that affects the biliary system, portal hypertension dominates the clinical presentation of this disease, as the number of portal vein branches is often reduced [9]. Treatment of CHF with portosystemic shunt surgery may also add to the

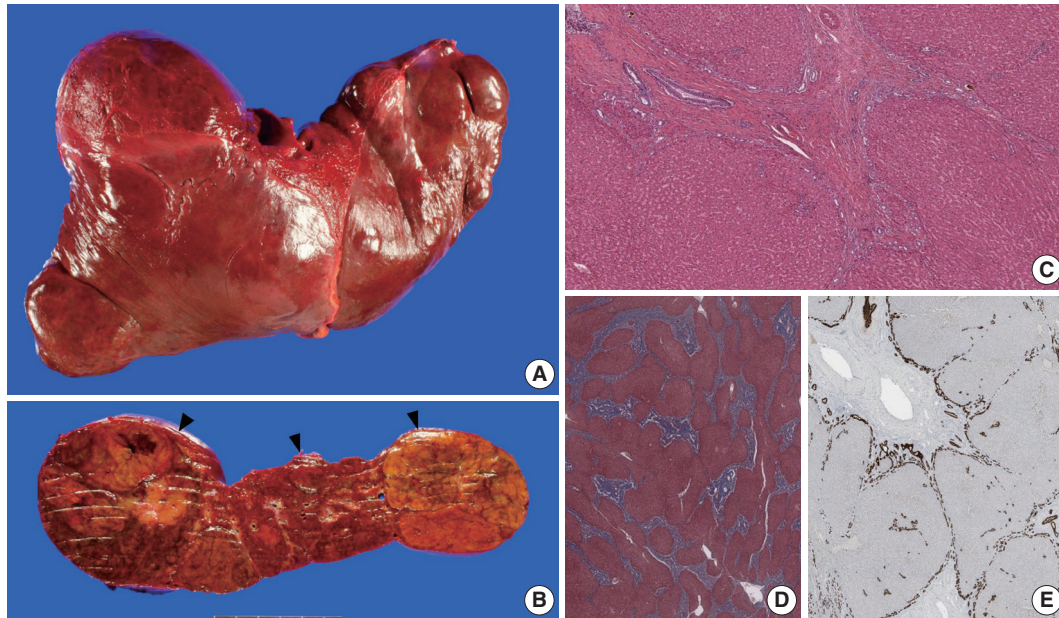


Fig. 1. (A–C) Gross findings. (A) The explanted liver is distorted in shape due to the multiple bulging masses. (B) A representative section reveals three lobulated nodules (arrowheads). The nodules are lobulated, well-demarcated but non-encapsulated, with focal hemorrhage and peliosis. (C) On microscopy, the background liver shows broad fibrous bands lined by ductal structures with ductal plate malformation pattern and inspissated bile. (D) Masson's trichrome stain reveals the jigsaw-puzzle pattern biliary fibrosis. (E) Cytokeratin 7 immunostain highlights the ductular structures at the interface between the fibrous bands and the hepatic lobules.

Table 1. Summary of the pathological features of the hepatic nodules in this case

No.	Location (segment)	Size (cm)	Diagnosis	Histopathological feature	Immunohistochemical stain result
1	S7	9.5	H-HCA	Patchy steatosis, focal peliosis, bile ductules	LFABP loss, SAA/CRP/GS negative, membranous β -catenin expression
2	S6	6.6	H-HCA	Patchy steatosis, focal peliosis, bile ductules	LFABP loss, SAA/CRP/GS negative, membranous β -catenin expression
3	S1	3.5	H-HCA	Diffuse steatosis	LFABP loss, SAA/CRP/GS negative, membranous β -catenin expression
4	S4	4.5	H-HCA	Diffuse steatosis	LFABP loss, SAA/CRP/GS negative, membranous β -catenin expression
5	S4	1.0	LRN	Fibrous septa with bile ductules	No LFABP loss, focal SAA/CRP expression, GS negative, membranous β -catenin
6	S4	1.0	FNH-like nodule	Fibrous septa with bile ductules	No LFABP loss, focal SAA/CRP expression, patchy GS expression, membranous β -catenin
7	S2	9.5	H-HCA	Diffuse steatosis	LFABP loss, SAA/CRP/GS negative, membranous β -catenin expression
8	S2	0.9	FNH-like nodule	Fibrous septa with bile ductules	No LFABP loss, focal SAA/CRP expression, patchy GS expression, membranous β -catenin
9	S6	1.6	H-HCA	Focal mild steatosis	LFABP loss, SAA/CRP/GS negative, membranous β -catenin expression

H-HCA, Hepatocyte nuclear factor 1A-inactivated hepatocellular adenoma; LFABP, liver fatty acid-binding protein; SAA, serum amyloid A; CRP, C-reactive peptide; GS, glutamine synthetase; LRN, large regenerative nodule; FNH-like nodule, focal nodular hyperplasia-like nodule.

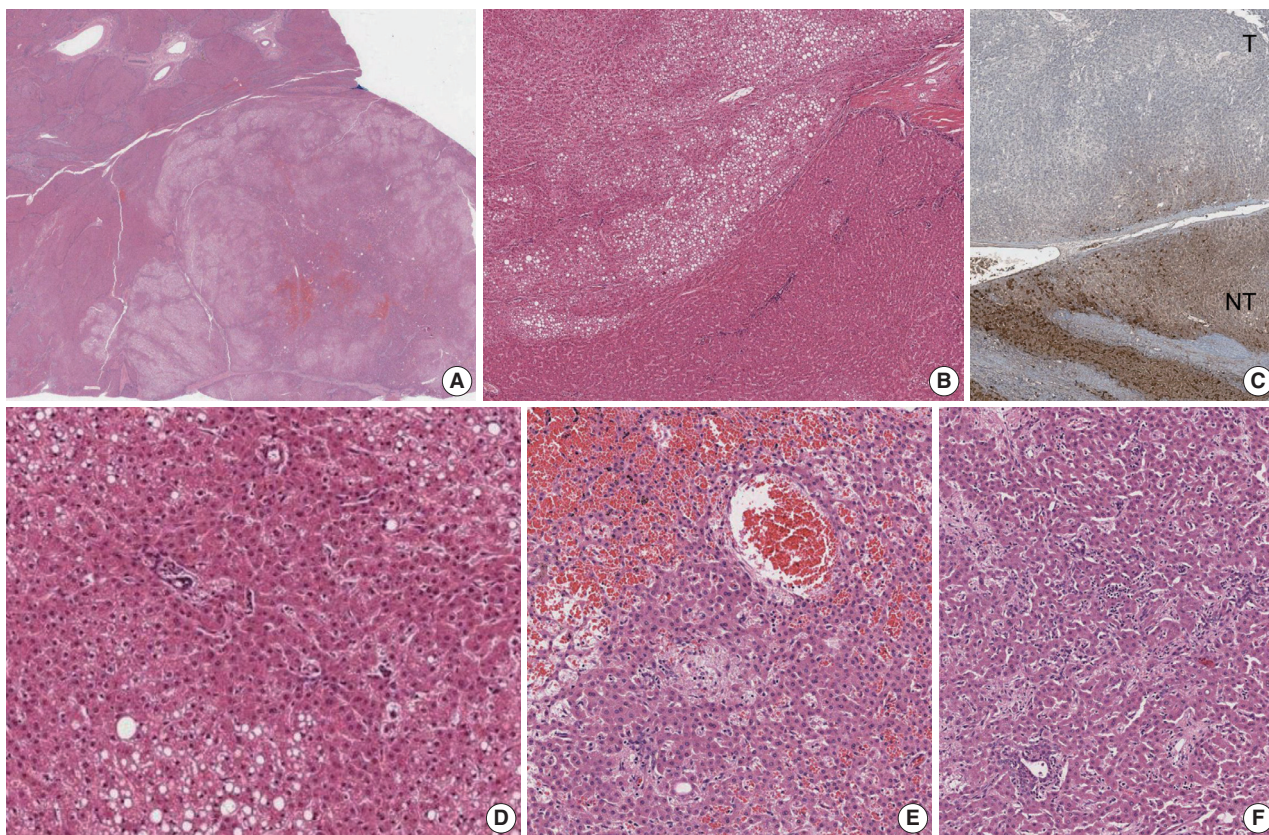


Fig. 2. The histopathological and immunohistochemical features of this case. (A) Scanning power view demonstrates a well-demarcated and non-encapsulated solid mass (lower right). (B) The peripheral portion of the tumor shows patchy macrovesicular steatosis. (C) Loss of liver fatty acid-binding protein expression is seen in the tumor (T, tumor; NT, non-tumor). (D) Higher power magnification of the hepatocellular adenoma, demonstrating the patchy macrovesicular steatosis and unpaired arteries. (E) No significant cytoarchitectural atypia is present. The central portion of nodule #1 demonstrates focal sinusoidal dilatation with congestion and peliosis. (F) A few pseudoportal tracts are seen in nodule #1, containing clusters of bile ductules.

abnormal heterogeneous vascularity in the parenchyme [10]. As a result, the uneven hepatic perfusion may give rise to the formation of hepatocellular nodules. However, although this vascular concept explains the pathogenesis of reactive hyperplastic hepatocellular nodules such as FNH and LRN/FNH-like nodules, the relationship between this vascular abnormality and the occurrence of neoplastic hepatocellular nodules is still not well understood. Indeed, the neoplastic nature of smaller hepatocellular nodules resembling HCAs (previously referred to as “adenoma-like” nodules or adenomatous hyperplasia) arising in vascular disorders have been questioned, due to the morphological overlap with LRNs and FNH-like nodules and their frequent co-existence within the same liver [4]. However, as the molecular classification of HCAs has been better characterized over the past decade, immunohistochemical stains have facilitated the diagnosis of HCAs [7]. Interestingly, Sempoux et al. [7] described three cases of H-HCAs arising in backgrounds of hepatic vascular disorders

which were either associated with HCCs or contained atypical foci. This is a notable finding as it implies that H-HCAs associated with vascular disorders may be at increased risk of malignant transformation, in contrast to those arising in “conventional” settings (e.g., females, oral contraceptives, MODY3, etc) [2]. Another interesting finding is that H-HCAs in the context of hepatic vascular disorders often demonstrated a lack of intratumoral steatosis, which differs from the characteristic histology (diffuse steatosis) of typical H-HCAs [7]. Indeed, in our case, three H-HCAs demonstrated only focal mild steatosis, and the diagnosis was rendered based on the loss of LFABP expression.

Although further validation would be required, the identification of nodular lesions on imaging in the liver of patients with CHF or hepatic vascular disorders may warrant histological examination to rule out the possibility of HCCs or HCAs. In addition, H-HCAs arising in the context of hepatic vascular disorders may not be associated with the typical clinicopathological fea-

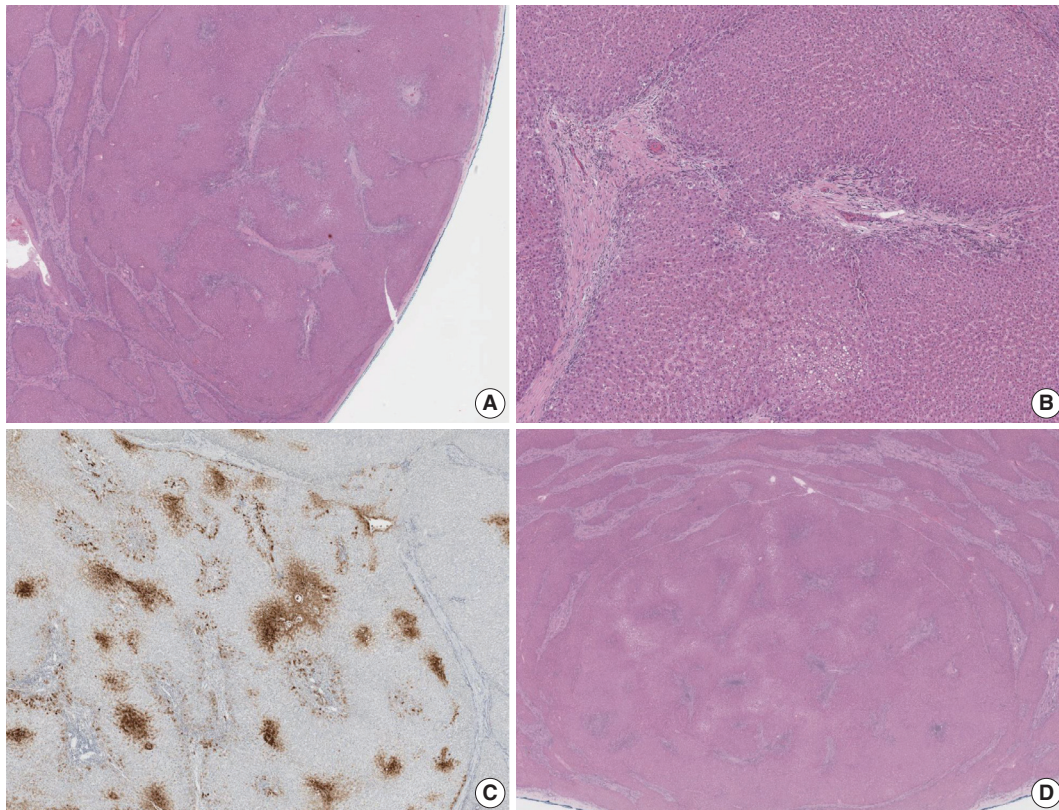


Fig. 3. Smaller focal nodular hyperplasia-like nodules were seen (A–C) with small fibrous scars containing thick-walled blood vessels and patchy non-map-like glutamine synthetase expression. Fibrous septa were also seen in a large regenerative nodule but the central scar-like fibrous tissue was less prominent (D).

tures, such as steatosis and low risk of malignant transformation.

Ethics Statement

This case study was approved by the Institutional Review Board of Seoul National University Hospital (#H-1809-141-975) and informed consent was waived.

ORCID

Yangkyu Lee <https://orcid.org/0000-0002-6008-7713>
 Hyunjin Park <https://orcid.org/0000-0001-7193-9849>
 Kyoungbun Lee <https://orcid.org/0000-0001-8427-3003>
 Youngeun Lee <https://orcid.org/0000-0002-0000-1615>
 Kiryang Lee <https://orcid.org/0000-0003-3769-001X>
 Haeryoung Kim <https://orcid.org/0000-0002-4205-9081>

Author Contributions

Conceptualization: YL (Yangkyu Lee), HK. Funding acquisition: HK. Investigation: YL (Yangkyu Lee), HK. Supervision: HK. Writing—original draft: YL (Yangkyu Lee). Writing—review & editing: YL (Yangkyu Lee), HP, KL, YL (Youngeun Lee), KL, HK. Approval of final manuscript: all authors.

Conflicts of Interest

H.K., a contributing editor of the *Journal of Pathology and Translational Medicine*, was not involved in the editorial evaluation or decision to publish this article. All remaining authors have declared no conflicts of interest.

Funding Statement

No funding to declare.

References

1. Bioulac-Sage P, Sempoux C, Balabaud C. Hepatocellular adenoma: classification, variants and clinical relevance. *Semin Diagn Pathol* 2017; 34: 112-25.
2. Nault JC, Paradis V, Cherqui D, Vilgrain V, Zucman-Rossi J. Molecular classification of hepatocellular adenoma in clinical practice. *J Hepatol* 2017; 67: 1074-83.
3. Rebouissou S, Imbeaud S, Balabaud C, et al. HNF1alpha inactivation promotes lipogenesis in human hepatocellular adenoma independently of SREBP-1 and carbohydrate-response element-binding protein (ChREBP) activation. *J Biol Chem* 2007; 282: 14437-46.
4. Ibarrola C, Castellano VM, Colina F. Focal hyperplastic hepatocellular nodules in hepatic venous outflow obstruction: a clinicopathological study of four patients and 24 nodules. *Histopathology* 2004; 44: 172-9.
5. Kondo F. Benign nodular hepatocellular lesions caused by abnormal hepatic circulation: etiological analysis and introduction of a new concept. *J Gastroenterol Hepatol* 2001; 16: 1319-28.
6. Sempoux C, Balabaud C, Paradis V, Bioulac-Sage P. Hepatocellular nodules in vascular liver diseases. *Virchows Arch* 2018; 473: 33-44.
7. Sempoux C, Paradis V, Komuta M, et al. Hepatocellular nodules expressing markers of hepatocellular adenomas in Budd-Chiari syn-

- drome and other rare hepatic vascular disorders. *J Hepatol* 2015; 63: 1173-80.
8. Sanada Y, Mizuta K, Niki T, et al. Hepatocellular nodules resulting from congenital extrahepatic portosystemic shunts can differentiate into potentially malignant hepatocellular adenomas. *J Hepatobiliary Pancreat Sci* 2015; 22: 746-56.
 9. Bertheau P, Degott C, Belghiti J, et al. Adenomatous hyperplasia of the liver in a patient with congenital hepatic fibrosis. *J Hepatol* 1994; 20: 213-7.
 10. Fukushima N, Kuromatsu R, Uchiyama D, et al. Hyperplastic nodular hepatic lesions following end-to-side portacaval shunting in childhood. *Intern Med* 2007; 46: 1203-8.

What's New in Pathology Newsletter by PathologyOutlines.com

Nat Pernick

PathologyOutlines.com, Inc., Bingham Farms, MI, USA

PathologyOutlines.com is pleased to collaborate with JPTM to publish its What's New in Pathology newsletter, written by our Editorial Board to provide updated subspecialty information.

Dr. Pernick started the website in August 2001 by writing the Thyroid chapter in Microsoft Word while at a family camp, using his residency and fellowship notes, textbooks and other references. The underlying idea was that pathologists anywhere should be able to find the information they need, fast and free, and not rely on print references which may be outdated, in another location or available only for a fee.

Today, in our 20th year, our textbook of 5000 topics is maintained by 17 employees, our Editorial Board (Fig. 1) and 300+ active authors. The Editor-in-Chief (Dr. Debra Zynger) and Deputy Editors determine the textbook content, which focuses on entities likely to be encountered by practicing anatomic and clinical pathologists. Authors are staff pathologists who have published at least five non-case report journal articles about their subspecialty in the past 15 years and meet our other qualifications. Authors are assigned topics based on their publication history, using templates and guidelines similar to those in journals. All topics go through a peer review process.

In contrast to books and journals, topics on PathologyOutlines.com use bullets and are updated regularly. Sections include essential features of the topic, abundant high quality photomicrographs complete with captions and legends contributed by authors, a sample pathology report, detailed differential diagnoses and board review style questions. A recently written topic is Ovarian serous borderline tumor by Drs. Sharma and Lastra [1].

We also provide:

- Case of the Month with diagnostic microscopic images and a short but useful discussion; cases are also compiled by subspecialty.
- Books for pathologists with recommendations and various search criteria
- Jobs and Conference listings for pathologists with dynamic graphs. We recently published a summary of job trends in the US job market [2].
- A compilation of over 1600 Board review style questions, sorted by subspecialty.
- Libraries of educational information from advertisers, available 24/7/365, as well as Banners and E-blasts for information useful to pathologists.

Dr. Pernick, the founder and owner, is an AP/CP pathologist who has worked with computers since 1970, practiced law for 20 years and has owned many businesses. His philosophy is an important part of the business:

- The website should be fast, free and easy to use.
- The needs of pathologists are our top priority.
- We aim for exceptional treatment of employees, visitors and advertisers.
- We make charitable contributions a major part of our business. Currently, we sponsor a pandemic music relief program (<https://www.pathologyoutlines.com/musicaward.html>).
- We are always open to ideas on how to make the website more useful to pathologists. We also welcome ideas on how to use the worldwide network of pathologists connected through PathologyOutlines.com to help our profession and humanity.

Received: March 7, 2021 Accepted: March 8, 2021

Corresponding Author: Nat Pernick, MD

PathologyOutlines.com, Inc., 30100 Telegraph Road, Suite 408, Bingham Farms, MI 48025, USA

Tel: +1-248-646-0325, E-mail: Nat@PathologyOutlines.com

<https://orcid.org/0000-0002-7020-7803>

References

- Sharma A, Lastra RR. Serous borderline tumor. PathologyOutlines.com website. <https://www.pathologyoutlines.com/topic/ovarytumorserosborderline.html>. Accessed March 8th, 2021.
- Zynger DL, Pernick N. Understanding the Pathology Job Market: An Analysis of 2330 Pathology Job Advertisements From 2013 Through 2017. Arch Pathol Lab Med 2019;143:9-10.



PathologyOutlines.com Editorial Board

find pathology information fast

March 2021



Fig. 1. Editorial Board of PathologyOutlines.com (March 2021).

What's new in gynecologic pathology 2021: vulva, cervix, and uterus

Carlos Parra-Herran¹ and Jennifer A. Bennett²

¹Department of Pathology, Brigham and Women's Hospital and Harvard Medical School, Boston, MA, USA

²Department of Pathology, University of Chicago Medical Center, Chicago, IL, USA

Received: March 8, 2021 Accepted: March 9, 2021

Corresponding Author: Carlos Parra-Herran, MD
 Department of Pathology, Brigham and Women's Hospital and Harvard Medical School, Boston, Massachusetts, USA

E-mail: CPARRA-HERRAN@bwh.harvard.edu

ORCID

Carlos Parra-Herran

<https://orcid.org/0000-0003-1420-7291>

Jennifer Bennett

<https://orcid.org/0000-0001-8155-7131>

This article has been published jointly, with consent, in both Journal of Pathology and Translational Medicine and PathologyOutlines.com



PathologyOutlines.com

The 5th edition of the World Health Organization of Tumours of Female Reproductive Organs was published in 2020. This is a compilation of the most important changes in the vulva, cervix and uterus.

VULVA

- Squamous intraepithelial lesions and squamous cell carcinomas are now classified as **HPV-associated and HPV-independent**.
- p16 overexpression is a reliable surrogate marker of HPV infection. A second marker with prognostic utility is p53. Thus, squamous neoplasms are now classified in three main groups: p16 overexpressed / p53 normal, p16 negative / p53 abnormal and p16 negative / p53 normal.
- HPV-independent (p16 negative), p53 abnormal

mal carcinomas have been associated with worse progression-free and overall survival compared to HPV-associated carcinomas as well as p16 negative / p53 normal carcinomas.

- **HPV-associated squamous intraepithelial lesions** (formerly known as vulvar intraepithelial neoplasia of the usual / classic type) represent the majority (90%) of precursors. They are referred to as low-grade (LSIL, equivalent to uVIN1) and high-grade (HSIL, equivalent to uVIN2 and uVIN3).
 - HSIL is characterized by p16 overexpression and wild-type p53 (with strong staining in mid-epithelial layers and negative or patchy basal / parabasal staining).
- The most common HPV-independent lesion is differentiated **vulvar intraepithelial neoplasia (dVIN)**. Its presumed rapid progression to invasive carcinoma and the difficulties in its diagnosis likely explain why dVIN represents only <10% of squamous intraepithelial lesions.
 - dVIN is characterized by negative or patchy p16 and mutant-type p53 expression (the latter could be full-thickness strong, basal strong, completely negative or cytoplasmic staining).
- Another, far less common form of HPV-independent lesion is the now called **differentiated exophytic vulvar intraepithelial lesion (DE-VIL)**. This lesion demonstrates verruciform acanthosis, hypogranulosis and cytoplasmic pallor (Figure 1). Unlike HSIL and dVIN, DE-VIL lacks cytologic atypia.

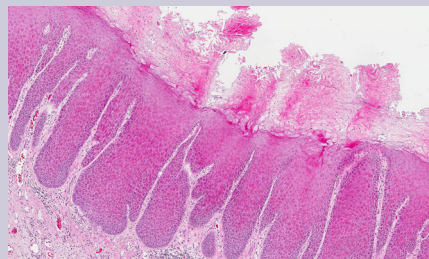


Fig. 1. Differentiated exophytic vulvar intraepithelial lesion (DE-VIL).

- DE-VIL has been associated with p16 negative / p53 normal carcinomas, including verrucous and conventional squamous cell carcinoma.
- DE-VIL is characterized by negative or patchy p16 and wild-type p53 (heterogeneous staining).

CERVIX

- Carcinomas in both squamous and glandular categories are now classified as **HPV-associated and HPV-independent**.
- More than 90% of squamous cell carcinomas of the cervix are secondary to HPV infection. There is emerging evidence showing that the HPV-independent subgroup (~7%) has worse outcome.
- There are currently no morphologic clues to distinguish between HPV-associated and HPV-independent squamous cell carcinomas.
- Adenocarcinoma in-situ also now has two recognized categories: HPV-associated (frequently referred to as "usual") and HPV-independent. Currently, only gastric-type AIS and atypical lobular endocervical glandular hyperplasia belong to the latter category. They feature foamy clear to eosinophilic mucinous cytoplasm, distinct cell borders, nuclear atypia and intraglandular growth (tufting, micropapillary, cribriform) (Figure 2).

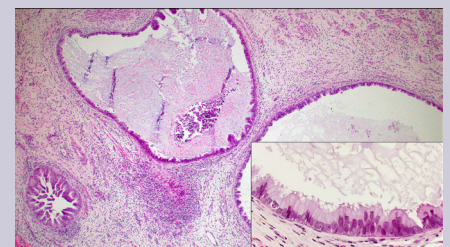


Fig. 2. Adenocarcinoma in situ, gastric type.

- HPV-independent adenocarcinomas, in particular gastric-type adenocarcinoma, have worse clinical behavior than HPV-associated adeno-

Sponsored by an unrestricted grant from ELITechGroup

carcinomas.

- **HPV-associated endocervical adenocarcinomas** represent 85-90% of all adenocarcinomas. Their histologic hallmark is the presence of conspicuous apical mitoses and apoptosis.
 - They are characterized by p16 overexpression (strong and diffuse, nuclear and cytoplasmic staining), normal p53 staining and negative to weak ER/PR staining.
 - The usual subtype is the most common, defined as having < 50% of cells with intracytoplasmic mucin, with the remaining having non-mucinous cytoplasm.
 - The mucinous subtype, defined as having > 50% cells with intracytoplasmic mucin, can feature endocervical-type mucinous epithelium or intestinal-type epithelium.
 - Invasive stratified mucin-producing carcinoma is a novel subtype, characterized by solid nests of multilayered mucinous epithelium resembling stratified mucin-producing intraepithelial lesion (SMILE). This subtype appears to have a worse outcome compared to other HPV-associated subtypes.
- **Gastric-type adenocarcinoma** represents the most common type of HPV-independent adenocarcinoma (~10% of all adenocarcinomas). It includes the formerly called minimal-deviation adenocarcinoma / adenoma malignum.
 - It features epithelium with foamy clear to eosinophilic mucinous cytoplasm and prominent cell borders.
 - It is negative for hormone receptors, but often expresses HIK1083 (a marker of pyloric-type epithelium). p53 can show mutant-type expression, and p16 can be strong and diffuse.
- Other recognized types of HPV-independent adenocarcinoma are clear cell and mesonephric. Endometrioid and serous carcinomas of the cervix are exceedingly rare, and their diagnosis requires first exclusion of an endometrial and tubo-ovarian primary.

UTERUS-EPITHELIAL

- An algorithm for applying The Cancer Genome Atlas (TCGA) classification system (POLE-mutated, microsatellite instable, copy number low and copy number high/TP53-mutated) is provided. Surrogate markers for molecularly classifying endometrial carcinomas include targeted POLE sequencing, and MSH6, PMS2 and p53 immunohistochemistry.
- **Molecular features in serous carcinomas have been updated to include ERBB2 (HER2) amplification in 30% of tumors;** such patients have been shown to benefit from trastuzumab therapy.
- **The category of mucinous carcinoma, defined by mucinous cells involving > 50% of the tumor, has been eliminated.**
- **Novel subtypes of endometrial carcinoma including mesonephric-like carcinoma and gastric (gastrointestinal)-type mucinous carcinoma have been added.**

- Mesonephric-like carcinoma is characterized by a variety of architectural patterns, focal intraluminal eosinophilic secretions and nuclei resembling papillary thyroid carcinoma with mild to moderate atypia (Figure 3). They are often GATA-3, TTF-1, calretinin, and CD10 (luminal) positive, with ER negative or at most focally positive. Many harbor KRAS mutations and gain of chromosome 1q.

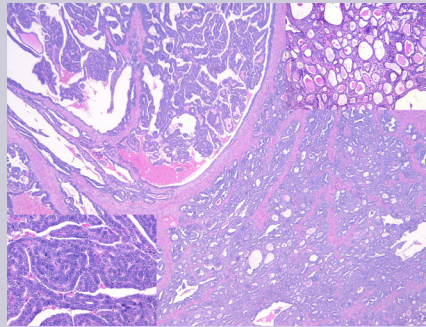


Fig. 3. Mesonephric-like endometrial carcinoma.

- Gastrointestinal-type mucinous carcinoma is composed of mucin-secreting glands (+/- goblet cells) with low-grade atypia and may be mismatch repair protein-deficient.
- **Carcinosarcoma is now considered a subtype of endometrial carcinoma rather than a mixed epithelial and mesenchymal tumor.**

UTERUS-MESENCHYMAL

- **Fumarate hydratase-deficient leiomyoma has been added as a subtype of leiomyoma** and is characterized by staghorn vessels, alveolar-pattern edema, scattered bizarre nuclei, ovoid nuclei sometimes arranged in chains, eosinophilic cytoplasmic (rhabdoid) inclusions and prominent eosinophilic nucleoli surrounded by perinucleolar halos (Figure 4). It may harbor somatic or germline fumarate hydratase mutations, the latter being diagnostic of hereditary leiomyomatosis and renal cell carcinoma (HLRCC) syndrome.

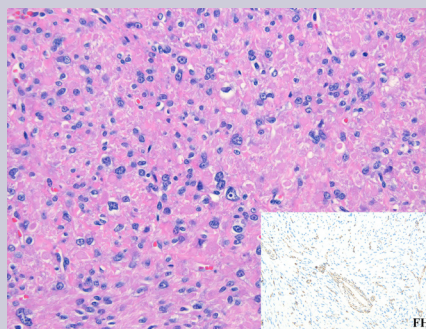


Fig. 4. Fumarate hydratase deficient leiomyoma.

- Specific diagnostic criteria for myxoid leiomyosarcoma are proposed: presence of any cytological atypia, tumor cell necrosis or > 1 mitoses/10 HPF.

- IFITM1 has been included as a novel immunohistochemical stain that is often strongly and diffusely positive in endometrial stromal nodules and low-grade endometrial stromal sarcomas.
- **Novel subtypes of high-grade endometrial stromal sarcoma include those with BCOR alterations (ZC3H7B-BCOR fusions or BCOR internal tandem duplication), which have a morphology overlapping with other myxoid mesenchymal neoplasms.**
 - ZC3H7B-BCOR sarcomas are positive for cyclin D1, CD10 and BCOR (~50%), with variable ER/PR.
 - BCOR internal tandem duplication sarcomas are positive for cyclin D1 and BCOR, variably express CD10 and desmin, and are negative for ER, PR, SMA and caldesmon.
- Molecular alterations for uterine tumor resembling ovarian sex cord tumor (UTROSCT) include NCOA1-3, ESR1 or GREB1 fusions.
- Modified gynecologic-specific criteria for predicting PEComa behavior with elimination of the "benign" category are proposed.
- Inflammatory myofibroblastic tumor has been added as a distinct entity and a subset with malignant behavior is recognized. The most common ALK fusion partners include IGFBP5, THBS1 and TIMP3.
- **NTRK-rearranged spindle cell neoplasm is a novel low-grade sarcoma most common in the cervix.** It is positive for S100, CD34 and TRK, negative for ER, PR, CD10, SMA and desmin, and harbors NTRK fusions.

This newsletter is a featured collaboration with PathologyOutlines.com

Conflicts of Interest

The authors declare that they have no potential conflicts of interest.

Meet the Authors

Dr. Parra-Herran has been part of the Pathology Outlines editorial board since 2016. He is originally from Colombia and started his academic pathology career in Canada. He is currently affiliated with Brigham and Women's Hospital and Harvard Medical School as a pathologist and associate professor of pathology.

Dr. Bennett has been part of the Pathology Outlines editorial board since 2019 and was appointed deputy editor-in-chief of gynecologic pathology in 2020. She is currently an assistant professor at the University of Chicago Medical Center. Her research primarily focuses on the integration of morphology and molecular features, particularly in uterine mesenchymal neoplasms.

